CO2MVS RESEARCH ON SUPPLEMENTARY OBSERVATIONS

Estimates of the annual fossil fuel CO_2 emissions at the continental to national scales over a decade and recommendations for the implementation of global scale Oxygen and $^{14}CO_2$ data assimilation in the CO2MVS

Due date of deliverable	December 31, 2025
Submission date	December 5, 2025
File Name	CORSO-D3-5-V1.1
Work Package /Task	WP3 /3.3-3.4
Organisation Responsible of Deliverable	UNIVBRIS/WU
Author name(s)	H. Allen, J. Hooghiem, C. Gómez-Ortiz, E. Saboya, M. Rigby, I. Luijkx, G. Broquet, M. Scholze, A. Visser
Revision number	1.1
Status	Final
Dissemination Level / location	Public www.corso-project.eu

The CORSO project (grant agreement No 101082194) is funded by the European Union.

1 Executive summary

This report summarises progress made under Tasks 3.3 and 3.4 of the CORSO project, in which global and regional estimates of fossil fuel carbon dioxide ($ffCO_2$) flux were derived using atmospheric observations of ^{14}C in CO_2 and oxygen and atmospheric chemical transport models. It fulfils Deliverables D3.5 and D3.6, which are jointly described here to provide a consolidated overview of the current state of the science in this area.

Since atmospheric CO_2 mole fractions are influenced by fluxes from the terrestrial biosphere and the ocean in addition to fossil fuel emissions, it is well-established that the evaluation of fossil fuel emissions inventories at regional to global scales are likely to require atmospheric tracer measurements to supplement the inverse analyses of atmospheric mole fraction data. Previous studies have indicated that measurements of atmospheric radiocarbon (^{14}C) in CO_2 ($\Delta^{14}CO_2$) and concurrent atmospheric oxygen (O_2) and CO_2 observations may provide additional constraints on fossil fuel emissions, compared to atmospheric CO_2 mole fraction measurements alone. As radiocarbon has a half-life on the order of thousands of years, fossil fuels are ^{14}C-free, and therefore, fossil fuel emissions lead to a reduction in the $^{14}CO_2/^{12}CO_2$ ratio ($\sim\Delta^{14}CO_2$) in the atmosphere. CO_2 and O_2 are coupled in all processes in the carbon cycle, except for ocean exchange, and by assuming a fixed exchange ratio between the atmosphere and terrestrial biosphere, CO_2 and O_2 can be combined in "atmospheric potential oxygen (APO)", which on large scales is dominated by fossil and oceanic fluxes.

Tasks 3.3 and 3.4 of CORSO addressed key challenges relating to the inference of fossil fuel CO_2 emissions at global (Task 3.3) and European (Task 3.4) scales. Inverse modelling systems were adapted to assimilate atmospheric $\Delta^{14}CO_2$ and/or O_2. At the global scale, atmospheric $\Delta^{14}CO_2$ observations were incorporated into the Community Inversion Framework (CIF) with the LMDZ atmospheric transport model (LSCE), and atmospheric $\Delta^{14}CO_2$ and O_2 measurements were incorporated into the Carbon Tracker Europe system (CTE, WU). At the European scale, the high-resolution (~10 km resolution) transport models, NAME (UK Met Office Numerical Atmospheric dispersion Modelling Environment) and LUMIA were used to simulate fossil fuel tracers. Regional inversions were performed respectively by UNIVBRIS using the Regional Hierarchical Inverse Modelling Environment (NAME-RHIME) using $\Delta^{14}CO_2$ and APO, and LUND for $\Delta^{14}CO_2$ using LUMIA. Atmospheric observations were incorporated into these systems and the influence of potential confounding factors for the determination of $ffCO_2$ were investigated.

The primary achievement outlined in this report is the implementation of inverse analyses of atmospheric $\Delta^{14}CO_2$ observations in all four models, and preliminary inverse analyses of O_2 (or APO) in one global and one regional model. The lessons learned in establishing these systems have informed the below recommendations for CO2MVS.

For the inference of $ffCO_2$ using $\Delta^{14}CO_2$ at the European scale, all models used flask measurements from the Integrated Carbon Observing System (ICOS), including the "intensive" sampling period during 2024, when the frequency of flask analysis was increased by approximately a factor of 2 through CORSO Task 3.1 (D3.3). As the average footprint of the ICOS samples was highest over Germany, our analyses focused on Germany. The major findings of this part of the study were that:

1. The enhanced sampling during 2024 led to $ffCO_2$ emissions estimates for Europe and Germany that were less strongly influenced by prior estimates, compared to earlier years.
2. A consistent seasonality in German $ffCO_2$ emissions was derived from the ensemble of inversions, with emissions being substantially lower during the summer than in the winter. This seasonal cycle was found to be larger than in the prior emissions estimates used by some of the models (EDGAR and GridFED).

3. The magnitude of $ffCO_2$ emissions estimates for Germany based on atmospheric $\Delta^{14}CO_2$ observations was broadly consistent between models, but further work is needed to determine the influence on these estimates of the assumed background $\Delta^{14}CO_2$, the nuclear industry and uncertainties in the isotopic signature of respiration fluxes.

European emissions estimates of $ffCO_2$ using CO_2 and O_2 data were more preliminary than those derived from $\Delta^{14}CO_2$ and indicated that further work is needed to reconcile the model results. Model-measurement comparisons were performed using NAME-RHIME and CTE with ICOS flask samples measured for O_2. Forward simulations using NAME-RHIME suggested a substantial under-estimation in German $ffCO_2$, assuming negligible ocean influence on the data. However, a marked difference in model performance was found between in-land and coastal measurement sites, potentially indicating ocean APO exchange. In contrast, CTE did not find an overall large difference with inventory $ffCO_2$ and that derived from O_2 data. However, their analysis did suggest a much larger emissions seasonal cycle than the inventories' and the $ffCO_2$ derived from atmospheric $\Delta^{14}CO_2$. In the CTE system, the combination of both O_2 and $\Delta^{14}CO_2$ provided the most robust results. Neither model was yet able to establish the added value of continuous atmospheric O_2 measurements, beyond the forward model comparisons with NAME-RHIME published near the beginning of CORSO. Further work in that area will be undertaken in the partner project, PARIS, during 2026.

At the global scale, CIF-LMDZ and CTE inversions showed that global $ffCO_2$ is not well constrained by the existing background network for atmospheric $\Delta^{14}CO_2$, given the uncertainties in heterotrophic respiration flux and its isotopic signature. However, the importance of global simulations and inversions was noted for constraining the $\Delta^{14}CO_2$ regional background. For the global study using O_2 data (CTE), the assimilation of O_2 was found to produce a useful additional constraint on land/ocean flux partitioning, compared to inversions using atmospheric CO_2 mole fractions alone.

Based on these findings, the recommendations for the future of $\Delta^{14}CO_2$ and O_2 data in CO2MVS are provided at the end of this report. These recommendations are summarised as follows:

1. Based on the knowledge gained in developing simulations for $\Delta^{14}CO_2$ and O_2 in Tasks 3.3 and 3.4, the implementation and evaluation of these tracers in the IFS should be continued in the near term, so that forward simulations can be compared to the atmospheric observations.
2. Our findings suggest that atmospheric $\Delta^{14}CO_2$ observations provide a constraint on $ffCO_2$ for north-western Europe, at least for Germany, based on the ICOS $\Delta^{14}CO_2$ network and the enhanced sampling frequency during CORSO for 2024. This measurement frequency should be maintained, and sampling should be expanded to the rest of Europe so that $ffCO_2$ can be derived for other countries.
3. Maintenance and expansion of the global background $\Delta^{14}CO_2$ network should be encouraged to provide background fields for regional inversions and, given sufficient measurement density, to better constrain global $ffCO_2$.
4. Reduced uncertainties are needed for respiration flux and its ^{14}C isotopic signature.
5. Further work is needed to establish the use of atmospheric O_2 as a tracer for $ffCO_2$, particularly using continuous atmospheric measurements. The influence on $ffCO_2$ of ocean and biosphere CO_2 and O_2 exchange needs to be established.

Table of Contents

2 Introduction

2.1 Background

To ensure the European Union (EU) moves towards a low-carbon economy and implements its commitments under the Paris Agreement, a binding target was set to cut greenhouse gas emissions in the EU by at least 40% below 1990 levels by 2030. European Commission (EC) President von der Leyen committed to deepen this target to at least a 55% reduction by 2030. This was further consolidated with the release of the Commission's European Green Deal on the 11th of December 2019. The European Green Deal set targets for the European environment, economy, and society to reach net zero emissions of greenhouse gases in 2050, outlining all needed technological and societal transformations that are aiming at combining prosperity and sustainability. To support EU countries in achieving their greenhouse gas emission targets, the EU and European Commission recognised the need for an objective way to monitor anthropogenic CO_2 emissions and their evolution over time.

Such a monitoring capacity will deliver consistent and reliable information to support informed policy- and decision-making processes, both at national and European level. To maintain independence in this domain, it is seen as critical that the EU establishes an observation-based operational anthropogenic CO_2 emissions Monitoring and Verification Support (MVS) (CO2MVS) capacity as part of its Copernicus Earth Observation programme.

The CORSO research and innovation project has built on and complements the work of previous projects such as CHE (the CO_2 Human Emissions), and CoCO2 (Copernicus CO_2 service) projects, both led by the European Centre for Medium-Range Weather Forecasts (ECMWF). These projects had already started the ramping-up of the CO2MVS prototype systems, so it can be implemented within the Copernicus Atmosphere Monitoring Service (CAMS) with the aim to be operational by 2026. The CORSO project has further supported establishing the new CO2MVS addressing specific research & development questions.

The main objectives of CORSO were to deliver further research activities and outcomes with a focus on the use of supplementary atmospheric observations, i.e., of co-emitted species as well as the use of auxiliary observations to better separate fossil fuel emissions from the other sources of atmospheric CO_2. CORSO aimed to deliver improved estimates of emission factors/ratios and their uncertainties of co-emitted species, as well as to use observations of co-emitted species at global and regional scales to better estimate anthropogenic CO_2 emissions. CORSO also aimed to provide clear recommendations to CAMS, the Integrated Carbon Observation System (ICOS), and the World Meteorological Organization (WMO) about the potential added-value of high-frequency atmospheric $\Delta^{14}CO_2$ and oxygen (O_2, including Atmospheric Potential Oxygen; APO) observations as tracers for fossil fuel emissions in both global and regional scale inversions. Furthermore, CORSO aimed to develop coupled land-atmosphere data assimilation in the global CO2MVS system constraining carbon cycle variables with satellite observations of soil moisture, leaf area index (LAI), solar induced fluorescence (SIF), and biomass. Finally, CORSO aimed to provide specific recommendations for the topics above for the operational implementation of the CO2MVS within the Copernicus programme.

2.2 Scope of this deliverable

2.2.1 Objectives of this deliverable

This deliverable reports on work in Work Package 3, specifically Tasks 3.3 and 3.4. In these tasks, the goals were to develop global and European scale multi-tracer or purely "fossil fuel CO_2" inverse modelling systems. These systems were used to assess the relevance of assimilating atmospheric $\Delta^{14}CO_2$ and O_2 (or APO) observations with atmospheric CO_2 data to disentangle the fossil fuel component from other CO_2 signals and derive fossil fuel emission estimates for several decades at continental scale, and for recent years in Europe at regional scales.

Ultimately, the analyses with the inversions in WP3 aimed to provide guidance on the potential use of these tracers for attribution and verification in the CO2MVS framework and prepare for their future implementation (with a transfer of the modelling capacities developed here), either in the main multi-scale inversion system or for benchmarking. Inversion Tasks 3.3 and 3.4 strongly relied on inputs from the Tasks 3.1 and 3.2 in WP3 (see Deliverables D3.1, D3.2, D3.3 and D3.4), and in particular on the unprecedented set of high-frequency monitoring of atmospheric $\Delta^{14}CO_2$ in Europe in 2024 and expansion of the continuous atmospheric O_2 measurement sites to include Cabauw thanks to CORSO (O_2 flask sampling already started in 2022 by ICOS).

This deliverable report documents these global and regional inversion systems, the challenges of their development, and specific sets of analyses that address:

- The value of atmospheric $\Delta^{14}CO_2$ and O_2 (APO) for inferring fossil fuel CO_2 emissions on global and national scales, and the added value gained from WP3 intensive sampling period compared to the more traditional sampling of these tracers.
- The large-scale constraints on the fossil fuel emissions versus the natural atmosphere-land and atmosphere-ocean carbon flux exchanges, brought by atmospheric $\Delta^{14}CO_2$ and O_2 (APO) observations.
- The potential to evaluate national budgets for selected countries, especially in north-western Europe where there are well-established emissions inventory estimates.
- The impact of uncertainties of emissions from nuclear power generation ($^{14}CO_2$), in terrestrial respiration fluxes ($^{14}CO_2$), in the atmospheric observations, in exchange ratios (O_2 /APO), and in the ocean fluxes (O_2 /APO).
- The need for the extension of the current atmospheric observation networks and the intensification of atmospheric CO_2-tracer observations.

2.2.2 Work performed in this deliverable

A major part of the efforts in Tasks 3.3 and 3.4 was dedicated to the development and tests of the multi-tracer and fossil fuel inverse modelling configurations. Most of these configurations were based on pre-existing atmospheric transport inverse modelling frameworks but in some cases, the specific inversion system with the coupling between these frameworks and specific (e.g., higher resolution) configurations of the transport models were further developed during this project. Furthermore, the modelling groups invested time to:

- Implement and test the additional tracers.
- Expand the inversions to very recent years (including 2024).
- Set up new control vectors for some of the multi-tracer approaches.
- Implement and use new input products from WP3 and other projects.
- Implement the corresponding statistics of the uncertainties in the prior estimate of the fluxes and isotopic signatures, disequilibrium or O_2 outgassing fluxes.

Reference inversions have been conducted over more than two decades over the globe and for more than five years at the European scale. Finally, major efforts have been dedicated to conduct sensitivity tests and analysis to fulfil the main objectives of the tasks.

2.2.3 Deviations and counter measures

The development and set up of suitable inverse modelling frameworks and the launch of reference inversions, after having overcome major challenges in the initial tests, took more time than expected in the Tasks 3.3 and 3.4. This highlights the challenges of developing multi-tracer approaches with a full joint modelling and assimilation of the atmospheric CO_2, $\Delta^{14}CO_2$ and O_2 tracers. The amount of tests and analyses to answer the main questions posed in WP3 was less extensive than initially planned, and two specific targeted studies were not conducted. The first one corresponded to the site-level attribution, which also depended on observations that were not fully available (see e.g. D3.3 on measurement issues at Heathfield station, UK). The second corresponded to the simulations of the tracers for future decades based on the emissions scenarios developed in Task 3.2. Initial simulations with future emission scenarios have been conducted for $\Delta^{14}CO_2$, but they should be refined. Furthermore, the current inversion experiments described in this deliverable showed that even in the present situation we have to learn more about the types of signals which provide the main constraints for the derivation of fossil fuel emissions. For fully assessing future emission scenarios, we should further refine the present inversions, so we can see the impact the decline in emissions would have on the potential for future emissions evaluation. Finally, the implementation into IFS was started at ECMWF, but did not yet result in simulations for these tracers.

However, specific experiments were targeted with specific inversion systems to ensure that this deliverable brings insights for the main objectives assigned to Tasks 3.3 and 3.4, and the set of experiments detailed in this document provides some clear views on the current challenges and potential of the multi-tracer inversion approach.

This Deliverable represents the work performed for both Deliverable 3.5 and 3.6. Given the strong connections between the regional and global scale inversion systems, and to strengthen the recommendations and conclusions, we have combined the results from the global and regional systems into a single Deliverable instead of two separate ones.

2.3 Project partners:

Partners	
COMMISSARIAT A L'ENERGIE ATOMIQUE ET AUX ENERGIES ALTERNATIVES	CEA
WAGENINGEN UNIVERSITY	WU
UNIVERSITY OF LUND	ULUND
UNIVERSITY OF BRISTOL	UNIVBRIS
EUROPEAN CENTER FOR MEDIUM-RANGE WEATHER FORECASTS	ECMWF

3 Methods

This section explains the general concepts used in the tracer inversions of atmospheric $\Delta^{14}CO_2$ and O_2 (APO) and describes the methods applied to each of the inverse modelling systems.

3.1 Multi-tracer and fossil fuel inversions

Accurately separating natural and anthropogenic contributions to atmospheric CO_2 is essential for robust top-down emission estimates. In regions where land biospheric fluxes, ocean–atmosphere exchange, and fossil fuel emissions all influence observed mole fractions, using atmospheric CO_2 mole fraction observations alone may not be sufficient because different processes can produce similar atmospheric signals.

Multi-tracer inversions could address this problem by jointly assimilating atmospheric CO_2 and atmospheric tracers of CO_2 with a prominent signal from fossil fuel emissions e.g. radiocarbon (^{14}C) in CO_2 (reported as $\Delta^{14}CO_2$) or atmospheric oxygen O_2 (or Atmospheric Potential Oxygen; APO), allowing the optimisation of both natural fluxes (land biospheric and ocean exchange with the atmosphere) and fossil fuel emissions within a single framework. Intermediate approaches rely on the derivation of fossil fuel CO_2 signals from joint atmospheric observations of CO_2 and these tracers, and on their assimilation in "fossil fuel inversion frameworks" i.e. inversions that only simulate fossil fuel CO_2 data, and which only control fossil fuel emissions.

3.1.1 $\Delta^{14}CO_2$ modelling

Over small spatial and temporal scales, atmospheric radiocarbon in CO_2 provides an almost direct constraint on fossil fuel CO_2. Using both atmospheric $\Delta^{14}CO_2$ and CO_2 should improve the attribution of observed variability to specific natural and anthropogenic sources and sinks, and should lead to more consistent and empirically informed flux estimates. This combined approach should provide a strong basis for evaluating global and regional carbon budgets and for separating anthropogenic emissions from ecosystem processes. To formalise these components and their interactions, we introduce the mass-balance equations governing atmospheric CO_2 and $\Delta^{14}CO_2$. For extensive details, please refer to the given references.

Let the evolution of the atmospheric CO_2 burden, C, be expressed as

$$\frac{d}{dt}C = F_{bio} + F_{oce} + F_{ff}.$$

In this equation, F_{bio} is the net exchange with terrestrial ecosystems (including photosynthesis, respiration, and fires), F_{oce} is the air–sea CO_2 exchange, and F_{ff} represents fossil fuel and cement emissions.

The corresponding budget for atmospheric $\Delta^{14}CO_2$ is

$$\frac{d}{dt}(C\Delta_{atm}) = \Delta_{atm}(F_{bio} + F_{oce}) + (\Delta_{bio} - \Delta_{atm})F_{bio\to atm} + (\Delta_{oce} - \Delta_{atm})F_{oce\to atm} + \Delta_{ff}F_{ff} + F_{nuc} + F_{cosmo}.$$

Here, Δ denotes the radiocarbon signature of a carbon reservoir or flux, corrected for fractionation and radioactive decay following Stuiver & Polach (1977). Multiplying Δ by CO_2 (mole fractions or fluxes) yields conservative, additive quantities (Tans et al., 1993). The terms $\Delta_{atm}F_{bio}$ and $\Delta_{atm}F_{oce}$ represent exchanges of "modern" ^{14}C between the atmosphere and the

biosphere or the ocean's surface layer, which generally share similar radiocarbon levels (Graven et al., 2020).

The disequilibrium fluxes ($F_{bio\rightarrow atm}$ and $F_{oce\rightarrow atm}$) describe deviations in $\Delta^{14}CO_2$ between the atmosphere and the biosphere or ocean. Terrestrial disequilibrium arises from the release of ^{14}C-enriched carbon from older organic matter, while oceanic disequilibrium is mainly driven by ^{14}C-depleted carbon transported upward from deeper waters (Lehman et al., 2013; Basu et al., 2016). Fossil fuels, which contain no ^{14}C, are represented by $\Delta_{ff} = -1000‰$. Additional terms account for radiocarbon emitted by nuclear facilities (F_{nuc}) and natural ^{14}C production in the stratosphere (F_{cosmo}).

The structure of these equations varies slightly across the literature and leads to different implementations in the multi-tracer models; some formulations explicitly separate photosynthesis and respiration and assign isotopic signatures to each (Naegler & Levin, 2009; Turnbull et al., 2009; Potier et al., 2022). The version used above to illustrate the principle of the ^{14}C modelling follows Miller et al. (2012) and Basu et al. (2016). The multi-tracer systems used in this deliverable follow both types of formulation.

Another established method for separating fossil fuel CO_2 from natural fluxes is the regional isotope budget approach. This technique uses $\Delta^{14}CO_2$ to quantify the fossil fuel CO_2 enhancement at a monitoring site relative to a background location assumed to represent air masses unaffected by nearby emissions (Levin et al., 2003). The fossil fuel CO_2 component (C_{ff}) is derived from the difference between the observed (Δ_{obs}) and background $\Delta^{14}CO_2$ values (Δ_{bg}), combined through a simple mass-balance relationship that also accounts for biospheric exchange:

$$C_{ff} = C_{obs}\left(\frac{\Delta_{bg}-\Delta_{obs}}{\Delta_{bg}+1000‰}\right) + \beta.$$

Corrections for local influences, mainly radiocarbon emissions from nuclear facilities, are included in the β term, typically estimated through source-receptor atmospheric transport modeling (Maier et al., 2023).

The correction term, β, is defined as

$$\beta = \left(\frac{\Delta_{bg}-\Delta_{resp}}{\Delta_{bg}+1000‰}\right)C_{resp} + \left(\frac{\Delta_{bg}-\Delta_{gpp}}{\Delta_{bg}+1000‰}\right)C_{gpp} + \left(\frac{\Delta_{nuc}}{\Delta_{bg}+1000‰}\right).$$

Here, the first two terms represent the terrestrial biosphere correction - split between gross primary productivity (GPP) and respiration - and the last term is a correction for nuclear power plant $\Delta^{14}CO_2$. Since the global background $\Delta^{14}CO_2$ value (Δ_{bg}) is close to Δ_{gpp} (i.e. a small isotopic disequilibrium) at present, the terrestrial biosphere contribution is likely to be small in comparison to the nuclear power plant and fossil fuel contributions.

This approach is most effective in regions where fossil fuel emissions strongly deplete $\Delta^{14}CO_2$ and provides a practical way to estimate fossil fuel CO_2 enhancements without fully resolving all natural flux components. This method is used to pre-compute fossil fuel CO_2 mole fractions (C_{ff}), which are subsequently assimilated within a "fossil fuel" inverse modelling system, abbreviated as $ffCO_2$-only from now on, to support the optimisation of regional fossil fuel emissions. These pre-computed C_{ff} mole fractions are considered to be *pseudo-observations*, meaning that they are not measured directly in the atmosphere but are instead derived from atmospheric $\Delta^{14}CO_2$ observations under a set of assumptions about background conditions and correction terms. In this sense, they function as observational constraints within the inversion, but retain the uncertainties and potential biases associated with the underlying $\Delta^{14}CO_2$-based regional isotope budget (Maier et al., 2023).

Alternatively, this approach can be formulated to not apply the β correction to the observation term and instead optimise for each of the terms of β and for C_{ff} from the atmospheric observation term. In other words, the observations are kept on the left-hand side of the equation, and all the sectoral estimates on the right-hand side. This approach allows for the β correction to be adjusted, which should be relatively small, rather than kept fixed.

3.1.2 O_2 and APO modelling

Atmospheric CO_2 and $\delta(O_2/N_2)$ measurements can be combined into Atmospheric Potential Oxygen (APO; Stephens et al., 1998). This is defined in the below equation, where the value 1.1 denotes the CO_2:O_2 land biosphere molar exchange ratio; 350 is an arbitrary reference value; and X_{O2} is the standard O_2 reference value (equal to 0.20946; Machta and Hughes, 1970) used to convert the second term from ppm to per meg

$$\delta(APO) = \delta(O_2/N_2) + \frac{1.1}{X_{O2}}(CO_2 - 350)\,.$$

Assuming that the terrestrial land biosphere molar exchange ratio is close to 1.1, atmospheric variations in APO are dominated by fossil fuel fluxes and exchange with the ocean (e.g., Pickers et al., 2022; Chawner et al., 2024). Therefore, it has been proposed that APO variations can be used to infer fossil fuel CO_2 emissions, if ocean influences are small.

Recent work by Faassen et al. (in prep.) shows that in certain cases, the biosphere exchange ratio can vary from the fixed value of 1.1. This can influence fossil fuel estimates using APO, especially in regions where there are large biosphere signals (particularly in summer), or regions where the variability in the exchange ratio is large. In the inversions using CarbonTracker Europe (CTE, see Section 3.2.3), we therefore simulate the full O_2 signal, instead of APO.

3.2 Global systems

3.2.1 Community Inversion Framework - LMDZ (CIF-LMDZ)

The variational model of the Community Inversion Framework (CIF) coupled with the LMDz atmospheric general circulation model has been used to perform global inversions co-assimilating CO_2 and $\Delta^{14}CO_2$ data with transport modelling at different spatial resolutions and over different timescales to answer the questions on both the large and national scale constraints from radiocarbon on CO_2 inversions. The inversion configuration used here assimilates daily mean CO_2 and integrated and flask sample $\Delta^{14}CO_2$ observations, comparing them to mole fractions simulated using CIF-LMDZ that is fed by estimates of the CO_2 surface fluxes together with isotopic signatures for these fluxes following the formulation of joint CO_2/radiocarbon assimilation problem of Wang, (2016) and Potier et al (2022).

The CIF is a flexible, open-source framework developed in Python for enabling consistency across multiple systems of atmospheric inversions of greenhouse gases (Berchet et al, 2021). The CIF has been adapted to assimilate observations of atmospheric tracers together with their isotopes, independently optimize fluxes and isotopic signatures for multiple emissions categories, and optimize the initial atmospheric conditions (Thanwerdas et al, 2022). An offline version of LMDZ and its adjoint code has been interfaced with the CIF to provide seamless integration between the variational inversion algorithm and the atmospheric transport.

Atmospheric transport of CO_2 and $^{14}CO_2$ is simulated using the LMDz global circulation model. LMDz is the atmospheric component of the Earth system model of the Institut Pierre-Simon-Laplace (Durfresne et al, 2013), developed at the Laboratoire de Meteorologie Dynamique (LMD; Hourdin et al, 2006), that has been converted into an offline version for use in

atmospheric inversions (Chevallier et al, 2005). Precalculated meteorological inputs are fed to the model to reduce computation time, with the model simulating large-scale advection and sub-grid transport processes. LMDz uses the deep convective scheme of Tiedtke, 1989, and the vertical diffusion scheme of Louis, 1979. It is nudged every 6 hours towards a reanalysis of wind fields from the European Centre for Medium-Range Forecasts (ECMWF) ERA-5 products.

The results from two configurations of the CIF-LMDz multi-tracer system corresponding to different resolutions of LMDz are presented here. The first configuration simulates atmospheric distributions of these tracers over a period of 27 years from 1998 to 2024, inclusive, with LMDz at a standard resolution. The second configuration performs the simulation over a 4-year period, from 2021 to 2024 inclusive, with LMDz at a higher horizontal resolution. The first two years of the simulation considered a spin up period in both cases. The standard resolution configuration uses 144 grid points in both latitude and longitude, corresponding to a resolution of 1.3° latitude x 2.5° longitude; the high-resolution configuration uses 256 grid points (in both latitude and longitude), corresponding to 0.7° latitude x 1.4° longitude. Both LMDz configurations have a vertical discretization of 79 hybrid sigma-pressure layers extending from the surface to the top of the atmosphere (approximately 80 km altitude).

An initial coarse LMDz configuration was used for the first tests and analysis in task 3.3 (as documented in the report for milestone 7 of CORSO WP3). This configuration has a 96 grid point horizontal grid that corresponds to a horizontal resolution of 1.875° latitude x 3.75° longitude, with a vertical distribution of 39 hybrid sigma-pressure layers. The results from this configuration are not retained in this deliverable because the higher 1.3° x 2.5° resolution configuration proved to be attainable within the timeframe of the project. The higher resolution also provides more relevant results over the targeted past decades for the large-scale analysis. Transport is calculated at a 30-minute or 20-minute timestep for the 144 and 256 grid point configurations, respectively.

CO_2 and $^{14}CO_2$ are transported as two independent tracers in the model. All observations of $\Delta^{14}CO_2$ are converted to $\delta^{14}CO_2$ using background $\delta^{13}CO_2$; radiocarbon observations and isotopic signatures are converted between $\delta^{14}CO_2$ and $^{14}CO_2$ (mole fraction) using the modern standard $^{14}C/^{12}C$ ratio (R_{std} = 1.176 x 10^{-12}). For the standard resolution configuration, the initial CO_2 mole fractions are taken from outputs of the CAMS CO_2 global inversions based on the PyVAR-LMDz inversion system (Chevallier et al., 2023). The initial $\delta^{14}CO_2$ atmospheric distribution is taken from model outputs produced by Wang, 2016 and scaled to match the background average $\delta^{14}CO_2$ calculated from Graven et al, 2020.

Atmospheric observations of CO_2 and $\Delta^{14}CO_2$ are collected from the global greenhouse gas monitoring networks NOAA (United States), SIO (United States), ICOS (Europe), and NIWA (New Zealand). The CO_2 observations were taken from the NOAA Observation Package (ObsPack) data product (Schuldt et al., 2022 and 2023, and Bergamaschi et al., 2023). The data have been filtered to include observations from either the afternoon-only (12:00 to 17:00 local time) for stations at <1000 m altitude or night-only (0:00 to 5:00 local time) for stations situation above 1000 m altitude due to meteorological dynamics that can be difficult to simulate in the model. The $\Delta^{14}CO_2$ observations are provided by the CORSO project and further details on these measurements can be found in the deliverables D3.1 and D3.3.

The fluxes used to simulate CO_2 are categorized into fossil fuel, biomass burning, oceans, and the biosphere in the CIF-LMDz inversion framework; for the purpose of the multi-tracer approach (as implemented in the CIF-LMDz inversion framework following Wang, 2016 and Potier et al, 2022) the natural fluxes (oceans and biosphere) are further split into their gross one-way components of ocean-to-atmosphere (OA), atmosphere-to-ocean (AO), net primary productivity (NPP), and heterotrophic respiration (HR) fluxes due to the two components of the ocean and biosphere fluxes having different isotopic signatures. The prior estimates of

these fluxes are collected from a variety of flux products, with the prior fluxes chosen to align with the configuration of the CAMS CO_2 global inversions (Chevallier et al, 2023). Despite this attempt at alignment with the CAMS configuration, the practical implementation of the control vector used for the multi-tracer approach does produce significant differences with the CAMS configuration. For the higher resolution configuration, the initial CO_2 distribution is taken from the results of the standard resolution configuration. These flux products are regridded from their original resolution to the resolution on which LMDZ is run. Further information on the flux products is given below and summarized in Table 1.

The prior CO_2 ocean fluxes are generated using products from the Copernicus Marine Environmental Monitoring Service (CMEMS; Chau et al, 2024a, 2024b, and 2022) with the AO component calculated from the solubility of CO_2 in seawater, fraction of sea ice cover, and the CO_2 partial pressure in sea surface water and the atmosphere; the OA component is calculated from the difference between the net ocean flux and AO. The CO_2 biosphere fluxes are calculated using the ORganizing Carbon and Hydrology in Dynamic EcosystEms (ORCHIDEE) version 2.2 model (Krinner et al, 2005). The NPP is taken directly from the model output while HR is calculated as the difference between NEE and NPP. The ORCHIDEE products used here are a climatology (long-term average), using the mean of the years 1981 to 2020, to match the CAMS inversion configuration. The climatology was chosen to enable CAMS inversion to be run up to the present day without the delay due to the time needed to deliver the most up-to-date data products. The CO_2 fossil fuel emissions are taken from the Gridded Fossil Emissions Dataset (GridFED) produced by the Global Carbon Project (Janssens-Maenhout et al, 2019, Friedlingstein et al, 2023, Jones et al, 2021). The CO_2 biomass burning fluxes are from the Global Fire Emissions Database version 4 (GFED4; van der Werf et al, 2017).

Of the CO_2 fluxes, oceanic, biosphere, and fossil fuel fluxes are controlled by the inversion while biomass burning is not. The inversions control the fluxes at 1.3° x 2.5° and 10-day resolution even when simulating the transport at 0.7° latitude x 1.4° longitude resolution. The configuration of the prior error covariance matrix characterizing the statistics of the uncertainty in the prior estimates of the CO2 fluxes is described in Table 1. As explained above, these values have been selected to get approximately the same budget of uncertainty in NEE and net ocean fluxes at 1.3° x 2.5°/10-day scale with the same scales of spatial and temporal correlation as in the CAMS CO_2 global inversions. This set-up reflects the larger uncertainties in the terrestrial ecosystem fluxes compared to the other fluxes, which arises from the use of the long-term average for the prior estimate of the terrestrial fluxes and also the relatively good knowledge on the fossil fuel emissions whose order of magnitude should be fairly well known in the countries emitting the most fossil fuel CO_2.

Simulated atmospheric radiocarbon varies across the globe and in time because of the isotopic disequilibrium of the ocean and biosphere isotope signatures applied to the CO_2 fluxes, the cosmogenic and nuclear production of $^{14}CO_2$, and the dilution of $^{14}CO_2$ relative to $^{12}CO_2$ due to the lack of radiocarbon in fossil fuel emissions of CO_2. As explained above, the differences in the isotopic signatures for each of the one-way gross fluxes of the isotopic ocean and biosphere disequilibrium led to a separate control of the ocean-to-atmosphere (OA), atmosphere-to-ocean (AO), NPP, and HR components. Details of the prior estimate used for each of these isotopic signatures and for the $^{14}CO_2$ fluxes of other origins are given below. Several of these estimates are derived from the D3.4 radiocarbon flux database compiled in the frame of task 3.2. Similar to what is done for CO_2, the radiocarbon signatures and fluxes are regridded from their original resolution to the resolution of LMDZ. Further information on the flux products is given below and summarized in Table 1.

The ocean-to-atmosphere isotopic signature, the HR and NPP components of the biosphere disequilibrium, as well as the nuclear ^{14}C flux are taken from the D3.4 radiocarbon flux database compiled in the frame of task 3.2 and briefly summarized here. The isotopic

signatures for the ocean are derived from ^{14}C data from surface sea water measurements gathered by the Global Ocean Data Analysis Project (GLODAP) for the year 1995 and extended using ocean transect measurements collected by the Climate and Ocean: Variability, Predictability, and Change (CLIVAR) using the method described by Lindsay (2016). The NPP and HR components of the biosphere are taken from products generated by the global vegetation model Lund-Potsdam-Jena (LPJ; Sitch et al, 2003, Scholze et al, 2003). The global $^{14}CO_2$ nuclear flux is estimated using the annual electricity generation by nuclear power plants given by the International Atomic Energy Agency's Power Reactor Information System (IAEA PRIS) while the data for nuclear reprocessing sites are gathered from the ICOS Carbon Portal (Storm et al, 2004) and a report by the Japan Atomic Energy Agency (Nakada et al., 2008). These data are converted to a flux using the method and emissions factors from Graven and Gruber, 2011 and Zazzeri et al., 2018.

The atmosphere-to-ocean isotopic signature, fossil fuel isotopic signature, and cosmogenic production of $^{14}CO_2$ were derived independently. In brief, the atmosphere-to-ocean isotopic flux is taken from the lowest atmospheric layer of the initial $\Delta^{14}CO_2$ concentrations (see above) with a fractionation coefficient of -4 per mil applied. Fossil fuel emissions are assumed to have an isotopic signature of -1000% everywhere. The cosmogenic ^{14}C production is assumed to be a constant global production of 2.2 x 10^{26} ^{14}C atoms $year^{-1}$ with a latitudinal distribution that varies from a maximum at the poles to a minimum at the equator (Kanu et al, 2016 and Masarik and Beer, 2009).

Within the inversion framework, only the biogenic and oceanic isotopic signatures are controlled, both at 1.3° x 2.5° and 10-day resolution (same as for the CO_2 fluxes). The prior uncertainty in both the NPP and AO isotopic signatures is lower than those of the HR and OA isotopic signatures, as described in Table 1. In all cases, these prior uncertainties are assigned horizontal correlations of 500 km and temporal correlations of 5-year scales. The fossil fuel emission signature as well as the nuclear and cosmogenic emissions are not controlled by the inversion.

Table 1: Summary of fluxes and isotopic signatures as well as the corresponding prior uncertainties used in the inversion, with a control resolution of 1.3° latitude x 2.5° longitude and 10 days

	CO_2		**$\Delta^{14}CO_2$**	
	Flux source	*Prior uncertainties and correlations*	*Isotopic signature source*	*Prior uncertainties and correlations*
AO	CMEMS calculation	14% at control res. 1000 km spatial corr 1 month temporal corr	Surface $\Delta^{14}CO_2$	20% at control res. 500 km spatial corr 5-year temporal corr
OA	CMEMS calculation	14% at control res. 1000 km spatial corr 1 month temporal corr	GLODAP + CLIVAR calculation	50% at control res. 500 km spatial corr 5-year temporal corr
HR	ORCHIDEE climatology	92% at control res. 500 km spatial corr 1 month temporal corr	LPJ	50% at control res. 500 km spatial corr 5-year temporal corr
NPP	ORCHIDEE climatology	92% at control res. 500 km spatial corr 1 month temporal corr	LPJ	20% at control res. 500 km spatial corr 5-year temporal corr

Fire	GFED	Not controlled	-	-
FF	GridFED	50% at control res. No temporal or spatial correlation	Constant (-1000‰)	Not controlled
Nuc	-	-	PRIS+RADD CORSO product	Not controlled
Cosm	-	-	Constant (latitude gradient)	Not controlled

3.2.2 CarbonTracker Europe (CTE) - WU

The CarbonTracker Europe (CTE) multi-tracer setup is developed as a new version of CTE, called the CTE Long Window-Short Window (CTE-LW-SW) system (Hooghiem et al, in prep., van der Laan-Luijkx et al. 2017, Peters et al. 2007). Within CORSO, the CTE-LW-SW system was further developed for multi-tracer capacity for $\Delta^{14}CO_2$, $\delta O_2/N_2$ and $\delta^{13}CO_2$. The system uses the TM5 global transport model and is built within CarbonTracker Europe's Data Assimilation Shell (CTDAS).

The Transport Model 5 or TM5, simulating atmospheric trace gas chemistry and transport, is documented by Krol et al. (2005). TM5 is an offline tracer transport model used where the advection is computed using the slopes advection scheme (Russel and Lerner, 1981). This scheme is currently driven by ERA-5 reanalysis wind fields (Hersbach et al., 2020). The convection is computed from the convective entrainment and detrainment rates from the ERA-5 reanalysis. Free tropospheric diffusion is computed using the formulation by Louis (1979) and in the boundary layer using Holtslag and Boville (1993), where the diurnal variability in the boundary layer height is computed using Vogelezang and Holtslag (1996).

The CarbonTracker Europe Data Assimilation Shell (CTDAS) is the European branch of CarbonTracker (van der Laan-Luijkx et al., 2017, Peters et al. 2007). It is a data assimilation system dedicated to estimate (carbon) surface fluxes, via data assimilation of observations of atmospheric composition. The core analysis is done using the Ensemble Kalman Filter technique, where an ensemble represents the covariance in the fluxes, to obtain an optimal regression that minimizes the Bayesian Cost function. The ensemble can only represent limited degrees of freedom, which can lead to so-called spurious correlations, and the uncertainty reduction is overestimated.

In this work, we used CTE-LW-SW to perform global simulations over the period 2000-2025. The LW part of this system is specifically designed to deal with atmospheric records of greenhouse gas and related tracer observations that have sparse spatial and temporal coverage, such as those of $\delta^{13}CO_2$, $\Delta^{14}CO_2$ and $\delta O_2/N_2$. In the data assimilation system, the natural fluxes are fully coupled to CO_2 through isotopic ($\delta^{13}CO_2$, $\Delta^{14}CO_2$) or exchange ratios ($\delta O_2/N_2$). In addition, to solve for the natural (biosphere and ocean) fluxes, we optimize the disequilibrium fluxes as well as the oxygen outgassing over the ocean. Table 2 below shows the setup of the LW system, including correlations and uncertainties.

Table 2: settings of the CTE-LW system. For the last two columns: the dash means that these fluxes are not optimised

State	Prior flux	O_2 ratio	^{14}C-signature	Spatial	Temporal
Biosphere	SiB4	SiB4	LPJ	For each Olsen region in a Transcom region	Daily; 15 days; 4 year
Ocean	Carboscope	-	Constant -4 per mil	30 ocean basins; 3000 km	Daily; 60 days; 5 years
Fossil fuel flux	GridFED	GridFED	-1000 per mil	-	-
Fire flux	GFAS	SiB4	LPJ	-	-
^{14}C terrestrial biosphere disequilibrium	SiB4	-	LPJ	Transcom regions	Daily; 90 day correlation; 5 years
^{14}C ocean disequilibrium	LMDZ-CORSO	-		Transcom regions; correlation of 3000 km	Daily; 90 day correlation; 5 years
Nuclear	CORSO			-	-
Cosmogenic	Basu et al. 2020			-	-
Ocean oxygen flux	Scaled CESM			Transcom regions; correlation of 3000 km	Daily; 90 day correlation; 5 years

In the second short window (SW) step (see Table 3), an attempt was made to estimate fossil fuels over Europe and investigate the impact of various aspects on inversions. In this step, the focus is over Europe in 2024, the year of the intensive CORSO sampling. Also, fewer background observations were available over 2024, which gives less constraint over the rest of the globe. We perform several experiments for 2024 over Europe to show the constraints brought from the new observations in Europe. In these experiments, in contrast to the global setup, we now keep the disequilibrium fluxes as well as the oxygen outgassing over the ocean fixed. We use a gridded state vector over Europe, instead of larger (Transcom) regions in the global inversion. And we now also solve for fossil fuel emissions. For this, we reduce the prior fossil fuel emissions, from the known GridFED emissions in 2024 (which we regard as the "truth"), to the GridFED emissions from the year 2020, reduced by 20%, to see how well the network can inform on the fossil fuel emissions. Subsequently, we do different experiments using only one simulation of transport but selecting different observations. This allows us to

redo the data assimilation step only, and see the impact of each tracer separately. The experiments performed are as follows:

- Only using CO_2 observations. This includes observations from the Globalview Plus ObsPack, including many of the insitu stations from ICOS. To reduce the weight of the amount of CO_2 data in the assimilation we have randomly selected only 10 percent of the available data.
- Only the $\mathbf{\Delta}^{14}CO_2$ observations.
- Only the $\delta O_2/N_2$ observations.
- All tracers combined.

Two important notes: during the test phase, we found that a potentially large impact exists for samples with a very low O_2 value. These can be seen e.g. in the observations of Cabauw, and the low O_2 values likely indicate a very local fossil fuel signal (or measurement error). These very low O_2 values could not be simulated with our TM5 model at the relatively coarse resolution. Therefore, in the $\delta O_2/N_2$ only experiment, we introduced a filter for values deviating from the mean of the observations. For the other experiments we did not apply the filter. Secondly, the power of our multi-tracer data-assimilation lies in the coupling of all tracers, and in that sense these experiments that we performed so far do not provide the full picture. Instead, with our experiments presented here, we aim to quantify where the constraints can be found, and in these experiments, the tracers that were not assimilated serve as a validation. These individual tracer experiments thereby show how the combination of all tracers is influenced by either tracer, or potentially dominated by only one of them.

Table 3: settings of the CTE-SW system

State	**Prior flux**	**O_2 ratio**	**^{14}C-signature**	**Spatial**	**Temporal**
Biosphere	SiB4	SiB4	LPJ	Gridded over Europe; 300 km; For each olsen region in a transcom region	Daily; 15 days;
Ocean	Carboscope	-	Constant -4 per mil	30 ocean basins; 3000 km	Daily; 60 days; 4 years
Fossil fuel flux	GridFED	GridFED	-1000	Gridded over Europe; 600 km; For each olsen region in a transcom region-	-daily; 60 days
Fire flux	GFAS	SiB4	LPJ	-	-
^{14}C terrestrial biosphere disequilibrium	Optimized LW	-			

^{14}C ocean disequilibrium	Optimized LW				
Nuclear	CORSO				
Cosmogenic	Basu et al. 2020				
Ocean oxygen flux	Optimized LW				

3.2.3 Integrated Forecasting System (IFS) - ECMWF

As part of the CORSO project, progress has been made towards implementation of forward modelling capacity for atmospheric potential oxygen (APO) and radiocarbon in the Integrated Forecasting System (IFS). The IFS is used operationally at ECMWF for Numerical Weather Prediction and for air pollution and greenhouse gases for the Copernicus Atmosphere Monitoring Service (CAMS) (Flemming et al., 2015, Agustí-Panareda et al., 2022). The model has 137 hybrid sigma-pressure levels from the surface to 0.1 hPa with a vertical resolution that varies with (geometric) height and is highest in the planetary boundary layer. Tracer advection is calculated with an efficient semi-Lagrangian scheme (Diamantakis and Magnusson, 2016, and a mass fixer is subsequently applied to ensure mass conservation (Agustí-Panareda et al., 2017). The transport model additionally includes parameterizations of turbulent mixing (Sandu et al., 2013) and convection (Bechtold et al., 2014). The forward model is run with a time step of 15 minutes. The horizontal resolution of the IFS forward model depends on the model configuration: the reactive-species and aerosol configuration and the greenhouse gas forecasts within CAMS run at a spatial resolution of 40 km and 25 km, respectively.

The implementation of APO and radiocarbon in the IFS is closely coupled to the greenhouse gas configuration (Agustí-Panareda et al. 2014). The surface fluxes used for CO_2 (in IFS Cy49r1) are Jena CarboScope v2020 for ocean fluxes, CAMS-GLOB-ANT for anthropogenic emissions, and GFAS v1.4 for fire emissions. Biogenic GPP and ecosystem respiration are simulated online in ECLand, with a bias correction applied to ecosystem respiration to avoid large-scale drifts in simulated atmospheric CO_2 (Agustí-Panareda et al. 2016). More detail can be found in the IFS documentation on the land surface scheme and atmospheric composition (ECMWF, 2024ab).

The implementation of APO in IFS is based on the implementation in TM5 presented above, but with some differences. Separate tracers are used to simulate the contributing fluxes, and the deviations in these tracer fields resulting from these fluxes are combined to obtain the total $\delta(APO)$ signal in a postprocessing step. We use the Jena CarboScope ocean flux and the GridFED O_2 flux database for the anthropogenic component. The biogenic O_2 flux is simulated by applying a fixed biogenic exchange ratio of 1.1 to the biogenic CO_2 fluxes simulated online in IFS. O_2 consumption from fires is calculated by applying a fixed exchange ratio of 1.1 to GFAS fire CO_2 emissions. Initial development of the radiocarbon implementation has been performed by including the biogenic and oceanic disequilibrium fluxes and the cosmogenic production from Basu et al. (2020) as prescribed fluxes. Fossil fuel fluxes in this implementation are taken from CAMS-GLOB-ANT (Soulie et al. 2024). Future development steps for these schemes includes the incorporation of CORSO products (e.g. the scaled CESM2 ocean O_2 flux product or the CORSO LPJ-GUESS ^{14}C isotopic signatures) into the IFS.

3.3 Regional systems

3.3.1 The Lund University Modular Inversion Algorithm (LUMIA)

LUMIA is a Python-based framework designed for regional atmospheric inverse modeling. Its modular structure allows the estimation of greenhouse gas fluxes, such as fossil fuel CO_2 emissions and natural CO_2 exchanges, by assimilating *in situ* atmospheric observations within a Bayesian optimization framework (Monteil & Scholze, 2021). The algorithm minimizes a cost function that balances the fit to observations with deviations from prior flux estimates, providing a statistically consistent way to refine fluxes at regional scales.

Its modular architecture allows different components (e.g. transport models, boundary conditions, and inversion configurations) to be interchanged without altering the core framework. This flexibility supports both synthetic experiments and inversions using real observations, and enables the integration of the background component either through a two-step scheme with global TM5-4DVar or by sampling background concentrations from global datasets via Lagrangian footprints.

LUMIA's modular architecture also supports multi-tracer applications. In this project, it is used to jointly assimilate CO_2 and $\Delta^{14}CO_2$ (Gómez-Ortiz et al., 2025a; 2025b), enabling the simultaneous optimization of fossil fuel emissions and natural CO_2 fluxes. LUMIA has also been configured to perform inversions using the fossil fuel inversion framework, allowing fossil fuel CO_2 enhancements derived from $\Delta^{14}CO_2$ to be directly integrated into the optimization framework.

Table 4 provides an overview of the inversions, methods, and input datasets used in LUMIA for the CORSO project. Three types of inversions are carried out:

1. CO_2-only: a conventional CO_2 inversion that optimizes only net ecosystem exchange (NEE),
2. CO_2-$\Delta^{14}CO_2$: a dual-tracer inversion that jointly optimizes fossil fuel emissions, NEE, and terrestrial disequilibrium fluxes, and
3. ffCO_2-only: a fossil fuel inversion that assimilates C_{ff} pseudo-observations to estimate fossil fuel emissions.

In the first set of inversions, all three inversion approaches are performed, using 2021 as a base year to prepare the system for the 2024 $\Delta^{14}CO_2$ intensive flask sampling campaign. The CO_2-only inversions are used to assess the "carry-on" bias that arises when fossil fuel emissions are prescribed, as shown by Basu et al. (2016). The fossil fuel inversion configuration is evaluated alongside the dual-tracer inversion as a lightweight alternative that requires fewer computational resources and can be used for rapid testing.

Beyond the 2021 reference year, additional inversions are conducted to incorporate the results of the 2024 $\Delta^{14}CO_2$ intensive sampling campaign and to produce a consistent multi-year reconstruction of fossil fuel emissions. For 2015-2024, only the fossil fuel inversion configuration is applied, using precomputed ffCO_2 observations to optimize fossil fuel emissions. For 2024, a full dual-tracer inversion is performed, assimilating the CO_2 observations and the flask $\Delta^{14}CO_2$ samples collected during the campaign.

Together, these inversion setups enable (i) evaluation of methodological differences between CO_2-only, dual-tracer, and fossil fuel inversion approaches, (ii) production of a multi-year fossil fuel emission time series, and (iii) integration of the 2024 $\Delta^{14}CO_2$ campaign results into a coherent regional inversion framework.

Table 4. Overview of the inversions, methods, and input datasets used in LUMIA for the CORSO project.

Inversion period	Inversion approach	Prior fossil fuel product	Optimized fluxes	Observations[4]	Background
2021 (1 inversion per approach and per prior fossil fuel)	CO_2-only	CTE-HR[1] EDGARv4.3[2] ODIAC[3]	F_{bio}	CO_2 observations at midday	CO_2: Interpolated last particle position from CAMS[5].
	CO_2-$\Delta^{14}CO_2$		F_{ff}, F_{bio}, F_{biodis}	CO_2 observations at midday $\Delta^{14}CO_2$ integrated and flask	CO_2: Interpolated last particle position from CAMS[5]. $\Delta^{14}CO_2$: Smoothed data from MHD using NOAA's curve fitting function[6].
	$ffCO_2$-only		F_{ff}	Precomputed $ffCO_2$ from CO_2 and $\Delta^{14}CO_2$ integrated and flask samples	$\Delta^{14}CO_2$: Smoothed data from MHD using NOAA's curve fitting function[6].
2015-2024	$ffCO_2$-only	EDGARv4.3[2] (2015-2017) CTE-HR[1] (2018-2024)	F_{ff}	Precomputed $ffCO_2$ from CO_2 and $\Delta^{14}CO_2$ integrated and flask samples	$\Delta^{14}CO_2$: Smoothed data from JFJ using NOAA's curve fitting function[6].
2024	CO_2-$\Delta^{14}CO_2$	CTE-HR[1]	F_{ff}, F_{bio}, F_{biodis}	CO_2 observations at midday $\Delta^{14}CO_2$ integrated and flask samples	CO_2: Interpolated last particle position from CAMS[5]. $\Delta^{14}CO_2$: Smoothed data from JFJ using NOAA's curve fitting function[6].

[1]van der Woude (2022).
[2]Koch & Gerbig (2025).
[3]Oda & Maksyutov (2023).
[4]ICOS RI et al. (2025).
[5]CAMS (2020).
[6]https://gml.noaa.gov/ccgg/mbl/crvfit/crvfit.html, last access: 18 November 2025.

3.3.2 Regional Hierarchical Inverse Modelling Environment (RHIME)

RHIME has been frequently used for regional trace gas inversions of various atmospheric species across the globe (e.g., Ganesan et al., 2014; Say et al., 2021; Western et al., 2022). Here, RHIME has been adapted for constraining fossil fuel CO_2 emissions estimates from atmospheric flask samples of CO_2 and $\Delta^{14}CO_2$, and separately from atmospheric observations of APO (formed from concurrent flask samples of atmospheric CO_2 and $\delta(O_2/N_2)$).

RHIME uses a MCMC (Markov Chain Monte Carlo) approach to quantify a mean multiplicative scaling (with confidence intervals) of a priori fluxes for each sector of interest. For the $\Delta^{14}CO_2$-CO_2 inversions, an estimate of fossil fuel emissions and the terms that comprise β (the terrestrial biosphere correction split between GPP and respiration, and the nuclear power plant contributions) were inferred from atmospheric observations.

For the APO inversions, we assume terrestrial biosphere APO fluxes are entirely masked out through the construction of APO. We therefore used RHIME to infer fossil fuel APO emissions and oceanic APO fluxes from the observations. We assumed that any land-based fluxes are entirely fossil fuel in origin and any offshore fluxes are from ocean-atmosphere exchanges.

3.3.2.1 RHIME radiocarbon setup

The NAME-RHIME simulations used a similar approach as LUMIA, but with some key differences. Atmospheric observations of $\Delta^{14}CO_2$-CO_2 were combined following the mass balance approach in Section 3.1.1. Instead of applying the β correction to the observations to derive an estimate for fossil fuel CO_2, we keep β on the right hand side,

$$\left(\frac{\Delta_a - \Delta_{bg}}{\Delta_f - \Delta_{bg}}\right) C_a = C_f + \left(\frac{\Delta_r - \Delta_{bg}}{\Delta_f - \Delta_{bg}}\right) C_r + \left(\frac{\Delta_{gpp} - \Delta_{bg}}{\Delta_f - \Delta_{bg}}\right) C_{gpp} + \left(\frac{1}{\Delta_f - \Delta_{bg}}\right) A_{nuc}$$

to reduce any potential biases introduced to the observations when correcting for β.

Each term on the right hand side of this equation was optimised in RHIME. EDGAR (Emissions Database for Global Atmospheric Research) v8.0 fossil fuel emissions were used as the fossil fuel emissions a priori estimate; terrestrial biosphere CO_2 fluxes from ORCHIDEE v2.2, VPRM (Vegetation Photosynthesis and Respiration Model; v2023) and LPJ were used and compared; terrestrial biosphere $\Delta^{14}CO_2$ estimates from LPJ were used; and interpolated measurements of atmospheric $\Delta^{14}CO_2$ from Jungfraujoch that were representative of northern hemispheric variations were used as the background $\Delta^{14}CO_2$ estimate. Nuclear power plant emissions estimates were taken from RADD (for European power plants) and RIFE (for UK power plants). Fluxes were combined with footprints produced from the UK Met Office's Numerical Atmospheric transport Modelling Environment (NAME v8.2; Jones et al., 2007) to simulate background-subtracted mole fractions (as described in White et al., 2019). These simulations were then combined as shown in the above equation.

An a priori emissions uncertainty probability density function (PDF) is assigned to each flux sector. For the fossil fuel emissions, this was ~TN(1,0.15^2); for the terrestrial biosphere isofluxes these were ~TN(1,2.0^2) for GPP and respiration; and for the nuclear power plants this was ~TN(1,1.0^2). All PDFs were bounded as [0,∞] to prevent unrealistic, negative solutions. The nature of this approach means that the background $\Delta^{14}CO_2$ estimates (Δ_{bg}) are not independently optimised in the inversion, but rather form part of the flux sector

optimisations. The crucial point being that RHIME optimises the isofluxes for each sector rather than just the CO_2 flux. For fossil fuel CO_2, the emissions themselves are optimised, but the terrestrial biosphere CO_2 fluxes are entangled with their $\Delta^{14}CO_2$ values and Δ_{bg}.

3.3.2.2 RHIME APO setup

Since atmospheric inversions are being performed in "APO-space" (as in Rodenbeck et al. 2023) sectoral flux field estimates for CO_2 and O_2 need to be combined to create APO flux fields. This was guided by the definition of APO in Section 3.1.2 and used the approach presented in Rodenbeck et al. (2023). Only fossil fuel and ocean APO fluxes were used in the model since, by construction, there are theoretically no APO fluxes from the terrestrial biosphere.

Fossil fuel fluxes of CO_2 are related to O_2 fluxes by their molar exchange ratio, α_f such that $F_f{}^{O2} = -\alpha_f F_f{}^{CO2}$.

From the definition of APO and the above equation, the fossil fuel APO flux field is defined as

$$F_f{}^{APO} = -(\alpha_f + \alpha_l) F_f{}^{CO2}.$$

Here, α_l is the CO_2:O_2 molar exchange ratio for the land biosphere and takes a value of 1.1.

Monthly fossil fuel CO_2 fluxes from EDGAR v8.0 (Crippa et al., 2021) were combined with fossil fuel CO_2:O_2 molar exchange ratios from the GridFED v2024 database (Jones et al. 2021) to construct fossil fuel APO flux fields. EDGAR provides 0.10ºx0.10º global anthropogenic CO_2 emissions estimates from 1970-2023 which were regridded using a mass-conservation approach to match the NAME footprint domain and spatial resolution. For 2024, the 2023 emissions field was used.

Ocean APO fluxes were similarly constructed from flux fields of CO_2, O_2, and N_2. Keeling and Manning (2014) demonstrated that a first order approximation of $\delta(O_2/N_2)$ oceanic fluxes can be modelled as

$$Z_{eff} = Z_{o2} - \frac{X_{O2}}{X_{N2}} \times Z_{N2}.$$

Here, Z_{O2} and Z_{N2} are the respective O_2, and N_2 net ocean-atmosphere flux exchanges. X_{O2} and X_{N2} are the reference oxygen and nitrogen standard values, respectively. A value of 0.79019 is used for X_{N2}.

Combined with the net ocean-atmosphere CO_2 flux exchange, Z_{CO2}, we can model oceanic APO fluxes as

$$F_{oce}{}^{APO} = Z_{eff} - \alpha_l Z_{CO2}.$$

Like Chawner et al. (2024), we used oceanic CO_2, O_2, and N_2 flux fields from NEMO-ERSEM (Butenschön et al., 2016; Madec and NEMO System Team, 2022), which were combined into an APO oceanic flux following the above equation for ocean APO fluxes. The NEMO-ERSEM

ocean fluxes have a daily time resolution and raw spatial resolution of 0.066ºx0.110º, which were also regridded using a mass-conservation approach to match the NAME domain and spatial resolution. Since NEMO-ERSEM fluxes were only available until 2015, we used the 2015 fluxes to model the oceanic APO fluxes for 2022-2024.

As the focus of this study was to use APO observations to constrain land-based fossil fuel CO_2 emissions estimates, using an outdated version of the ocean fluxes is less problematic provided a sufficiently large uncertainty is assigned to these fluxes in the inversion, and the ocean and land parts of the inversion domain are optimised using separate basis functions with distinct land and sea areas that do not overlap. Furthermore, we did not find a statistically significant trend in the NEMO-ERSEM ocean fluxes in the model domain over 2005-2015 (the period we had data available).

The Jena Carboscope (JC) inverse model (Rodenbeck et al. 2023) produced daily global estimates of APO values for 2002-2021 from global inversions of APO observations from 11 global stations and ship measurements (JC version ``apo99XS_v2022''). The global stations used in this model do not include any of the ICOS measurement stations used in the RHIME regional inversion. The JC APO values were extrapolated to 2024 at three latitudinal bands (30ºN-90ºN; 30ºS-30ºN; 90ºS-30ºS) using a linear regression applied to the 2017-2021 APO values. From this linear regression, we detrended the JC APO values and propagated the 2017-2021 mean APO seasonal cycle forwards in time to provide daily APO value estimates for 2022-2024. Whilst extrapolation can introduce large uncertainties into the data and is generally not recommended, this was the best approach we had at the time. The JC APO values formed the boundary condition fields along the edges of the NAME model domain for each month. Boundary conditions were calculated using the NAME particle density at the edge of the model domain (see below). A scaling is calculated for each cardinal boundary in each 1-month period of inference to derive posterior boundary condition values.

A priori emissions uncertainty PDFs were assigned to each APO flux sector and to the background APO values. For the APO fossil fuel flux, this was ~TN(1,0.35^2) bounded at [0,∞) to prevent unrealistic, negative solutions; for the ocean APO flux this was ~N(1,6.0^2); and for the background APO ~N(1,0.08^2).

3.3.2.3 RHIME setup

In both sets of inversions, the modelling domain is split into 55 scaling regions (basis functions) for each flux sector. The scaling regions over Europe (30ºW–42ºE longitude and 29ºN–77ºN latitude) are not spatially fixed and are recalculated for each month. Scaling regions in the rest of the inversion domain are always spatially fixed. The geographical coverage of each scaling region in Europe is calculated from multiplying the mean footprint field with the converging estimated absolute flux field for each month. The inversion domain is split (with land and sea areas kept distinct in each scaling region) such that summing the grid cells in each scaling region yields approximately the same footprint-flux value. Scaling regions closer to the measurement stations encompass fewer grid cells (and a smaller geographical area) than those much further away which encompass larger geographical areas.

The model-data uncertainties were calculated as the sum in quadrature of the observational uncertainty and the model uncertainty. The model uncertainty was taken as the median simulation-observation residual for the inversion period.

Like Saboya et al. (2024), we used a No-U-Turn (NUTS) sampler (Hoffman & Gelman, 2014) to sample from the posterior PDF. The samplers used a total 8000 iterations (discarding the first 1000) with two chains running in parallel. A Gelman-Rubin diagnostic is used to check for parameter convergence in both chains.

Inversions were performed over four-month periods from 2022-2024 for $\Delta^{14}CO_2$-CO_2. There was not enough data pre-2024 for RHIME to converge to a mean scaling value for smaller time periods, no matter the length of the chain. For APO, monthly inversions were performed for 2024 as there were more data available than for $\Delta^{14}CO_2$.

4 Results

4.1 Global decadal scale

4.1.1 CIF-LMDZ results (LSCE)

The results of the inversion using the CIF-LMDZ variational inversion framework, co-assimilating CO_2 and $\Delta^{14}CO_2$ over the period from January 1998 to December 2024 with a transport and control horizontal resolution of 1.3° latitude x 2.5° longitude, show the system is able to assimilate and reproduce observed CO_2 and $\Delta^{14}CO_2$ observations within the control framework. This system shows significant improvements from previous iterations of the model as described in Milestone Report 7, namely in the assimilation of radiocarbon and in the control of its isotopic signatures. The main explanations are the increase of the resolution of the CIF-LMDz configurations compared to the earlier version of the system, improvements in the definitions of the observation errors, and a better filtering of the observations to be assimilated, including a shift of the coastal sites in the sea when modelling them. As a result, the inversion cost function is far less focused on a few CO_2 time series at sites poorly modeled with the coarse initial configuration, and it better matches the overall ensemble of CO_2 and $\Delta^{14}CO_2$ timeseries. The control of the isotopic signatures also enhanced the ability to fit both CO_2 and $\Delta^{14}CO_2$ timeseries. An analysis and discussion of the different components of the inversion results is given below.

Figure 1 and Figure 3 show the results of the inversion in the form of a time series of the observations and simulations for CO_2 and $\Delta^{14}CO_2$, respectively, for a select subset of eight stations over the period of the simulation (1998-2024). These eight stations were selected as representative of the global distribution of CO_2 and $\Delta^{14}CO_2$ due to their varying locations from high northern latitudes (ALT), northern mid-latitudes (CBW, KRE, JFJ, MHD), mid-latitudes (MLO), southern mid-latitudes (BHD) and high southern latitudes (SPO). The stations include a mix of background locations (ALT, MLO, SPO), background locations with some occasional urban influence (BHD, JFJ, MHD), and more urban influenced locations (CBW, KRE). As a result, the stations show a mix of which flux mostly likely dominates the local CO_2 and $\Delta^{14}CO_2$ concentrations.

For all the stations simulated, the results show a much-improved fit to the CO_2 observations for the posterior simulation when compared with the prior simulation. Prior CO_2 is generally able to capture the seasonality of observed CO_2 but generally shows a higher growth rate, leading to an overestimation at most stations included in the model. The largest discrepancies between prior CO_2 and observations occur in the second decade of the simulation as the higher CO_2 growth rate compounds over time (Figure 1). The posterior CO_2 is better able to capture the observed CO_2 after 12 iterations of the variational scheme, maintaining the

seasonality while improving the growth rate to match the observations even at the end of the simulation period.

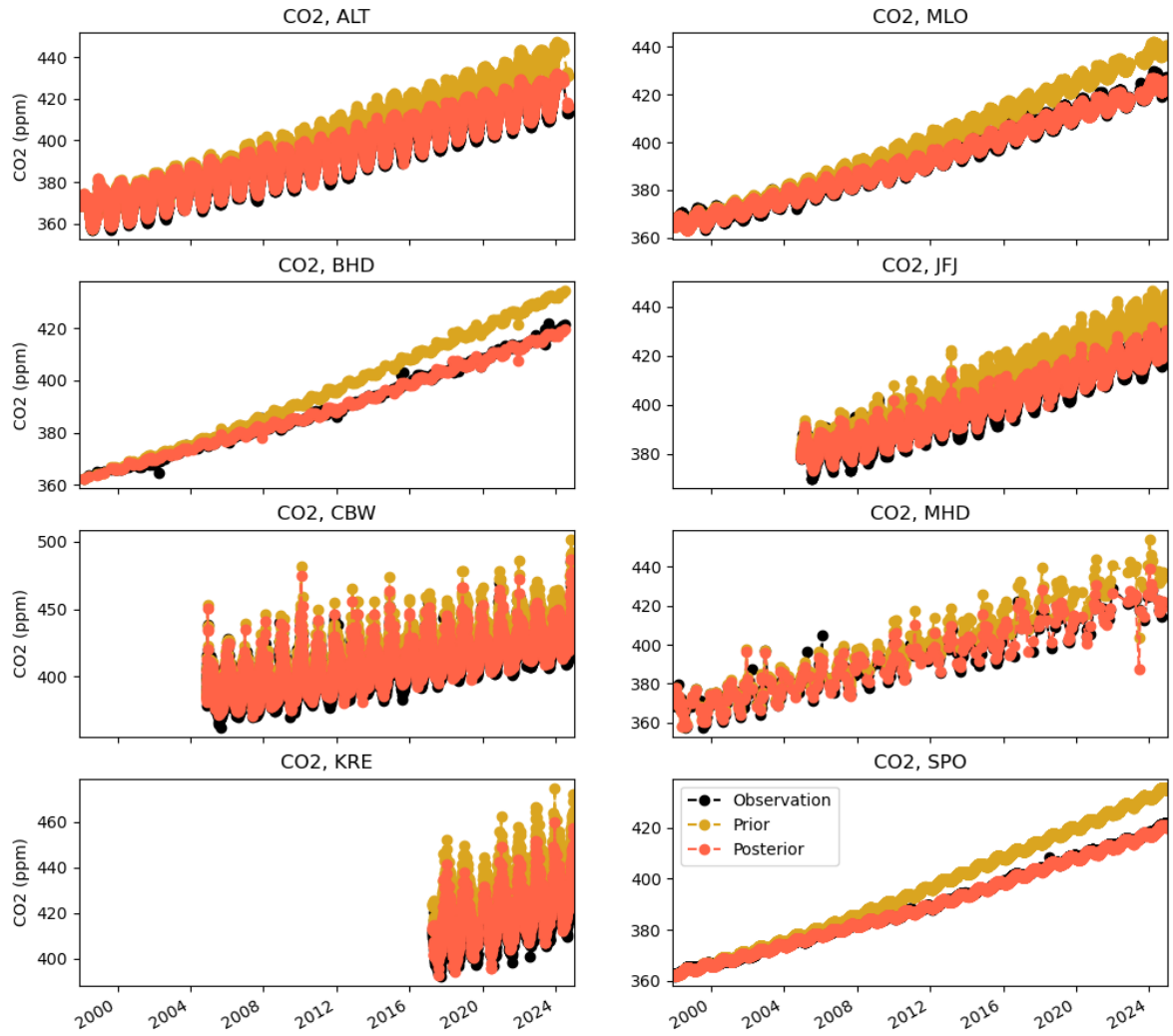

Figure 1: Time series of the daily average CO_2 observations and their prior and posterior simulations using CIF-LMDZ for a subset of eight stations used in the standard resolution configuration of the model. The stations are located at Alert, Canada (ALT); Bearing Head, New Zealand (BHD); Cabauw, Netherlands (CBW); Křešín u Pacova, Czechia (KRE); Mauna Loa, Hawaii, USA (MLO); Jungfraujoch, Switzerland (JFJ); Mace Head, Ireland (MHD); and South Pole, Antarctica (SPO).

The improvement in the posterior CO_2 is further illustrated in Figure 2, which shows the average RMSE of each station for the prior and posterior simulations. There are a total of 149 stations included in the simulation that were used to assimilate CO_2 observations. Each station shows a lower RMSE for the posterior estimate when compared to the prior estimate, indicating the better fit of the posterior CO_2 to the observations at every station simulated and suggesting that the inversion system was able to adequately assimilate the CO_2 observations.

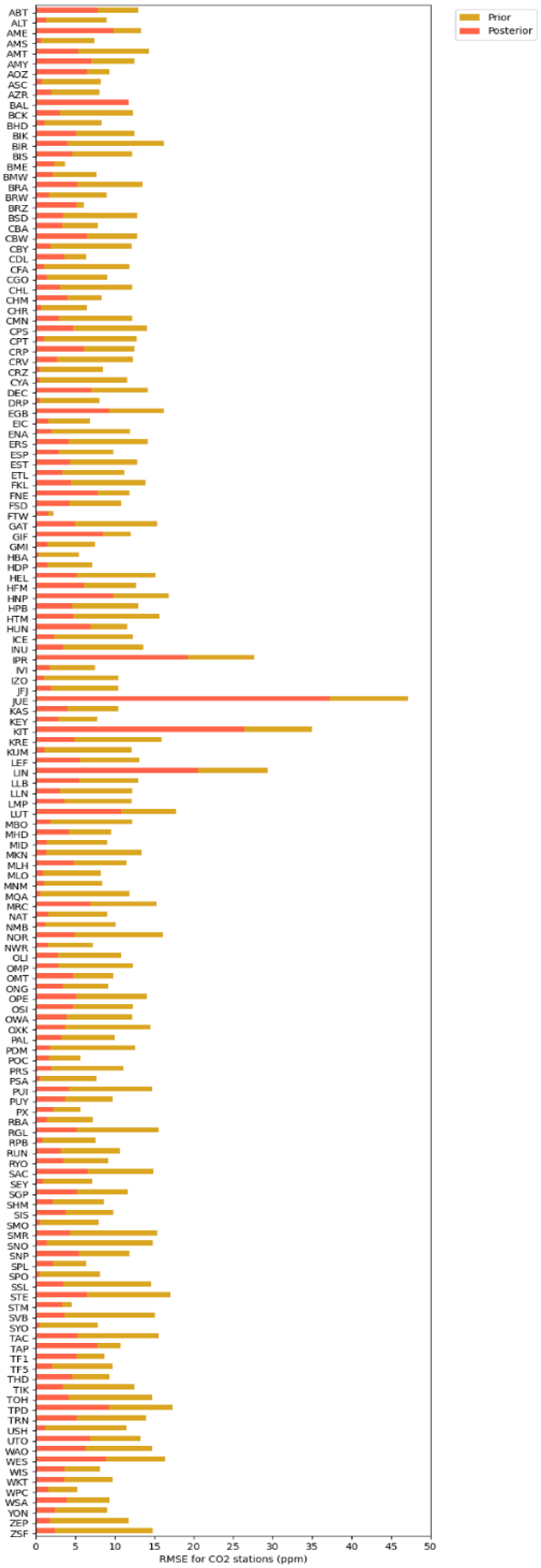

Figure 2: The average RMSE (in ppm) of the prior and posterior CO_2 simulations for each CO_2 station included in the model (149 total).

In the same vein as the results for CO_2, the results for $\Delta^{14}CO_2$ show a much-improved fit to the $\Delta^{14}CO_2$ observations for the posterior simulation when compared to the prior simulation. In the prior simulation, $\Delta^{14}CO_2$ is largely underestimated with values significantly lower than atmospheric observations over most of the simulation period indicating a lower growth rate of $\Delta^{14}CO_2$ in the model than is observed in the atmosphere. This lower growth rate compounds over the 25+ year simulation period, leading to a larger discrepancy between the prior simulation and the observations as time goes on (Figure 3). Both CO_2 and $\Delta^{14}CO_2$ thus show growth rates that differ from observations, but their respective growth rates have opposite trends in the model. The slow growth rate has been largely corrected after 12 iterations of the variational scheme and the posterior $\Delta^{14}CO_2$ matches much more closely with the observations (Figures 2 and 3). However, the posterior simulated $\Delta^{14}CO_2$ does not fully capture the seasonality patterns seen in the atmospheric observations, most notably at the remote stations, despite the improvement in the posterior atmospheric $\Delta^{14}CO_2$ growth rate.

The significant improvement in the posterior $\Delta^{14}CO_2$ compared to the prior $\Delta^{14}CO_2$ simulation is consistent across all the stations simulated. Figure 4 shows the average RMSE for prior and posterior $\Delta^{14}CO_2$ estimates for the 40 stations from which $\Delta^{14}CO_2$ was assimilated in the model. The RMSE is decreased across all stations by a factor of at least 2, and in some cases by a factor of 10, indicating the better fit of the posterior $\Delta^{14}CO_2$ to the observations compared to the fit of the prior $\Delta^{14}CO_2$ to the observations. This improvement represents crucial progress from the Milestone 7 report.

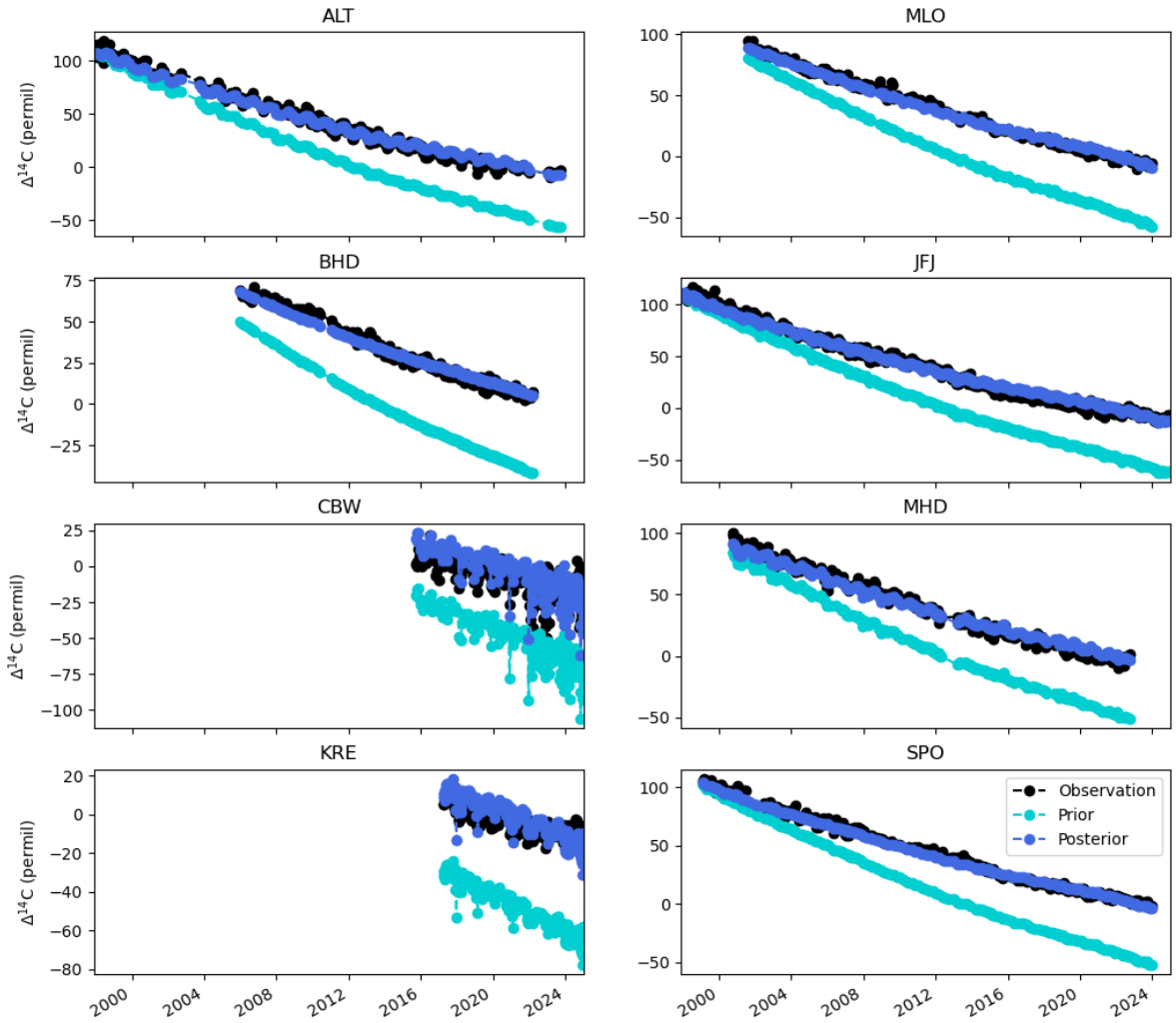

Figure 3: Time series of the integrated and flask $\Delta^{14}CO_2$ observations and their prior and posterior simulations using CIF-LMDZ for a subset of stations used in the standard resolution configuration of the model. The stations are located at Alert, Canada (ALT); Bearing Head, New Zealand (BHD); Cabauw, Netherlands (CBW); Křešín u Pacova, Czechia (KRE); Mauna Loa, Hawaii, USA (MLO); Jungfraujoch, Switzerland (JFJ); Mace Head, Ireland (MHD); and South Pole, Antarctica (SPO).

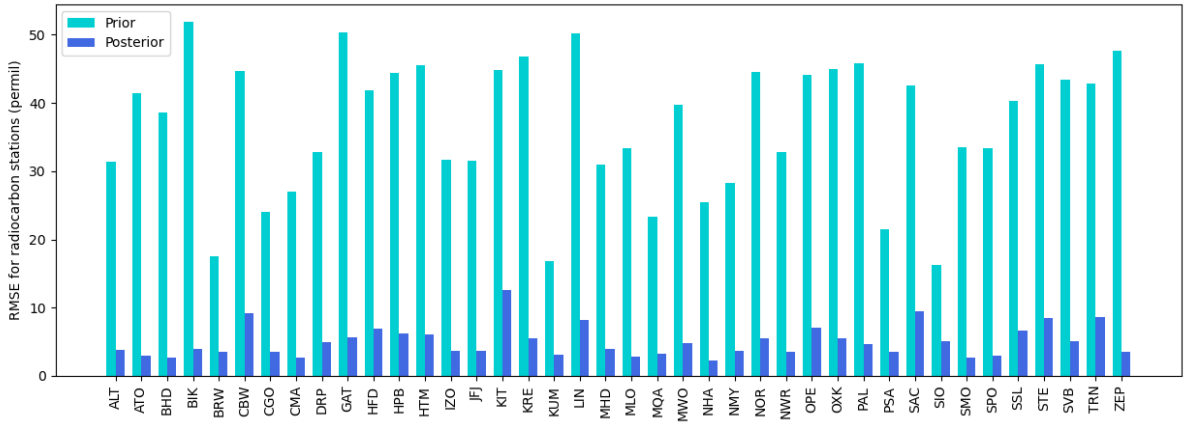

Figure 4: The average RMSE (in per mil) of the prior and posterior simulations of $\Delta^{14}CO_2$ for each of the stations included in the model (40 total).

Figure 5 shows the inversion results as a time series of the globally averaged annual prior and posterior CO_2 flux estimates over the simulation period (1998–2024) for the three main source categories: net ocean fluxes (OCE), net biosphere fluxes (NEE), and fossil-fuel emissions. In these flux estimates, NEE shows the largest difference between the prior and the posterior estimates after 12 iterations of the variational configuration. The prior simulation of CO_2 displays an overestimation of the CO_2 growth rate in the atmosphere, due to the use of a 40-year climatological NEE (without inter-annual variability) poorly accounting for the regular increase of the natural sink, especially during the two past decades. The inversion largely corrects this bias by adjusting the terrestrial flux. The posterior NEE flux estimates exhibit significant adjustments during certain periods (notably 2008–2012 and 2018–2022) to compensate for the lack of variability in the prior estimates.

Overall, these results indicate that the inversion generally increases the global natural carbon sink. Most of the difference between the prior and posterior estimates of the total global flux arises from changes in the NEE (Figure 5), with an additional contribution from the slight decline in the posterior net-ocean flux. In contrast, the inversion produces very little adjustment to the fossil-fuel flux estimates at the global scale.

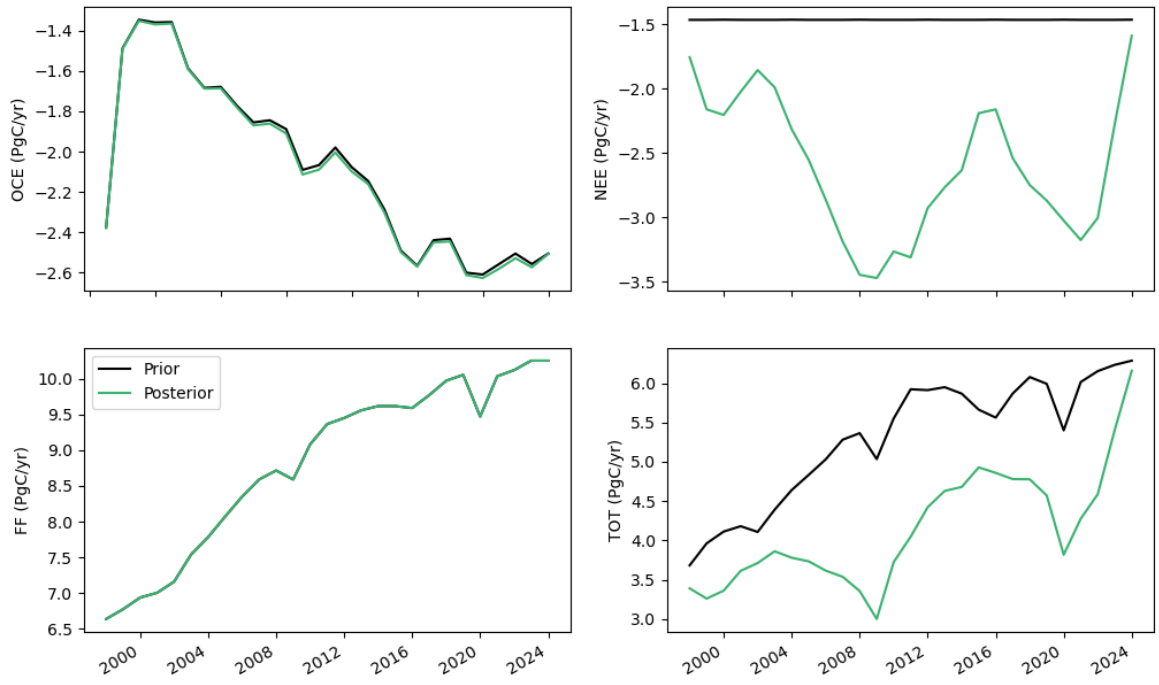

Figure 5: Global averaged annual prior and posterior CO_2 fluxes for the net oceans (OCE), net biosphere (NEE), fossil fuels (FF), and total (TOT) fluxes. Prior fluxes are shown in black and the posterior is in green.

A further look at the change in the fossil fuel CO_2 emissions over the whole analysis period from the inversion is provided by the map of increments in Figure 6. The value of the change is small, even locally, with less than 0.01% average change between the mean prior and posterior CO_2 fossil fuel emissions over the time of the inversion. The largest changes are clustered in areas with high fossil fuel emissions: there are slight decreases in the emissions estimates in Europe with some even smaller decreases along the eastern coast of North America and eastern Asia. Hence the multidecadal global inversion is primarily dominated by impact of the uncertainties in natural fluxes, even with the assimilation of the $\Delta^{14}CO_2$ observations in the system.

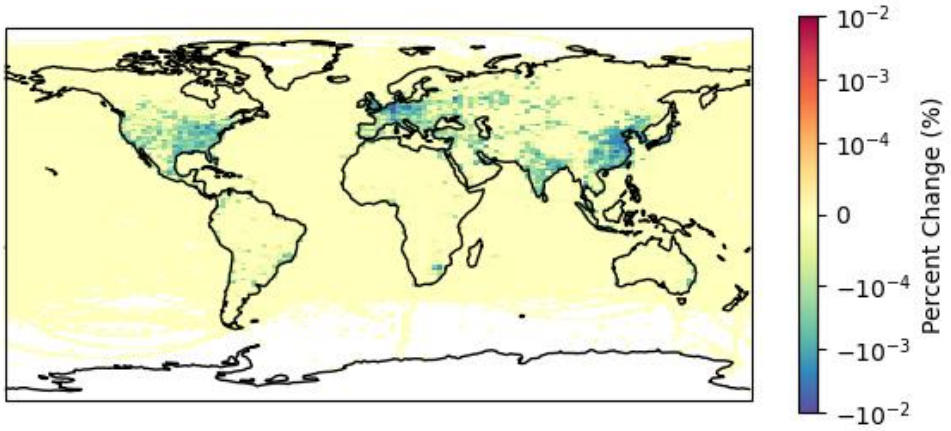

Figure 6: Map of the relative (percentage) change in fossil fuel emissions averaged over the period of the simulation (1998-2024) in the standard resolution configuration (with a logarithmic colorscale).

The inversion also applies significant corrections to the $\delta^{14}CO_2$ isotopic signatures of the individual gross components that comprise the natural fluxes. Figure 7 shows the global averaged prior and posterior isotopic signatures for the two gross components of each of the ocean and biosphere fluxes. The inversion makes slight adjustments to the isotopic signatures of NPP (decrease) and OA (increase) but the largest adjustment is in the isotopic signature of HR.

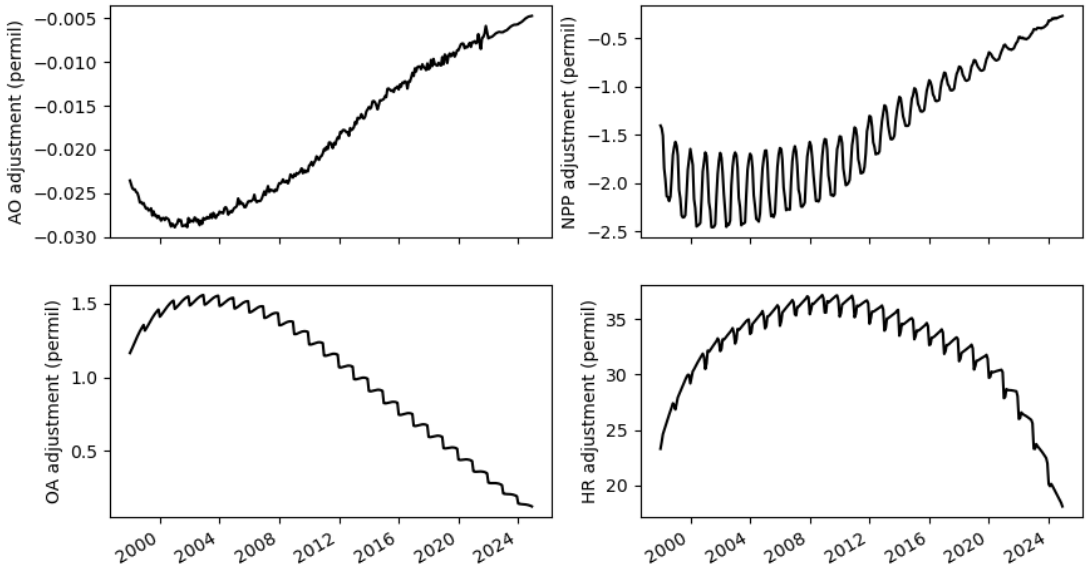

Figure 7: Global monthly averaged isotopic signature adjustment (posterior - prior) of $\delta^{14}CO_2$ for AO, OA, HR, and NPP. Note the different scales on the y-axis for each plot.

A sensitivity study was conducted to explore the effects of the prior estimate of the biosphere isotopic signatures on the model simulations of $\Delta^{14}CO_2$, given the importance of these fluxes in the global inversion. Two biosphere isotopic signature products were used: the first from the LPJ terrestrial biosphere model as described above and in Deliverable D3.4; the second from a prior study on $\delta^{14}CO_2$ by Wang, 2016 that used the ORCHIDEE terrestrial biosphere model to estimate HR and NPP isotopic signatures on a global scale resolution of 1.875°

latitude × 3.75° longitude over a period from 1990 to 2007 (inclusive). The details of the ORCHIDEE modeling of radiocarbon can be found in Wang, 2016. Briefly, the ^{14}C budget of the land biogenic CO_2 flux is calculated using an emulator of the ORCHIDEE-MICT model with 12 plant functional types, each with eight biomass pools, four litter pools, and three soil carbon pools. The biospheric $^{14}CO_2$ fluxes from ORCHIDEE-MICT are scaled together so that the global average decreasing trend in simulated $\Delta^{14}CO_2$ matches the mean trend from observed background atmospheric radiocarbon records from 1998 to 2007, as further described in Wang, 2016.

The results from the sensitivity study are shown in Figure 8, with the four different combinations of products for the HR and NPP isotopic signatures. The model shows some sensitivity to the NPP isotopic signature product with a slight change in the simulated $\delta^{14}CO_2$ depending on the product used. However, the HR isotopic signature plays a large role in the model's ability to match the $\delta^{14}CO_2$ observations and trend. Over a ten-year simulation period, the difference in HR isotopic signature between the two products leads to a difference of nearly 40 per mil in the simulated $\delta^{14}CO_2$ due to an average difference of about 45% in the HR isotopic signature between LPJ and ORCHIDEE. The use of the signature for HR from ORCHIDEE, whose $^{14}CO_2$ fluxes have been scaled to match the mean observed background trend, provides a good fit with the different background sites. In general, the ^{14}C in land biosphere pools and in CO_2 fluxes emitted by this reservoir to the atmosphere are highly uncertain (with more than 20% rescaling needed for the default simulations to fit the trends in observed background atmospheric radiocarbon records) as discussed in Randerson et al, 2002 and Naegler and Levin, 2009, and as shown by the 45% average difference between the HR isotopic signature from LPJ and ORCHIDEE. This uncertainty leads to potentially consequential discrepancies in simulations of $\Delta^{14}CO_2$ at the global level.

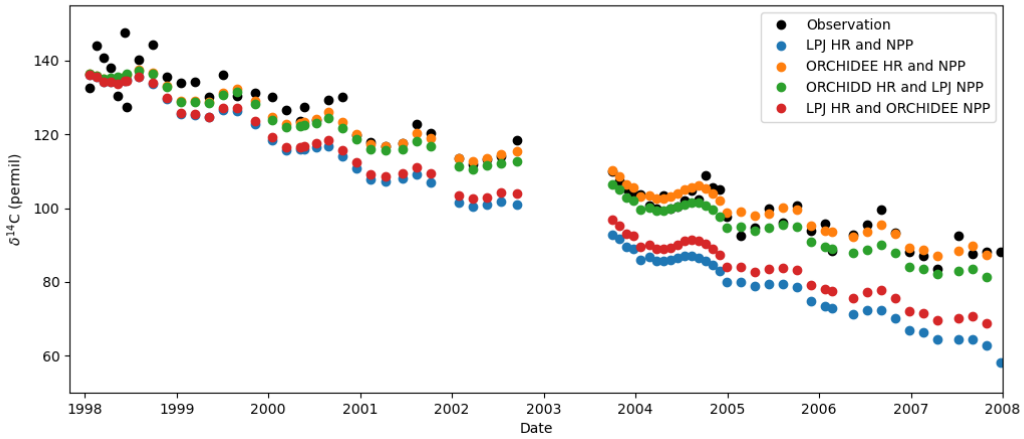

Figure 8: Time series of $\delta^{14}CO_2$ derived from different combinations of two different isotopic signature products for the HR and NPP from LPJ or ORCHIDEE. The data shown are the observations and simulations at Alert, Canada (ALT).

The CIF-LMDZ variational inversion framework was also configured to run the transport on a higher resolution grid of 0.7° latitude x 1.4° longitude over the period from January 2021 to December 2024 in order to take advantage of the intensive sampling of $\Delta^{14}CO_2$ performed in Europe during 2024 as part of CORSO (albeit keeping a control horizontal resolution of 1.3° latitude x 2.5° longitude). As with the standard transport resolution grid, the results of the inversion with transport at the higher resolution show the system can assimilate and reproduce observed CO_2 and $\Delta^{14}CO_2$ observations within the control framework within uncertainties. The results from this inversion, performed at the global scale but with the objective to focus on the European continent (defined as 35° to 70° in latitude and -25° to 40° in longitude).

Figure 9 shows the inversion results for atmospheric CO_2 and $\Delta^{14}C$ in the higher-resolution transport configuration at a selected subset of four European stations over the simulation period (2021–2024). The time series include data from two background stations (JFJ and PAS) and two stations with moderate urban influence (CBW and KRE). The latter two stations were among those that underwent intensive sampling in 2024.

These results similarly show a much-improved fit to the CO_2 and the $\Delta^{14}CO_2$ observations for the posterior simulation when compared to the prior simulation. The over-estimation of CO_2 and the under-estimation of $\Delta^{14}CO_2$ is evident in the time series in Figure 9, but the discrepancy is not as large as in Figure 1 and 3 due to the shorter timescale of this inversion. In both cases, the posterior CO_2 and $\Delta^{14}CO_2$ estimates are able to correct for the respective difference in simulated and observed growth rates after 19 iterations of the variational system. The posterior CO_2 and $\Delta^{14}CO_2$ thus match well with the observed CO_2 and $\Delta^{14}CO_2$ at each of the stations where these data are assimilated.

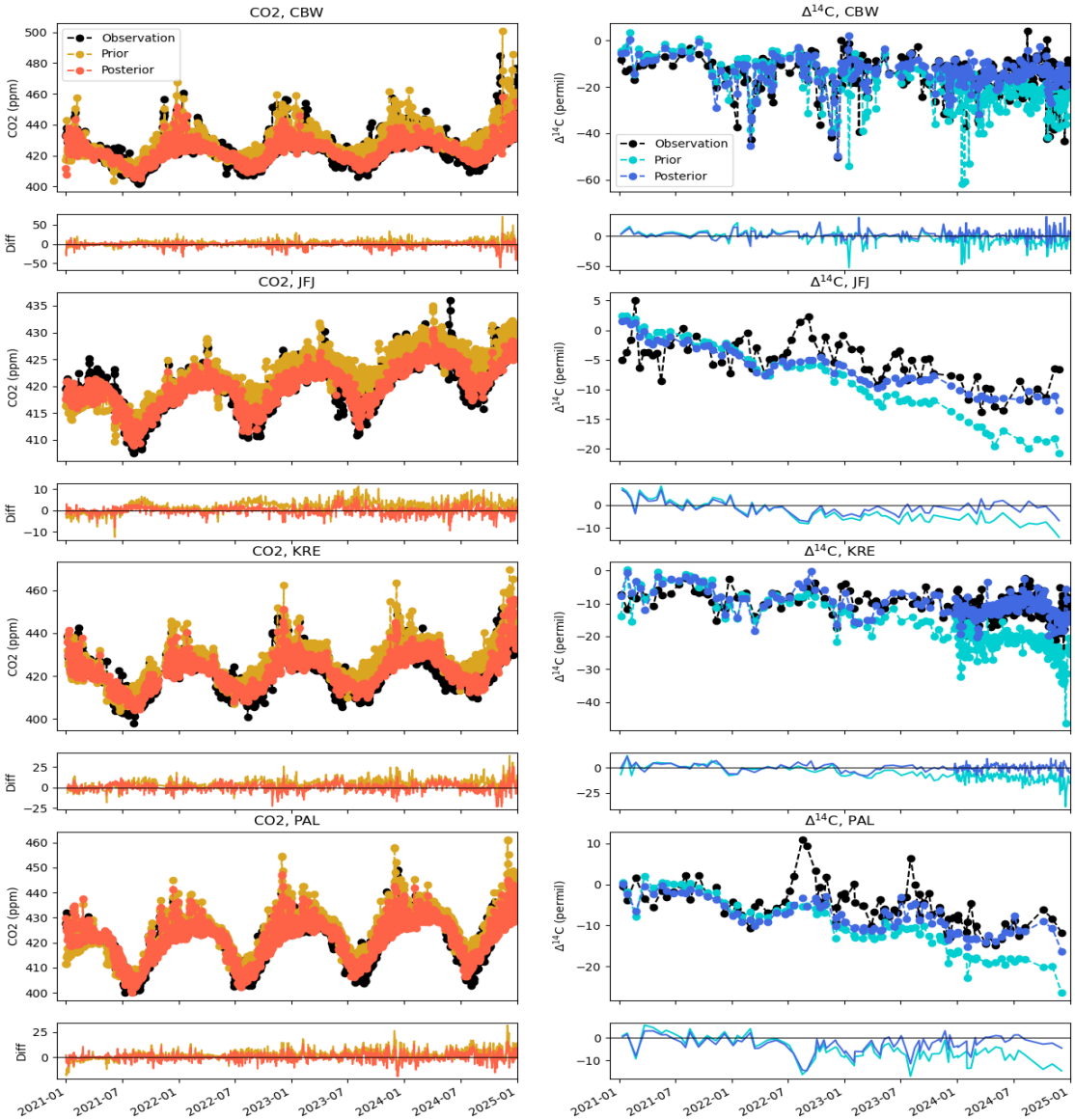

Figure 9: Time series of the daily average CO_2 and $\Delta^{14}CO_2$ observations compared with the prior and posterior simulations as well as the difference between the simulations and the observations ("Diff")

using CIF-LMDZ for a subset of four stations used in the higher resolution configuration of the transport model. The stations are located at Cabauw, Netherlands (CBW); Jungfraujoch, Switzerland (JFJ); Křešín u Pacova, Czechia (KRE); and Pallas, Finland (PAL).

Figure 10 shows the flux adjustments made by the inversion on monthly and annual timescales, spatially averaged over the European continent, when transport is performed with the higher-resolution configuration. These results correspond to iteration 19 of the variational inversion. Over this period and at this transport resolution, the inversion adjusts the NEE flux to reduce the CO_2 growth rate. However, in this configuration the inversion also exerts greater control over, and makes larger adjustments to, the ocean and fossil-fuel fluxes than in the longer-timeframe, standard-resolution configuration.

The average change in the fossil fuel fluxes over the 2021 to 2024 period and the European continent using the inversion configuration with a higher resolution transport is shown in Figure 11. This inversion indicates a larger adjustment to the fossil fuel fluxes, with changes on an average scale of about 5% over Europe. The changes are primarily in north-western Europe, in areas where the majority of $\Delta^{14}CO_2$ observations are located. There is a general decrease in posterior fossil fuel estimates in the region around Germany and a slight increase in the posterior estimates in the region around northern France and southern England.

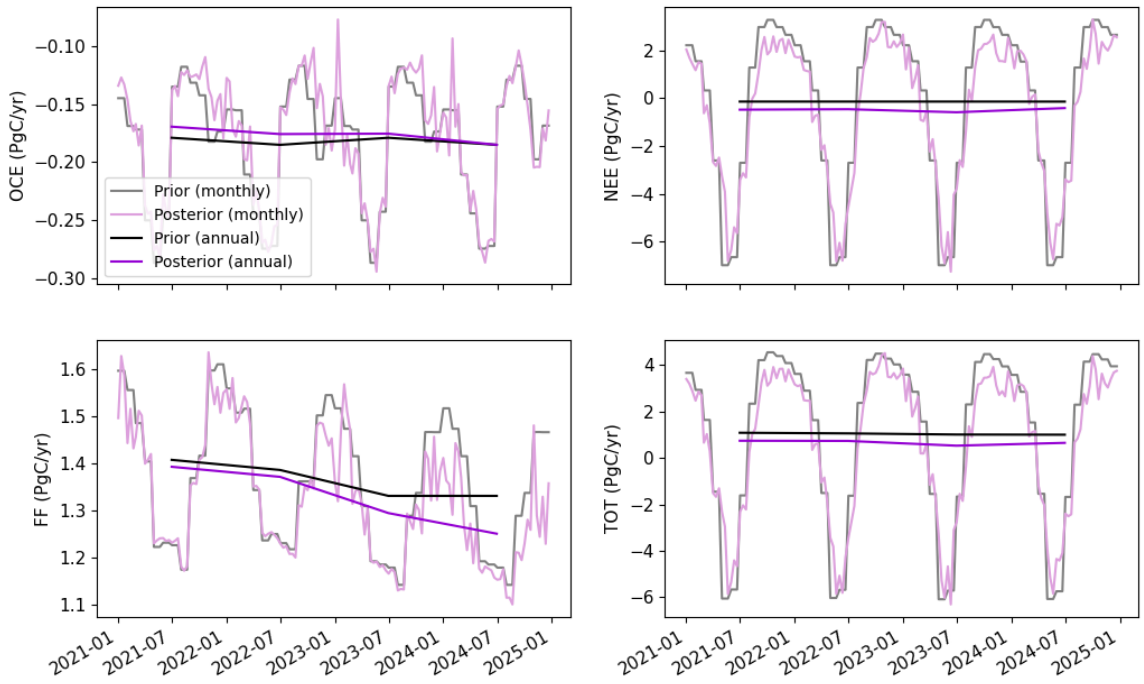

Figure 10: Monthly and annual prior and posterior CO_2 fluxes averaged over a European domain (35° to 70° in latitude and -25° to 40° in longitude) for the net oceans, net biosphere, fossil fuels, and total fluxes (when using the high resolution configuration of LMDZ).

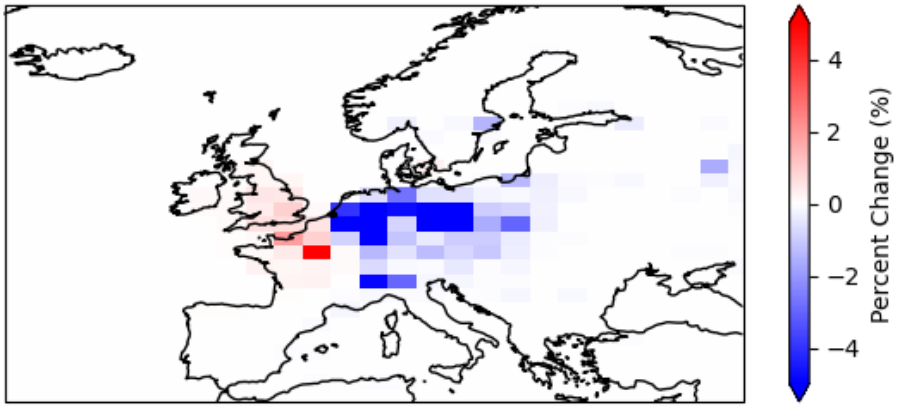

Figure 11: Map of the percentage change in fossil fuel emissions in Europe averaged over the time of the simulation (2021-2024) at 1.3° latitude x 2.5° longitude resolution (when using the high-resolution configuration of LMDZ).

4.1.2 CTE (Wageningen University)

With the CTE-LW-SW system, we have performed global inversions for the period 2000-2024, assimilating CO_2, $\Delta^{14}CO_2$ and $\delta O_2/N_2$. Figure 12 below shows the results for the comparisons of the three tracers to observations at the station Alert as an example. The Long-Window posterior matches the observations well for all three species.

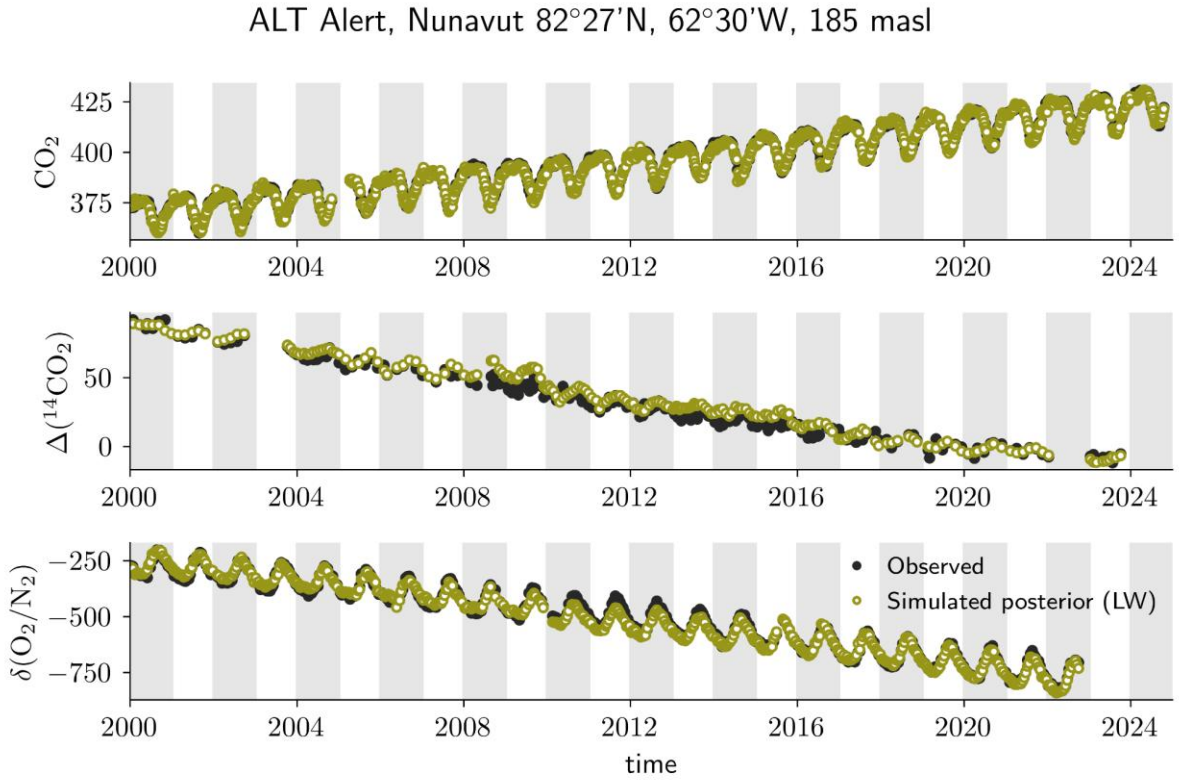

Figure 12: Simulated atmospheric CO_2 (top), $\Delta^{14}CO_2$ (middle) and $\delta O_2/N_2$ (bottom) at Alert for the period 2000–2024. The results shown are from simulations with posterior fluxes from the CTE Long Window system. A zoom of the final 5 years of this record is presented in Figure 15 below. Note that in the later years, there were less observations available for $\Delta^{14}CO_2$ and $\delta O_2/N_2$ at this location.

These posterior results improved much compared to a forward simulation of the prior fluxes (see Figure 13). Especially for $\Delta^{14}CO_2$, the deviation between prior simulations and observations is large, in this case for example at Alert, but this is also seen at other stations. This apriori imbalance is likely related to biases in the terrestrial and ocean disequilibrium flux. But it can also possibly be partly explained by too short spin-up time for this tracer. For $\Delta^{14}CO_2$, the cosmogenic production term leads to a large gradient between the stratospheric and tropospheric values absent in the starting boundary condition, and it takes time to see this signal at the surface stations. For $\delta O_2/N_2$, the prior simulation reproduces the observations already quite well, but the growing imbalance between the simulated and observed values is due to systematic underestimation of the global land and ocean sinks.

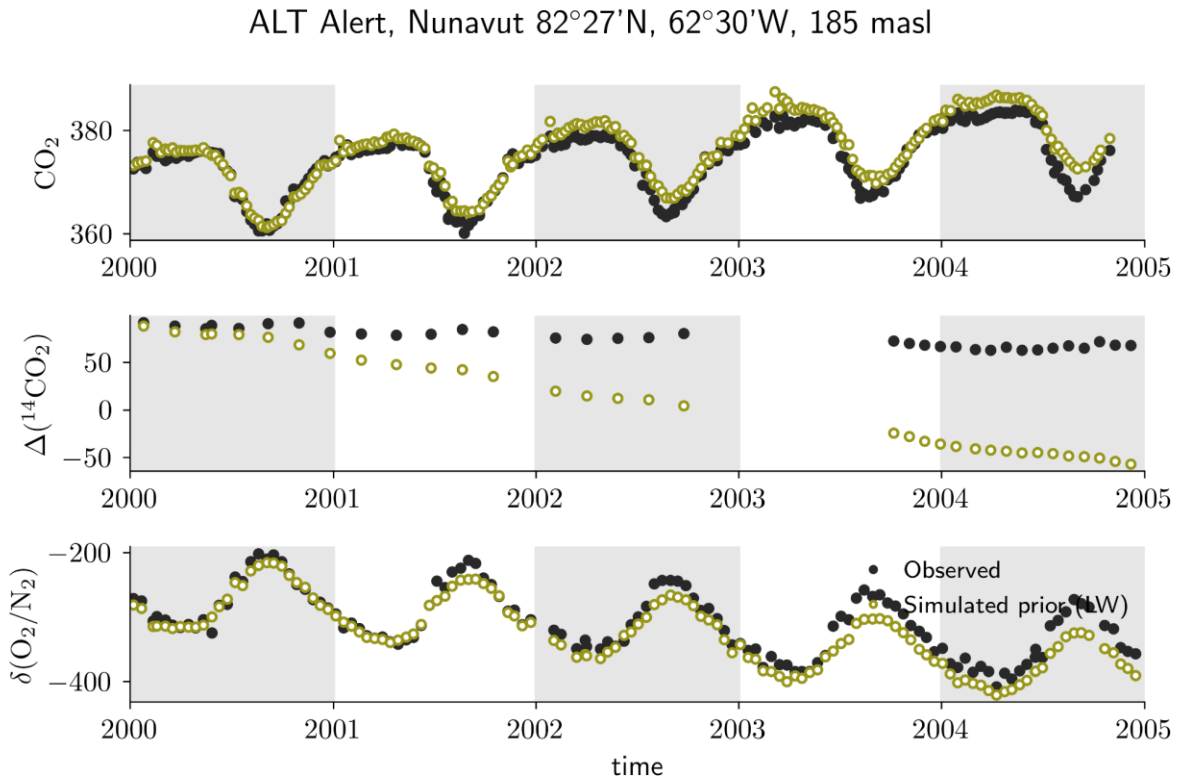

Figure 13: Simulated atmospheric CO_2 (top), $\Delta^{14}CO_2$ (middle) and $\delta O_2/N_2$ (bottom) from the prior fluxes using a forward simulation.

Figure 14 below shows the prior and posterior fluxes. In the global scale CTE Long Window system, all fluxes shown here were optimised. The figure shows that the disequilibrium fluxes for $\Delta^{14}CO_2$ are significantly adjusted, although with remaining uncertainty. We therefore decided to keep these fluxes fixed in the next experiments where we zoom in on Europe with the Short Window simulation. These disequilibrium fluxes might be improved by improving process based models, which could be part of a follow up study. $\delta O_2/N_2$ outgassing from the oceans is relatively well simulated in the prior already, and also kept fixed in the Short Window step.

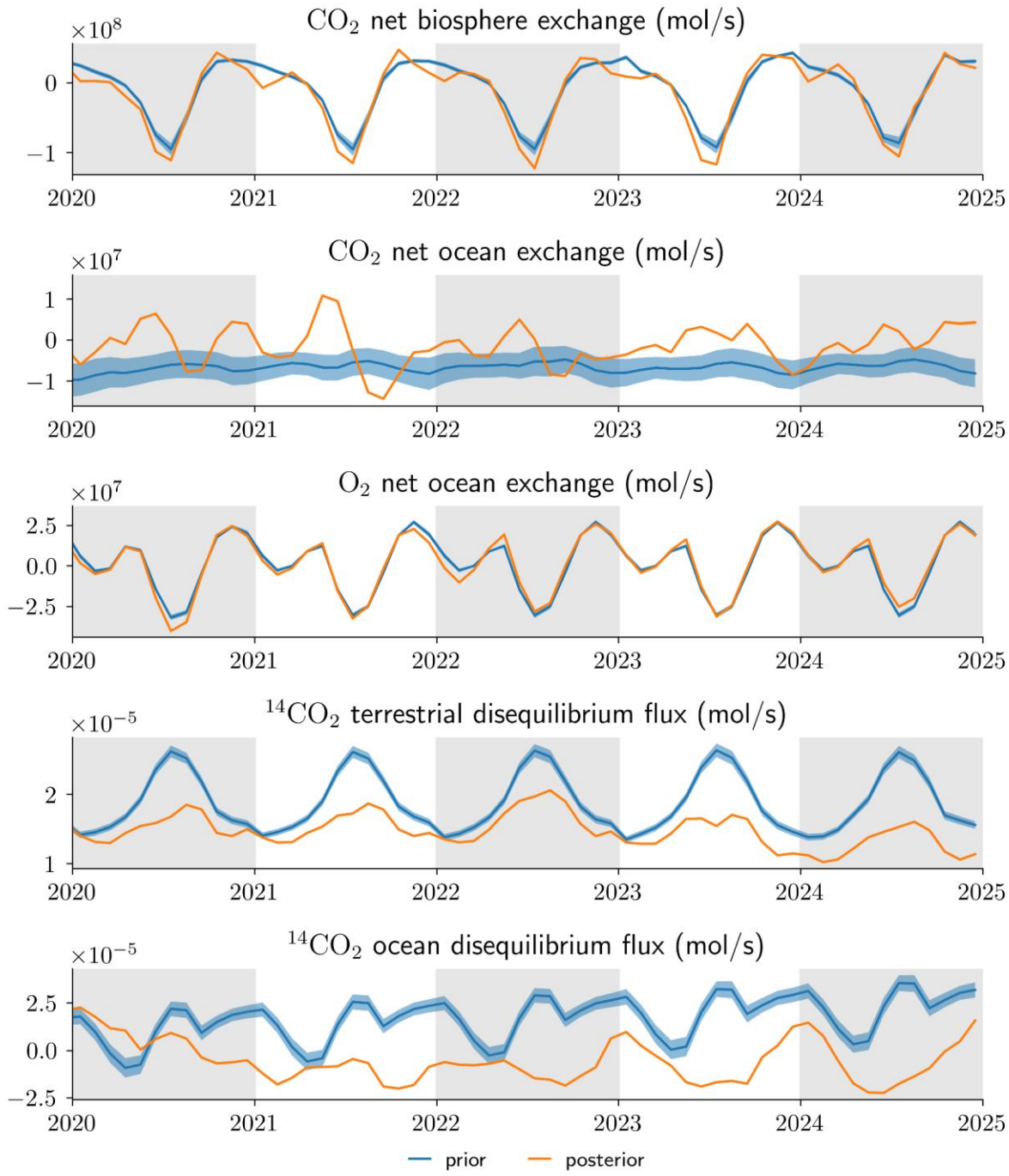

Figure 14: Prior (blue) and posterior (orange) fluxes from the global CTE Long Window joint inversion assimilating atmospheric CO_2, $\Delta^{14}CO_2$ and $\delta O_2/N_2$ observations. The blue shaded area shows the global aggregated prior uncertainty assumed in the prior.

Figure 15 zooms into the last 5 years of the global Long Window inversion. Here, we had less observations available from the global network. It is important to have a good availability of global stations, to perform global inversions, but also to get good constraints for Europe it is necessary to have a good background.

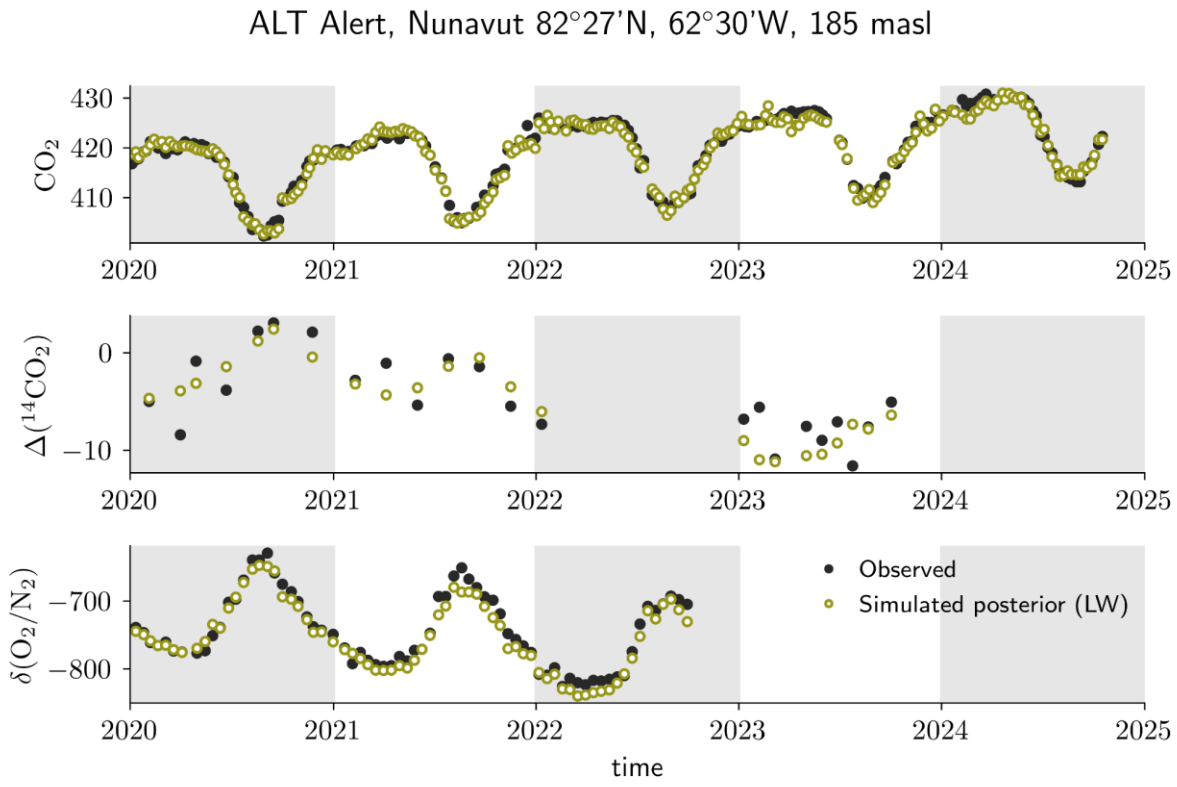

Figure 15: Simulated atmospheric CO_2 (top), $\Delta^{14}CO_2$ (middle) and $\delta O_2/N_2$ (bottom) at Alert. For the period 2020–2025 using the CTE Long Window system.

Next, we zoom in on Europe for the year 2024, in which we had the additional observations thanks to CORSO. For this, we use the CTE Short Window system that starts off from the posterior of the Long Window system. We see a good match to observations in Europe, e.g. at Cabauw as shown in Figure 16, already in the LW posterior, which is the prior for the SW inversion (except for the biosphere net exchange fluxes). The figure shows that there are certain observations that have relatively low $\Delta^{14}CO_2$ and $\delta O_2/N_2$ values, which are likely local signals, influenced by fossil fuel emissions. These local signals are not always well captured by our system, mostly due to the coarse spatial resolution (3x2 degrees lat-lon), also in the vertical direction. This is a topic for follow up research. Overall, this is a good starting point for the SW inversion. We have performed different experiments in which we have reduced the prior fossil fuel emissions, to see if the inversion can retrieve the input GridFED emissions.

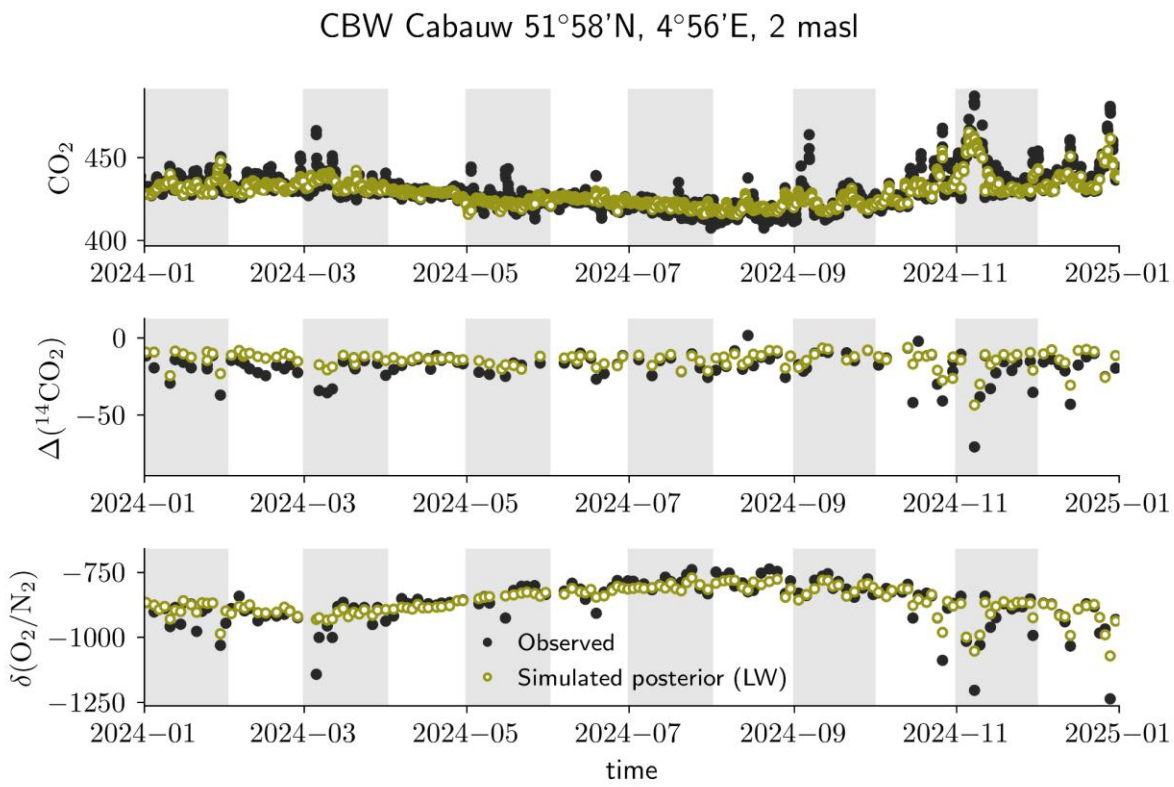

Figure 16: Simulated atmospheric CO_2 (top), $\Delta^{14}CO_2$ (middle) and $\delta O_2/N_2$ (bottom) at Cabauw for the period 2024–2025 from CTE-LW-SW. The observations were part of the intense CORSO sampling campaign. Note that both radiocarbon and oxygen show local signals in months 1-3 and 10-12 which may be related to fossil fuel signals. However these are not as strong in the simulations which is likely related to the coarse model resolution.

In our CTE-SW experiments, we have tested the influence of the assimilation of the different tracers. In Figure 17 we show the estimated emissions for Germany from these experiments. The experiment in which we assimilate all tracers (CO_2, $\Delta^{14}CO_2$ and $\delta O_2/N_2$) matches the GridFED emissions closely in the first months of 2024, but gives a higher value of the emissions in the September-December period. For this inversion, we also match the observations best (see Figure 18). This pattern of larger emissions in Sept-Dec is similar for the $\Delta^{14}CO_2$-only inversion. However for that inversion, the simulations of CO_2 and $\delta O_2/N_2$ show a larger deviation in comparison to the observations.

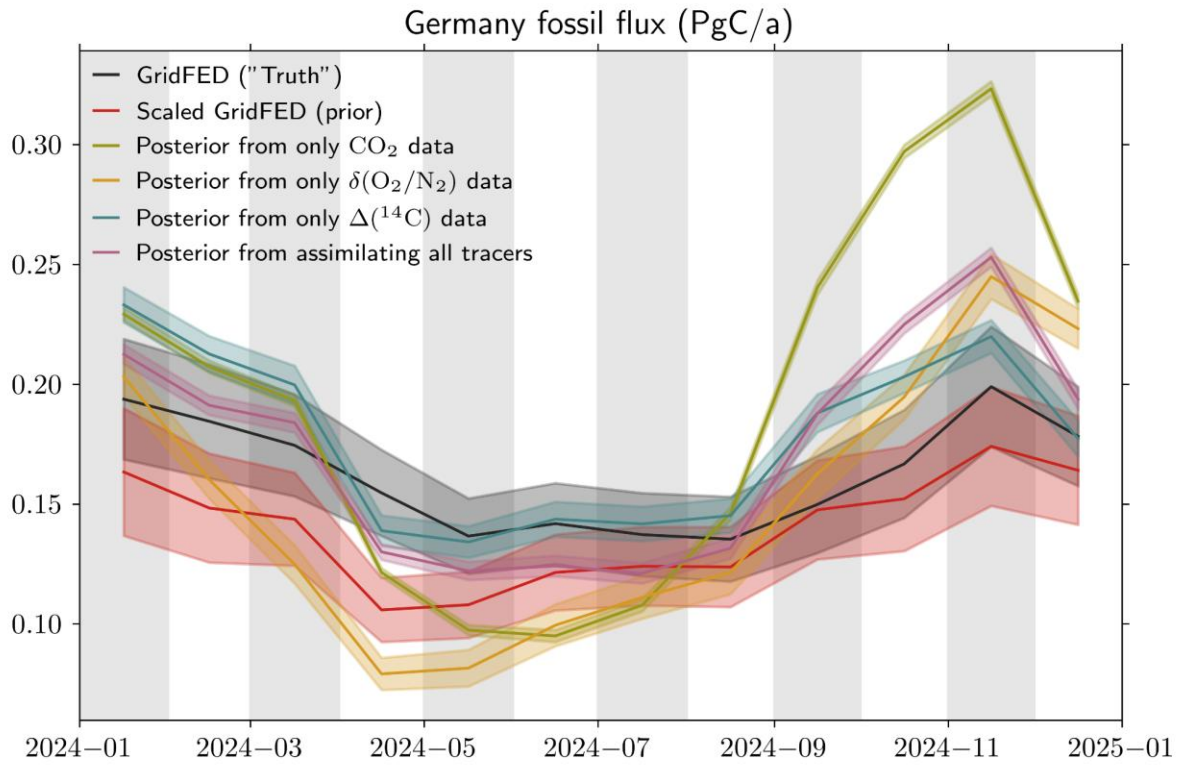

Figure 17: Fossil fuel estimate for Germany from inversions using different sets of observations. The red line shows the reduced fossil fuel emissions that were used as the prior in these experiments. The black line represents the GridFED emissions. Note that the posterior uncertainty is likely to be underestimated.

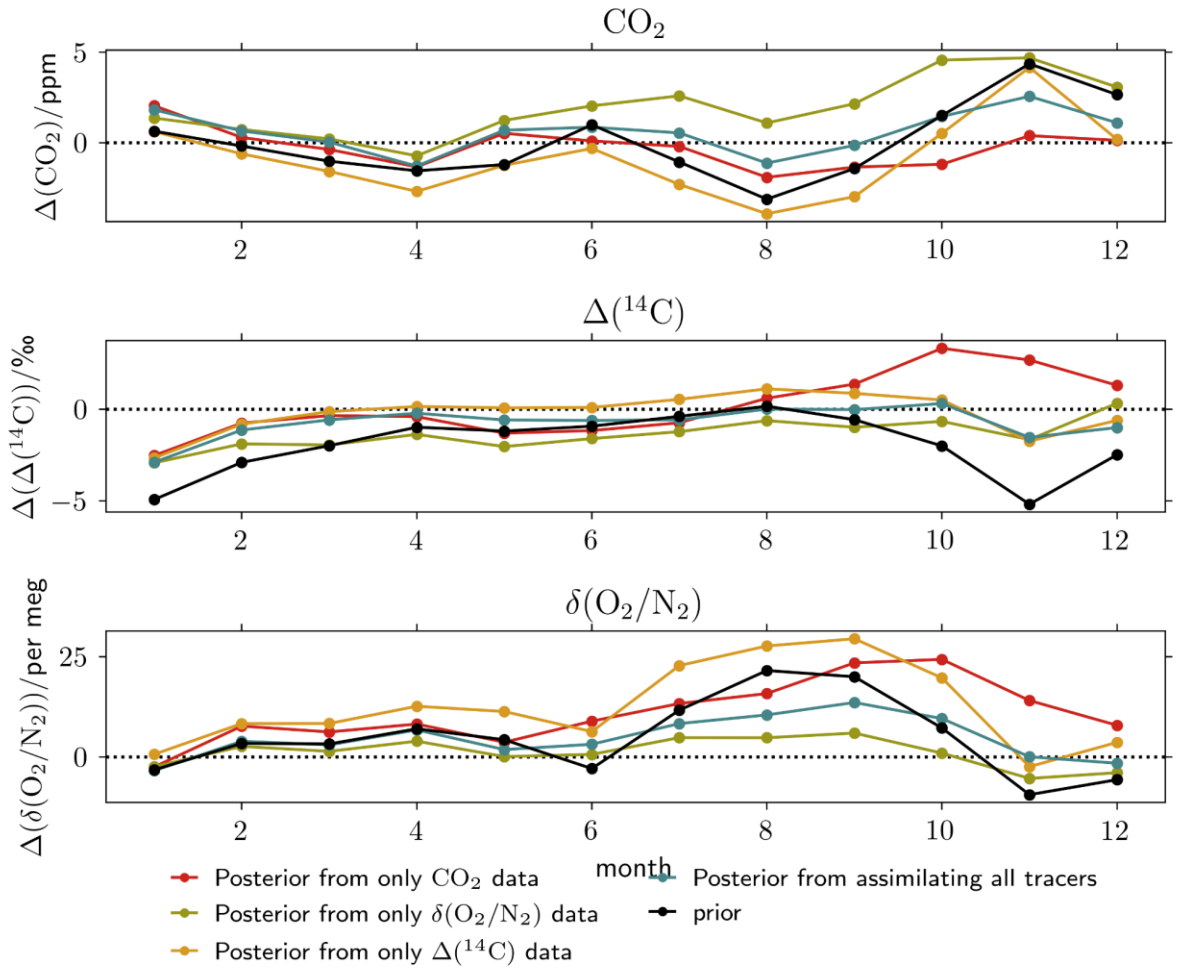

Figure 18: Monthly mean bias of observations at a selected set of sites over central and north-west Europe. Sitecodes of the selected sites are as follows: 'cbw', 'trn', 'oxk', 'ste', 'hfd', 'ope', 'wao', 'gat', 'sac', 'lin'. For $\Delta^{14}CO_2$ and $\delta O_2/N_2$ the CORSO flask measurements were used; for CO_2 the in situ ICOS data were used. For fair comparison, the same data is selected for each of the simulations.

Figure 19 shows that the main uncertainty reduction in our inversions is found in North-West Europe, this is especially visible for panels with the $\Delta^{14}CO_2$-only inversion, but also in the $\delta O_2/N_2$-only inversion. It shows that the current network mainly allows fossil fuel estimates for a relatively small part of Europe, specifically Germany, the Benelux and part of the UK, and that in order to estimate national scale emissions, the network should be expanded spatially. Note that the large uncertainty reduction shown for CO_2 is related to larger spatial coverage and volume of data. Figure 17 already showed that CO_2 by itself provides a poor constraint on the fossil fluxes.

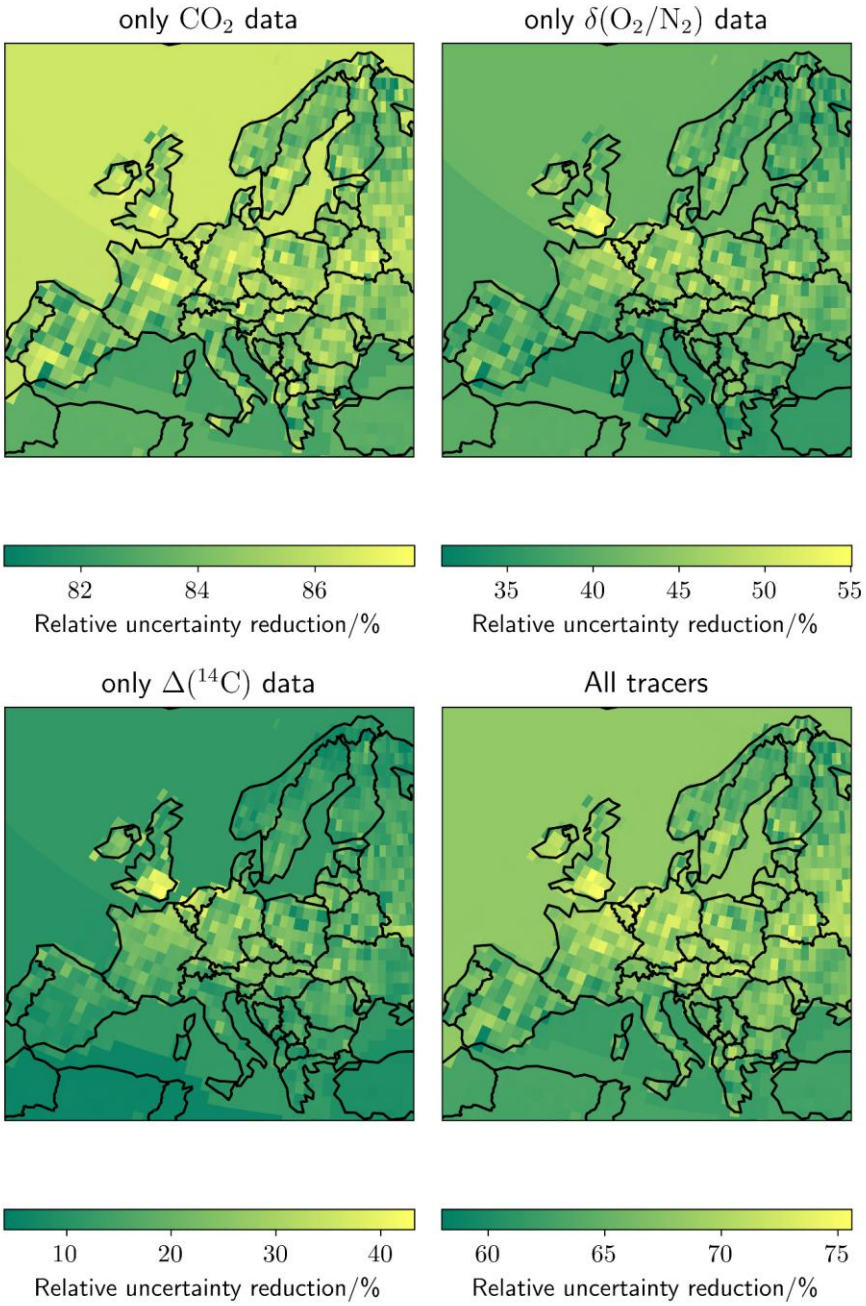

Figure 19: Maps of relative uncertainty reduction of the fossil fuel estimates after assimilating observations of CO_2, $\Delta^{14}CO_2$,$\delta O_2/N_2$ or all three tracers combined for the CTE-LW-SW system. Note that the values in the figure should be interpreted relatively within each panel, and the numbers cannot be compared between the panels. This is because spurious correlations tend to overestimate the uncertainty reduction in Ensemble Kalman Filters, and hence this figure shows a qualitative picture of the spatial pattern to gain understanding in where the tracers add additional information.

Figure 20 shows the correlations in the Net Ecosystem Exchange (NEE) and the fossil fuel flux estimates from the posterior ensemble. The low correlation in the $\Delta^{14}CO_2$-only inversion shows that this tracer informs on fossil fuel fluxes only, whereas the $\delta O_2/N_2$ and CO_2-only inversions show that these tracers also inform about the natural processes.

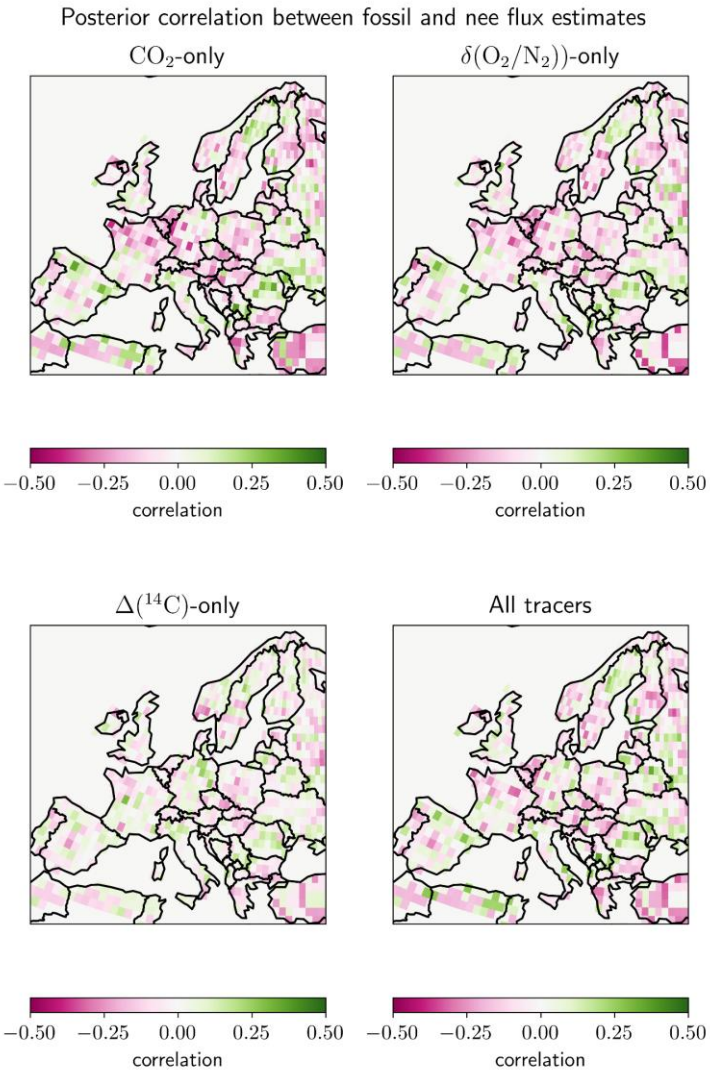

Figure 20: Correlation between posterior fossil fuel flux and Net Ecosystem Exchange (NEE) flux estimate for the CTE-LW-SW system for the inversions assimilation either CO_2, $\Delta^{14}CO_2$, or $\delta O_2/N_2$, or all three tracers combined.

4.2 European scale inversions

In this section, we present model comparisons with ICOS atmospheric $\Delta^{14}CO_2$ and O_2 observations based on the regional NAME-RHIME and LUMIA systems, and fluxes using these inverse modelling frameworks.

4.2.1 Inversions using NAME-RHIME

Forward simulations of $ffCO_2$+β (see Section 3.3) using NAME are shown in Figure 21 using the EDGAR and LPJ fluxes (blue) and using NAME-RHIME posterior fluxes (yellow). The figure indicates posterior correlations (*R*) between the observations and the model on the order of 0.7-0.8 at the two sites.

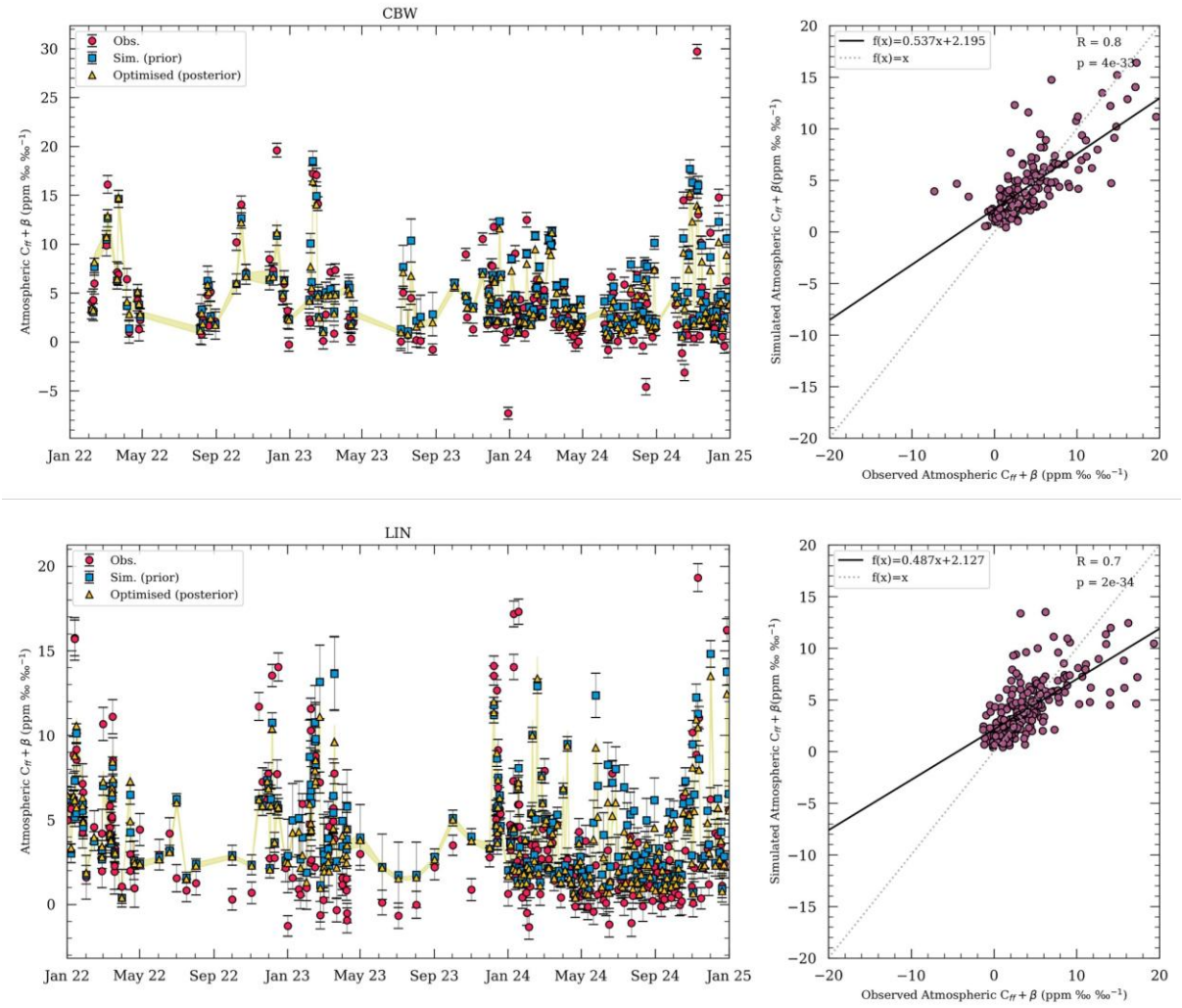

Figure 21: Above-baseline "uncorrected" fossil fuel CO_2 contributions (C_{ff}+β) derived from concurrent atmospheric $\Delta^{14}CO_2$-CO_2 observations (red circles), NAME simulations using EDGAR and VPRM (blue squares) and NAME-RHIME inversion results (yellow triangles) for Cabauw, NL and Lindenberg, DE (2022 - 2024, inclusive). The figures on the right show the observed ffCO_2+β compared to the posterior simulation at the two sites.

NAME-RHIME: Emissions estimates for Germany

Figure 22 shows emissions derived for Germany using the default inversion setup for NAME-RHIME (15% prior uncertainty per spatial basis function, 4-monthly inversions using ICOS flask data). A priori fluxes were taken from EDGAR and VPRM. Posterior emissions estimates are generally consistent with EDGAR during 2022 - 2024, with larger deviations during 2024 than 2022 - 2023, and statistically lower emissions than EDGAR during the summer of 2024 (May - August 2024).

Additional inversions were performed to indicate the level to which these inversions were influenced by the prior emissions and the sampling density.

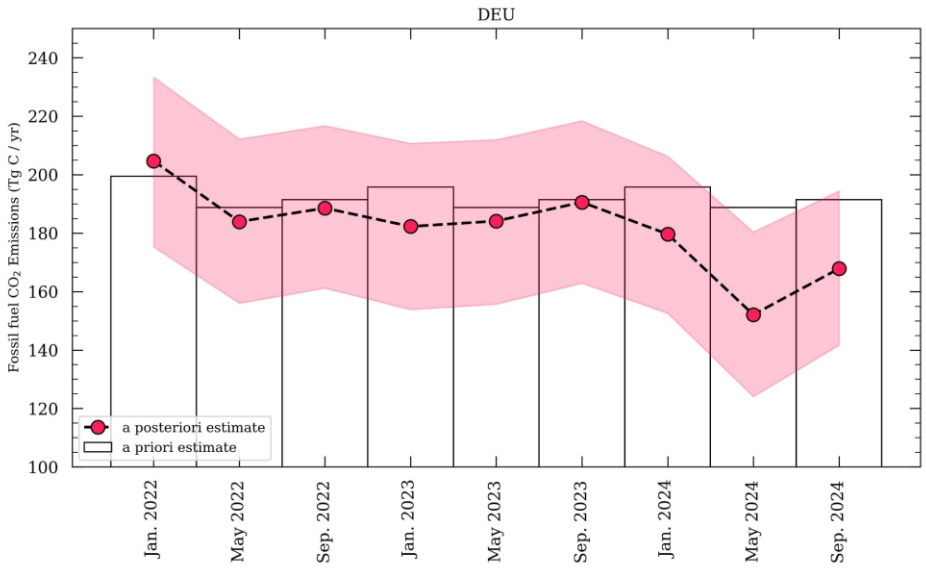

Figure 22: fossil fuel CO_2 emissions estimates for Germany from EDGAR (bars) and the NAME-RHIME base inversion (red circles with shading indicating 68% confidence interval). Results are presented for 4-month periods beginning at the dates indicated on the x-axis from 2022 to 2024.

NAME-RHIME: Influence of prior fossil fuel flux magnitude

NAME-RHIME inversions were performed using perturbed prior flux magnitudes, to determine the level to which inversion results were influenced by the prior. Figure 23 shows the results of two experiments, the first using EDGAR in the prior, and the second with EDGAR increased by 20%. Compared to the NAME-RHIME "base" run, prior uncertainty was increased to by 100% to give the inversion the flexibility to sufficiently adjust the prior.

As shown in Figure 23, the two inversions show more consistent fossil fuel emissions estimates during 2024, when sampling frequency was increased.

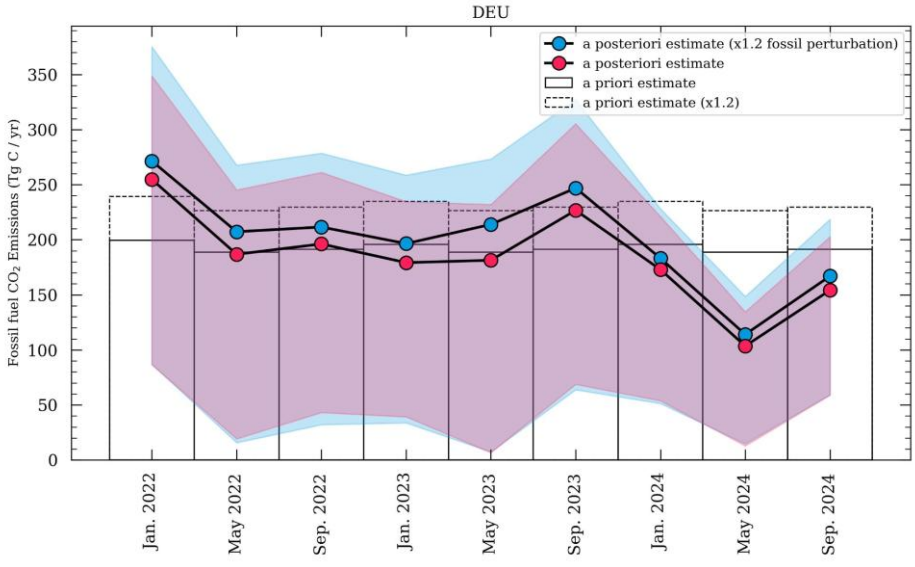

Figure 23: NAME-RHIME flux estimates for Germany using two different prior fossil fuel emissions magnitudes. Bars with solid lines show the EDGAR prior, with corresponding optimised fluxes shown as red circles. Bars with dashed lines show EDGAR emissions increased by 20%, with the corresponding inversion results in blue. Flux estimates were for 4-month periods between 2022 and 2024 (labels show the beginning of each period). Compared to the "base" NAME-RHIME inversion

shown in the other sections, prior uncertainty was increased by 100%, to allow the inversion to adjust from the “biased” prior.

NAME-RHIME: Influence of sampling frequency

A NAME-RHIME inversion was run using the same parameters as the “base” run, but in which the 2024 sampling frequency was reduced to the same frequency as in 2022 and 2023. Figure 24 shows that, in this simulation, the inversions with lower sampling frequency were closer to the prior estimates than those with the full dataset. Combined with the results from Figure 23, this finding indicates that emissions estimates before 2024 are more strongly influenced by the prior than those in 2024.

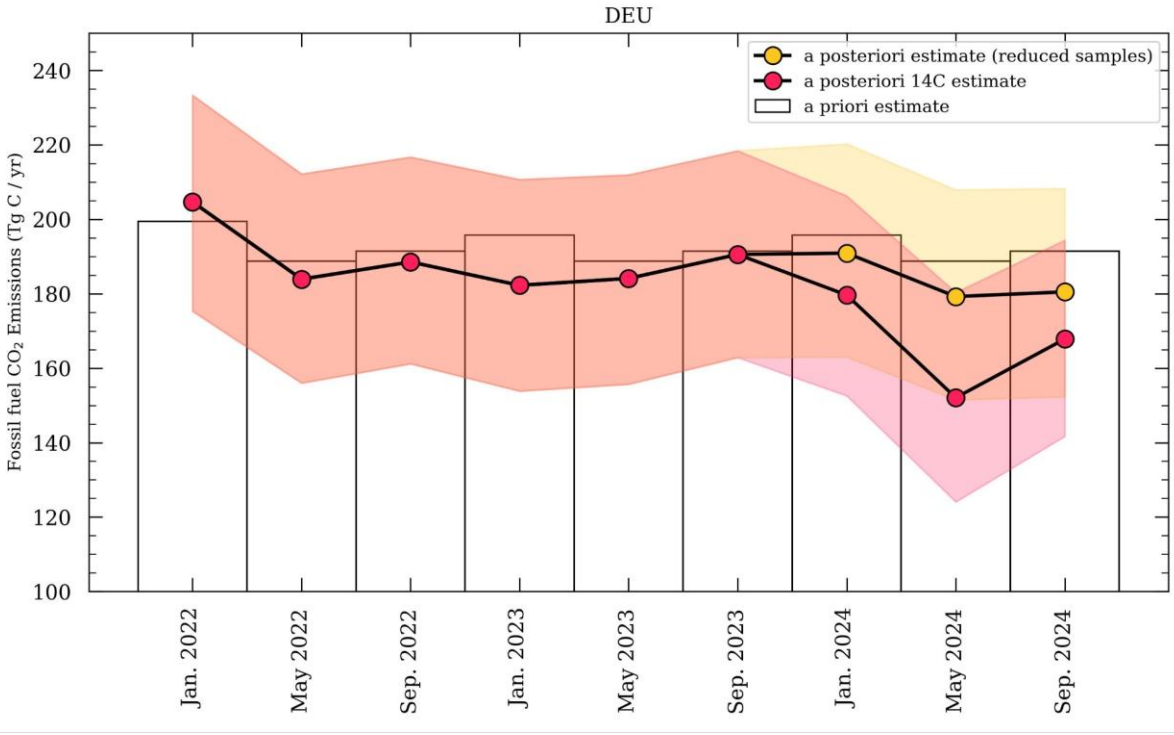

Figure 24: NAME-RHIME fossil fuel flux estimates for Germany with a reduced sampling frequency in 2024 (yellow circles). The NAME-RHIME inversion using the full dataset is shown in red.

NAME-RHIME: Influence of atmospheric background $\Delta^{14}CO_2$

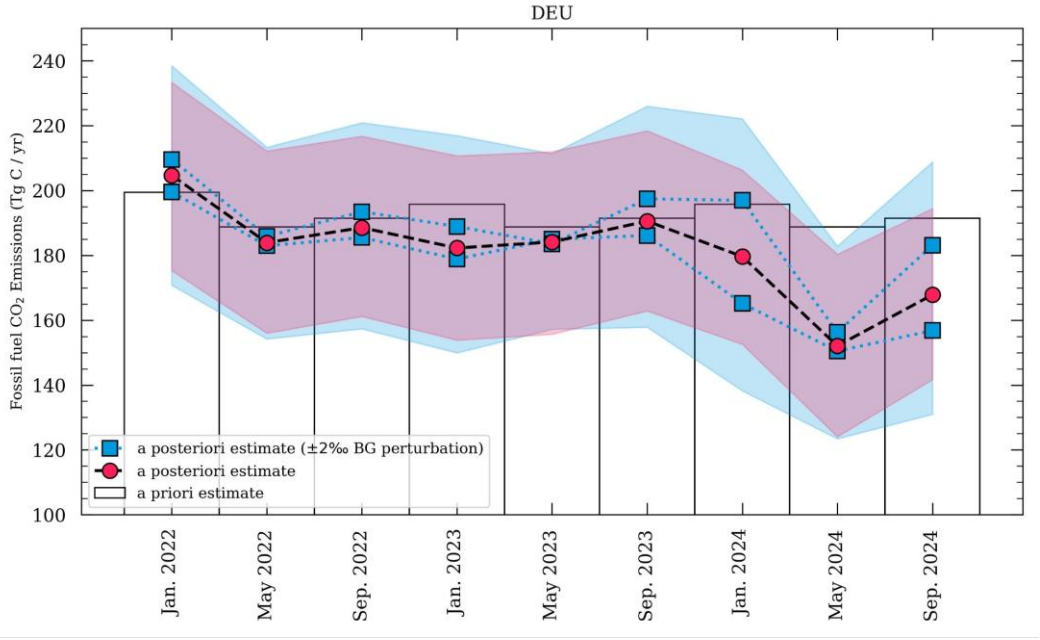

Figure 25: NAME-RHIME fossil fuel flux estimates for Germany with ±2‰ perturbed background $\Delta^{14}CO_2$ values (blue) and the standard inversion result (red).

We explored the impact of perturbing the background $\Delta^{14}CO_2$ estimate on the fossil fuel emissions inferred by RHIME. A perturbation of ±2‰ was applied to the background and yielded fossil fuel emissions estimates very similar to the unperturbed inversion result (Figure 25). A median difference of 4.9 Tg C yr^{-1} (2.7%) from the main posterior estimate was found with largest deviations of up to 17 Tg C yr^{-1} found in 2024. These differences are smaller than the posterior-prior difference for the main posterior emissions estimate.

Figure 25 shows there are overlapping 68% confidence intervals between the main fossil fuel emissions inferred from RHIME and the background-perturbed estimates. This result seems to suggest background $\Delta^{14}CO_2$ perturbations of ±2‰ do not yield statistically significantly different results from the main posterior emissions estimate. This was quantified by conducting Student t-test analyses for each sensitivity test. The results from these tests yielded *p*-values of 0.42 between the fossil perturbed results in Figure 23; 0.32 for the reduced data sampling results in Figure 24; 0.34 for the background perturbed results in Figure 35. In each case the *p*-value denotes the results were not statistically significantly different from the main inversion result. However, it is noteworthy that the highest sensitivity to boundary conditions is observed during 2024, when the density of observations is highest (as previously shown, before this period, the inversion is more prior-dominated). Notwithstanding this finding, the sensitivity to the boundary conditions during the summer of 2024 was small, suggesting that the drop in emissions observed during the summer is not due to uncertainties in the baseline.

4.2.2 CO_2-$\Delta^{14}CO_2$ inversions with LUMIA

Across both Cabauw (NL) and Lindenberg (DE), the CO_2-only inversions produce a clear adjustment in the CO_2 posterior but almost no correction in $\Delta^{14}CO_2$, as expected. Since fossil fuel emissions are not optimised (i.e., prescribed) in the CO_2-only setup, most of the mismatch in the prior modelled atmospheric CO_2 time series, reflected in RMSE reductions from 4.28 to 2.49 ppm at Cabauw and from 11.18 to 3.98 ppm at Lindenberg, is absorbed through modifications of biospheric fluxes (Net Ecosystem Exchange) rather than through changes in atmospheric $\Delta^{14}CO_2$. This leads to minimal improvement in $\Delta^{14}CO_2$, where RMSE remains high (e.g. 3.79‰ at Cabauw and 23.72‰ at Lindenberg), consistent with the fact that nearly all of the radiocarbon signal misfit originates from fossil-fuel-driven dilution rather than biospheric processes.

In contrast, the fossil fuel inversion ($ffCO_2$) produces the opposite pattern: CO_2 adjustments are limited, but $\Delta^{14}CO_2$ shows substantial improvement because this method explicitly reconstructs fossil fuel CO_2 as a radiocarbon-free dilution term. At Cabauw, the $\Delta^{14}CO_2$ RMSE decreases from 4.2 to 1.37‰, and at Lindenberg from 18.11 to 6.97 ‰. These improvements occur despite smaller corrections in CO_2 compared to the CO_2-only case (e.g. posterior RMSE of 3.94 ppm at Cabauw and 8.39 ppm at Lindenberg), reflecting the fact that the radiocarbon constraint directly informs the $ffCO_2$ pseudo-observations while CO_2 alone cannot fully isolate the fossil fuel component.

The dual-tracer inversion integrates both CO_2 and $\Delta^{14}CO_2$ constraints, producing consistent corrections in both tracers. For Cabauw, CO_2 RMSE decreases from 4.28 to 2.73 ppm and $\Delta^{14}CO_2$ RMSE from 4.2 to 2.05‰, while at Lindenberg reductions are from 11.18 to 3.06 ppm and 18.11 to 1.83‰. This joint improvement reflects the ability of the dual-tracer framework to redistribute adjustments between fossil fuel and biospheric fluxes while simultaneously resolving the radiocarbon dilution signal. The dual-tracer posterior also reproduces the seasonal behaviour of both tracers more accurately than the single-tracer setups, reducing wintertime biases driven by fossil-fuel dilution (particularly pronounced at Lindenberg) while capturing the magnitude and timing of the CO_2 summer minimum. This balanced performance highlights the complementarity of the two tracers: CO_2 primarily constrains biospheric variability, $\Delta^{14}CO_2$ isolates fossil fuel emissions, and only their combined assimilation yields consistent corrections in both atmospheric signals.

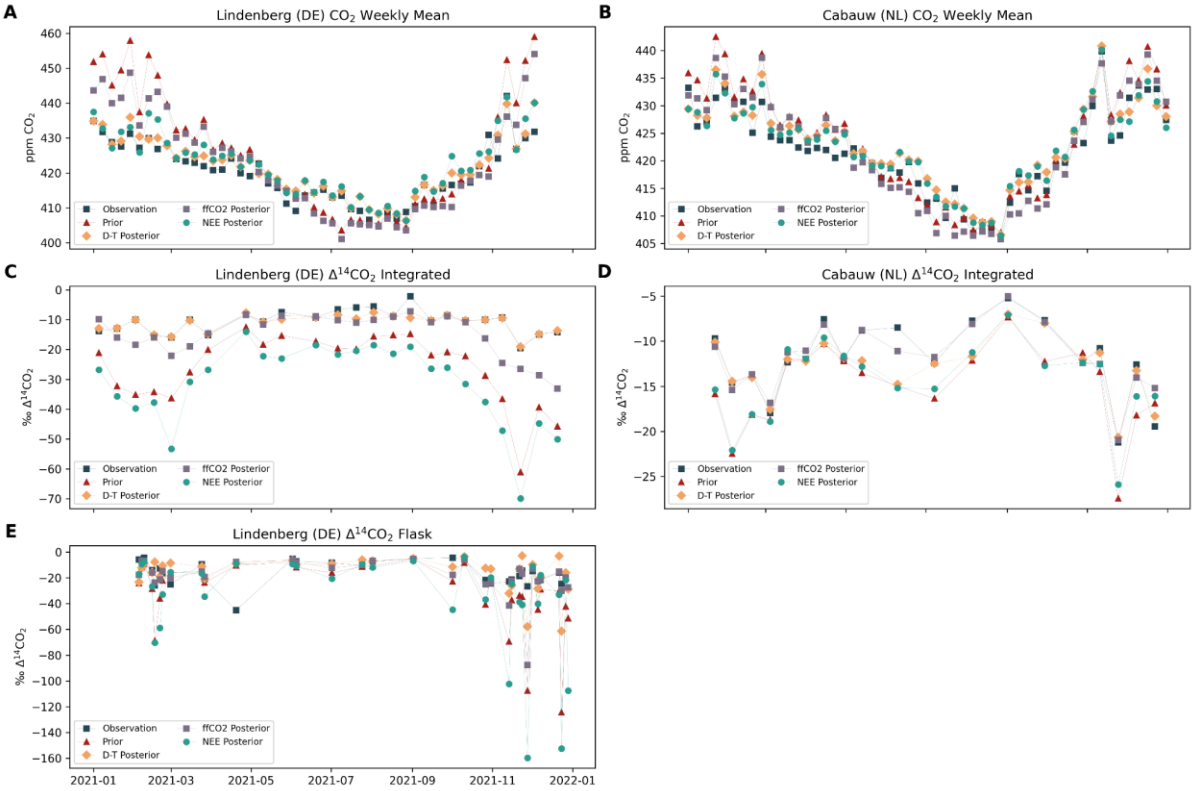

Figure 26: Comparison of observed and posterior CO_2 and $\Delta^{14}CO_2$ time series at Lindenberg (DE) (left) and Cabauw (NL) (right) for 2021. Panels (A-B) show weekly mean CO_2, panels (C-D) show two-week integrated $\Delta^{14}CO_2$, and panel (E) show flask $\Delta^{14}CO_2$ measurements at LIN (no flask measurements were available for CBW during this year). For each site, prior modelled concentrations and posterior results from the CO_2-only, $ffCO_2$, and dual-tracer inversions are shown together with their respective RMSE values.

Figure 27 shows the monthly and annual fossil fuel CO_2 emissions estimated for the EU27 region in 2021 using the dual-tracer inversion, the fossil fuel inversion, and three different prior inventories (CTE-HR, EDGAR-BP, and ODIAC). The priors show similar seasonal patterns, with higher emissions in winter and lower emissions in summer, but their magnitudes differ substantially. CTE-HR produces the largest seasonal cycle, while ODIAC is much flatter. Both inversion approaches reduce these differences, indicating that the priors tend to overestimate the seasonal variability of fossil fuel emissions, particularly during the winter heating period.

Across all three priors, the posterior estimates are generally lower than the prior values throughout the year. The largest reductions occur during the winter months, for example January and February, where EDGAR-BP drops from values above 3 Tg C day^{-1} to roughly 2.2-2.4 Tg C day^{-1} after inversion. Summer reductions are smaller but remain consistent across priors. The fossil fuel inversion usually produces slightly lower monthly values than the dual-tracer system, reflecting the stronger constraint from $\Delta^{14}CO_2$ when fossil fuel emissions are isolated directly. A quantitative comparison confirms that the differences between the prior and posterior estimates, although systematic, are not statistically significant when evaluated against their respective uncertainties. Monthly prior–posterior differences for the dual-tracer system range from 0.07 to 0.48 Tg C day^{-1}, while the combined 1σ uncertainties span 1.40-2.01 Tg C day^{-1}, yielding $|Z| < 0.25$ for all months. For the $ffCO_2$-only inversion, differences range from 0.16 to 0.67 with combined uncertainties of 1.34-1.96 Tg C day^{-1}, resulting in $|Z| < 0.35$. This indicates that the inversions consistently reduce the magnitude of fossil fuel emissions relative to the priors, but these adjustments remain well within the combined uncertainty envelopes.

Panel (b) of Figure 27 shows the annual totals. The priors spread widely, from about 680 to 840 Tg C yr^{-1}. After applying the atmospheric constraints, this range becomes much narrower. The dual-tracer inversion gives annual values between about 660 and 740 Tg C yr^{-1}. The fossil fuel inversion produces a slightly narrower interval, around 660 to 710 Tg C yr^{-1}. The posterior values of the dual-tracer inversions using CTE-HR and EDGAR are close to the EEA emission inventory (about 720 Tg C yr^{-1}). This agreement indicates that the dual-tracer system can help reconcile differences between top-down and bottom-up approaches, even when the prior inventories differ substantially. The uncertainty bars also show that the dual-tracer and isotope budget estimates remain consistent within one standard deviation for most cases.

Overall, the figure highlights three consistent findings: the inversions lower the annual fossil fuel CO_2 emissions compared to the priors, the priors show stronger seasonality than supported by the observational constraints, and the dual-tracer and isotope budget approaches give broadly similar results even though they rely on different information.

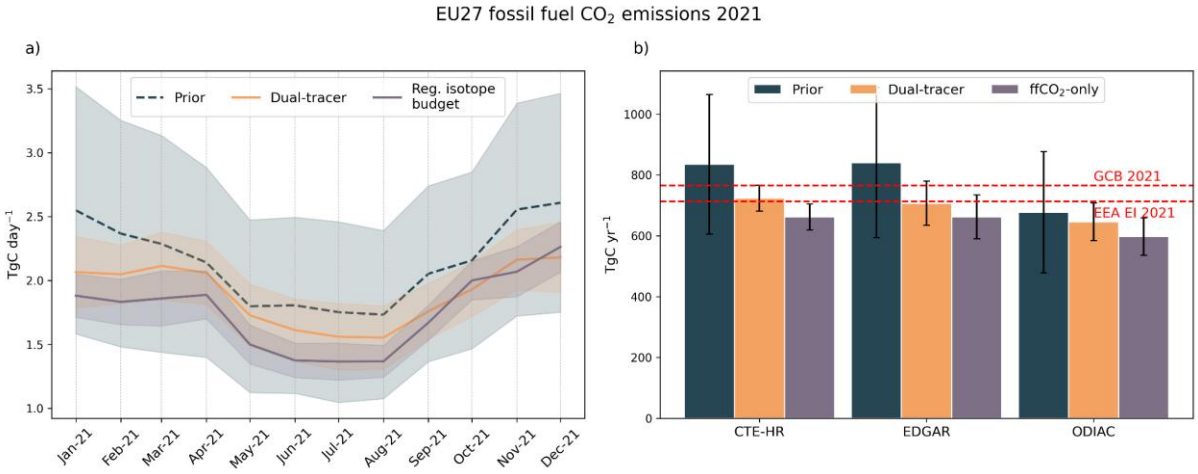

Figure 27. EU27 fossil fuel CO_2 emissions for 2021 inferred from the dual-tracer inversion and the fossil fuel inversion approach, compared with three prior emission inventories (CTE-HR, EDGAR-BP, and ODIAC). (a) Monthly mean fossil fuel CO_2 fluxes (Tg C day^{-1}). Each line represents the mean of the three priors or posteriors. Shaded areas denote 1σ uncertainties for each estimate. (b) Annual fossil fuel CO_2 totals (Tg C yr^{-1}) for each prior and posterior system. Error bars show 1σ uncertainties. Independent benchmarks from the *Global Carbon Budget 2021 (GCB 2021) and the European Environment Agency emission inventory (EEA EI 2021) are shown as red dashed lines.*

Figure 28 shows the monthly and annual net ecosystem exchange (NEE) for the study domain in 2021. As seen in panel (a), all priors and posteriors capture the expected seasonal pattern with strong uptake during late spring and summer and net release during winter. However, the magnitude of the prior uptake is larger than the posterior results. Both inversion approaches reduce the amplitude of the seasonal cycle, especially during the peak growing season in May-July, bringing the NEE closer to -10 Tg C day^{-1} rather than the prior values that exceed -20 Tg C day^{-1} for some inventories.

The CO_2-only and dual-tracer inversions produce similar monthly profiles, although the CO_2-only setup yields slightly stronger summer uptake for all priors. A statistical comparison confirms that these differences are not significant relative to their uncertainties: monthly prior–posterior differences for the dual-tracer inversion range from -2.20 to 2.02 Tg C day^{-1}, while the combined 1σ uncertainties span 12.25-27.12 Tg C day^{-1}, yielding $|Z| < 0.16$ for all months. For the CO_2-only inversion, differences range from −1.91 to 2.81 with combined uncertainties of 12.59-28.51 Tg C day^{-1} and $|Z| < 0.21$. These results indicate that although the inversions reduce the magnitude of the seasonal cycle, the adjustments remain well within the uncertainty envelopes and are therefore not statistically significant. The similarity between the two

approaches reflects the limited influence of $\Delta^{14}CO_2$ on NEE when fossil fuel corrections dominate the $\Delta^{14}CO_2$ signal, as shown in Figure 26.

Panel (b) summarizes the annual NEE for each prior and posterior. The priors span a wide range, from about -190 to -260 Tg C yr^{-1}, while the posteriors cluster more tightly around -200 Tg C yr^{-1}. The CO_2-only approach generally produces slightly larger uptake than the dual-tracer inversion, in line with the modest effect of $\Delta^{14}CO_2$ on biospheric fluxes at this scale. Uncertainties remain large for all cases, showing that NEE is less well constrained than fossil fuel emissions.

Together with the fossil-fuel results, these NEE estimates show how the dual-tracer inversion separates the contributions of fossil fuel emissions and biospheric fluxes: fossil fuel emissions are strongly adjusted by $\Delta^{14}CO_2$, whereas NEE is shaped primarily by CO_2 observations. The combined results indicate that the prior emission inventories tend to overestimate both fossil fuel emissions and biospheric uptake.

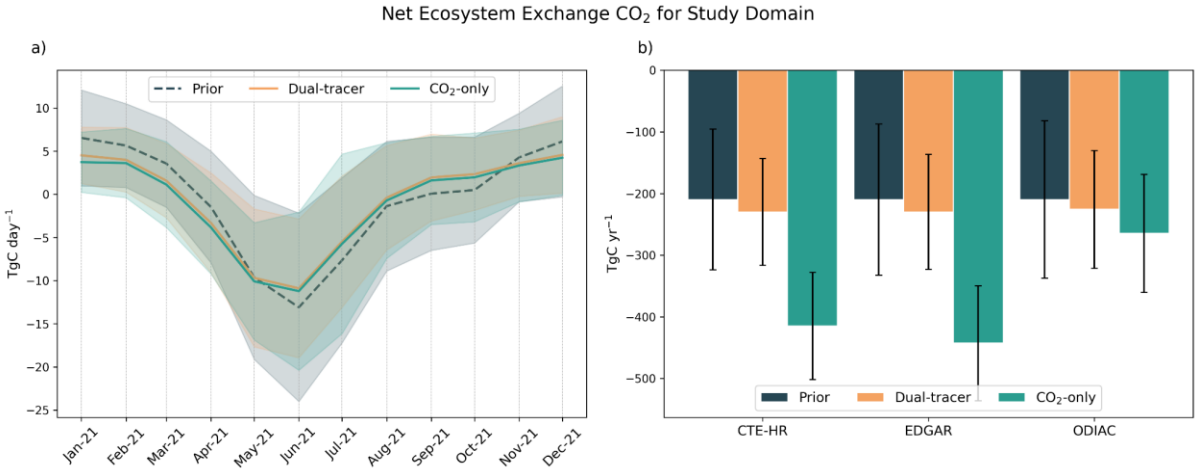

Figure 28. Net ecosystem exchange (NEE) for the study domain in 2021 from prior estimates and the CO_2-only and dual-tracer inversions. (a) Monthly NEE (Tg C day^{-1}) for the three prior products (CTE-HR, EDGAR-BP, ODIAC) and their corresponding posterior estimates. Shaded areas represent ±1σ uncertainties. (b) Annual NEE (Tg C yr^{-1}) corresponding to each prior and posterior. Error bars show ±1σ uncertainties.

Figure 29 shows the monthly EU27 fossil fuel CO_2 emissions from 2015 to 2024 obtained with the fossil fuel inversion inversion. The prior emissions (dashed line) show a very regular seasonal cycle, with high winter values (often above 3 Tg C day^{-1}) and a repeated summer minimum around or below 2 Tg C day^{-1}. The posterior emissions (solid line) follow the same seasonal pattern but with a systematically reduced amplitude. Winter peaks are lower and summer minima are slightly higher than in the prior, which is consistent with the 2021 analysis where the isotope budget reduced the seasonal range of EU27 fossil fuel emissions. The shaded areas indicate that posterior uncertainties are smaller than prior uncertainties for most of the period, especially after 2017.

Over the full decade, the inversion tends to pull emissions downward relative to the prior, particularly during winter. This is most evident from 2018 onward, where posterior winter peaks rarely exceed 3 Tg C day^{-1}, while the prior often approaches or exceeds 3.5 Tg C day^{-1}. A statistical comparison over the full 2015–2024 period shows that these adjustments remain modest relative to their uncertainties: monthly prior–posterior differences range from −0.45 to 1.41 Tg C day^{-1}, while the combined 1σ uncertainties span 0.83-5.27 Tg C day^{-1}, yielding $|Z| < 0.6$ with a mean of about 0.2. Thus, although the inversion consistently shifts the prior toward lower winter emissions and slightly higher summer values, these changes remain within the uncertainty envelopes and are not statistically significant.

The year 2020 shows a noticeable reduction in emissions during spring and early summer. Although the CTE-HR prior already includes adjustments related to COVID-19 restrictions, the posterior still reflects this anomaly, indicating that the isotope budget remains sensitive to large, short-term changes in fossil fuel use. After 2020, emissions recover, but the posterior remains consistently below the prior during most winters, indicating that the top-down constraint continues to moderate the amplitude of the seasonal cycle.

The behaviour in 2023 is different from the surrounding years and is flagged in the figure as needing further investigation. During this year, the posterior shows unusually low values in late winter and early spring, well below the prior and also below the typical levels seen in 2018-2022. Given the absence of an obvious large-scale driver comparable to the 2020 lockdowns, this feature may reflect a combination of changes in observational coverage, transport representation, or prior errors, and should be examined more carefully in future work.

The evolution of the radiocarbon sampling network provides context for the behaviour of the posterior estimates over the 10-year period. The number of $\Delta^{14}CO_2$ samples increases from 27 in 2015 to nearly 1500 in 2024. In the first years, when fewer than about 200 samples were available annually, the posterior remains generally close to the prior, although some differences already appear in 2016 and 2017. From 2018 onward, with more than 250–300 samples per year, the posterior displays more frequent deviations from the prior, including the reduction visible around 2020. By 2024, the substantially higher number of observations coincides with narrower posterior uncertainty bands compared with the early years. These multi-year inversion results are partially (2015-2022) also included as part of Task 2.3 of the HEU AVENGERS Project (grant agreement no. 101081322) since the development of the LUMIA radiocarbon framework was co-funded by both projects.

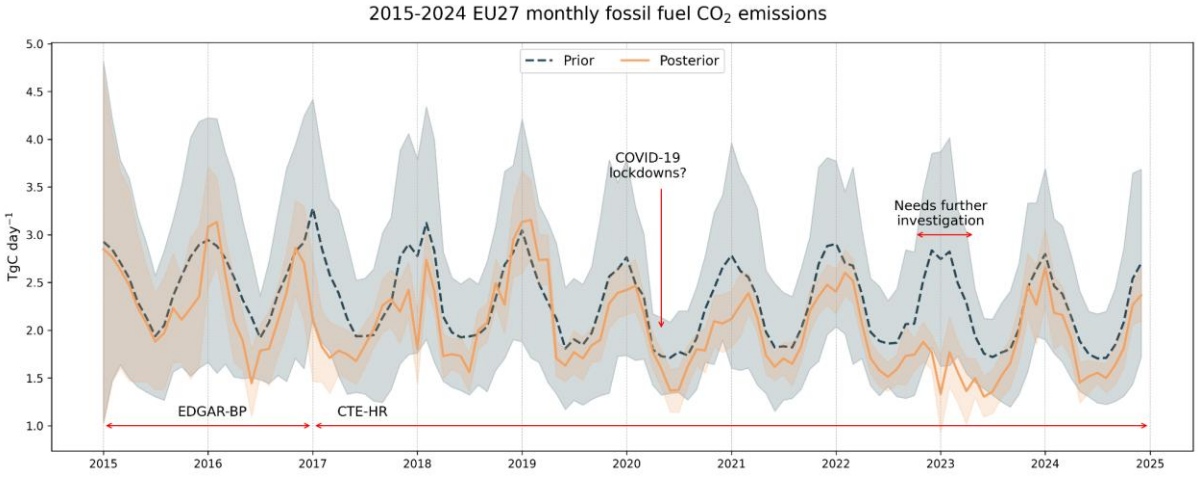

Figure 29. Monthly EU27 fossil fuel CO_2 emissions for 2015–2024 from the fossil fuel inversion. The dashed line shows the prior emissions and the solid line the posterior estimates, with shaded areas indicating ±1σ uncertainties.

Figure 30 shows the 2024 EU27 fossil fuel CO_2 emissions using the prior (CTE-HR) and two inversion configurations: AllObs, which uses all available $\Delta^{14}CO_2$ observations, and Flask-only, which uses only flask samples. As in earlier years, the prior displays a pronounced seasonal cycle with high emissions during winter and lower emissions in summer. Both inversion setups reduce this amplitude, especially between January and May, where posterior emissions remain well below the prior for all months.

The Flask inversion consistently yields the lowest monthly emissions throughout most of the year. Its spring minimum reaches values close to 1.3 Tg C day^{-1}, compared with roughly 1.5 TgC day^{-1} in the AllObs setup and around 1.7 Tg C day^{-1} in the prior. Both posterior time series also show smoother seasonal transitions compared with the prior, suggesting that the $\Delta^{14}CO_2$ constraints moderate the monthly variability. Posterior uncertainties are narrower than prior uncertainties across all months, indicating a stronger atmospheric constraint, particularly with

the Flask setup. A statistical comparison confirms that the reductions imposed by the inversions remain well within the combined posterior–prior uncertainty envelopes: for EU27, monthly prior-posterior differences range from 0.15 to 0.42 Tg C day^{-1} for the AllObs inversion and 0.23 to 0.66 Tg C day^{-1} for the Flask inversion, while the combined 1σ uncertainties span 0.65-1.59 Tg C day^{-1}, yielding |Z| < 0.9 for all months. Thus, although the posterior consistently lies below the prior, these adjustments are not statistically significant.

Panel (b) summarizes the annual totals. The prior estimate for 2024 is 793 ± 128 Tg C yr^{-1}. The AllObs inversion reduces this to 698 ± 48 Tg C yr^{-1}, while the Flask-only inversion gives an even lower value of 649 ± 39 Tg C yr^{-1}, which is the closest to the IEA/GCB 2024 reference level (approximately 660 Tg C yr^{-1}). The tighter uncertainties from both inversions reflect the large and dense $\Delta^{14}CO_2$ dataset available for 2024. The differences between AllObs and Flask indicate that flask samples alone contain sufficient information to strongly constrain annual fossil fuel emissions, with the AllObs solution landing between the prior and Flask estimates.

Panels (c–d) show the same analysis for Germany. The prior gives an annual total of 187 ± 111 Tg C yr^{-1}, well above the GCB 2024 value of 156.2 Tg C yr^{-1}. The large prior uncertainty is due to the system configuration in which the prior total uncertainty is distributed across the study domain relative to the observation network density. The inversions reduce both the magnitude and the spread. The AllObs solution yields 139 ± 31 Tg C yr^{-1}, and the Flask inversion gives 132 ± 21 Tg C yr^{-1}, both close to the GCB emission inventory and much tighter than the prior. The monthly behaviour mirrors the EU27 case: winter emissions are lowered relative to the prior, spring and summer minima converge across setups, and late-year differences remain small. The similarity between the AllObs and Flask results again shows that flask $\Delta^{14}CO_2$ measurements alone already provide a strong constraint at the national scale. A quantitative comparison again shows that the reductions relative to the prior remain well within uncertainty bounds: for Germany, monthly differences between the prior and the AllObs posterior range from 0.06 to 0.23, with combined 1σ uncertainties of roughly 0.49-1.18 (|Z| < 0.5). For the Flask posterior, differences range from 0.06 to 0.27 with uncertainties of 0.49-1.17 (|Z| < 0.6). These adjustments therefore reflect consistent downward corrections rather than statistically significant departures from the prior.

Taken together, the EU27 and Germany inversions show that the 2024 atmospheric constraints systematically adjust the prior estimates and produce annual budgets that lie closer to independently reported values such as the bottom-up estimates from the Global Carbon Budget. The reduction in uncertainty from prior to posterior is substantial for both regions, and particularly notable for Germany, where the inversion narrows the annual total to a much more stable range. The close agreement between the AllObs and Flask configurations across both spatial scales shows that flask $\Delta^{14}CO_2$ measurements already provide a solid basis for constraining fossil fuel emissions. At the same time, the differences that remain between the two setups also highlight the importance of strengthening the $\Delta^{14}CO_2$ network. Integrated samples contribute valuable temporal coverage, but they depend more strongly on atmospheric transport modeling over long periods, which can introduce additional uncertainties. Flask measurements, by contrast, offer direct and well-characterized observations that are less sensitive to these modelling issues and therefore play a key role in constraining the inversion. Increasing the number and geographic coverage of flask $\Delta^{14}CO_2$ samples would enhance the robustness of the fossil fuel signal and improve the consistency of regional and national estimates.

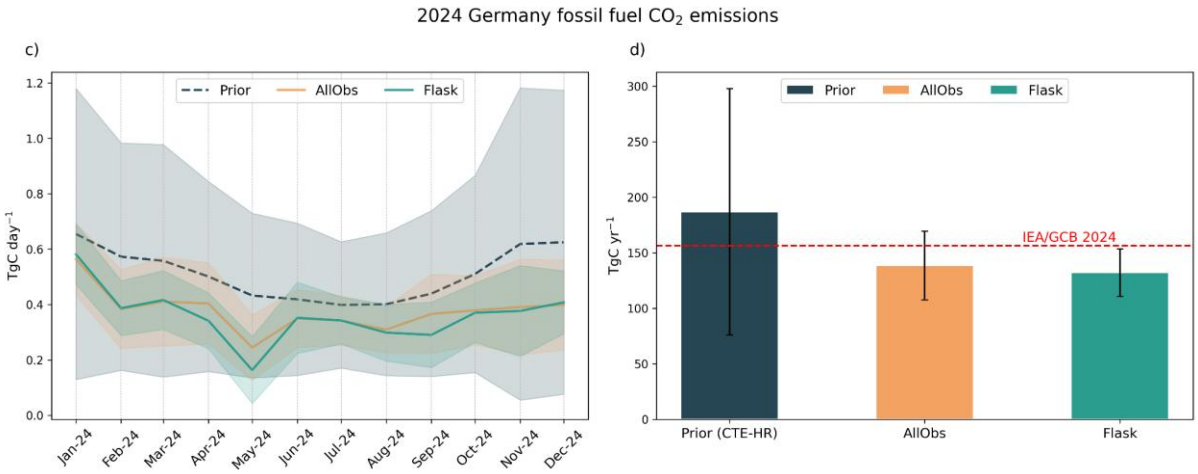

Figure 30. *EU27 and Germany fossil fuel CO_2 emissions for 2024 from the prior (CTE-HR) and two inversion configurations using the fossil fuel inversion framework: AllObs and Flask-only. (a-c) Monthly emissions (Tg C day^{-1}) with ±1σ uncertainties. (b-d) Annual totals (Tg C yr^{-1}).*

4.2.3 APO

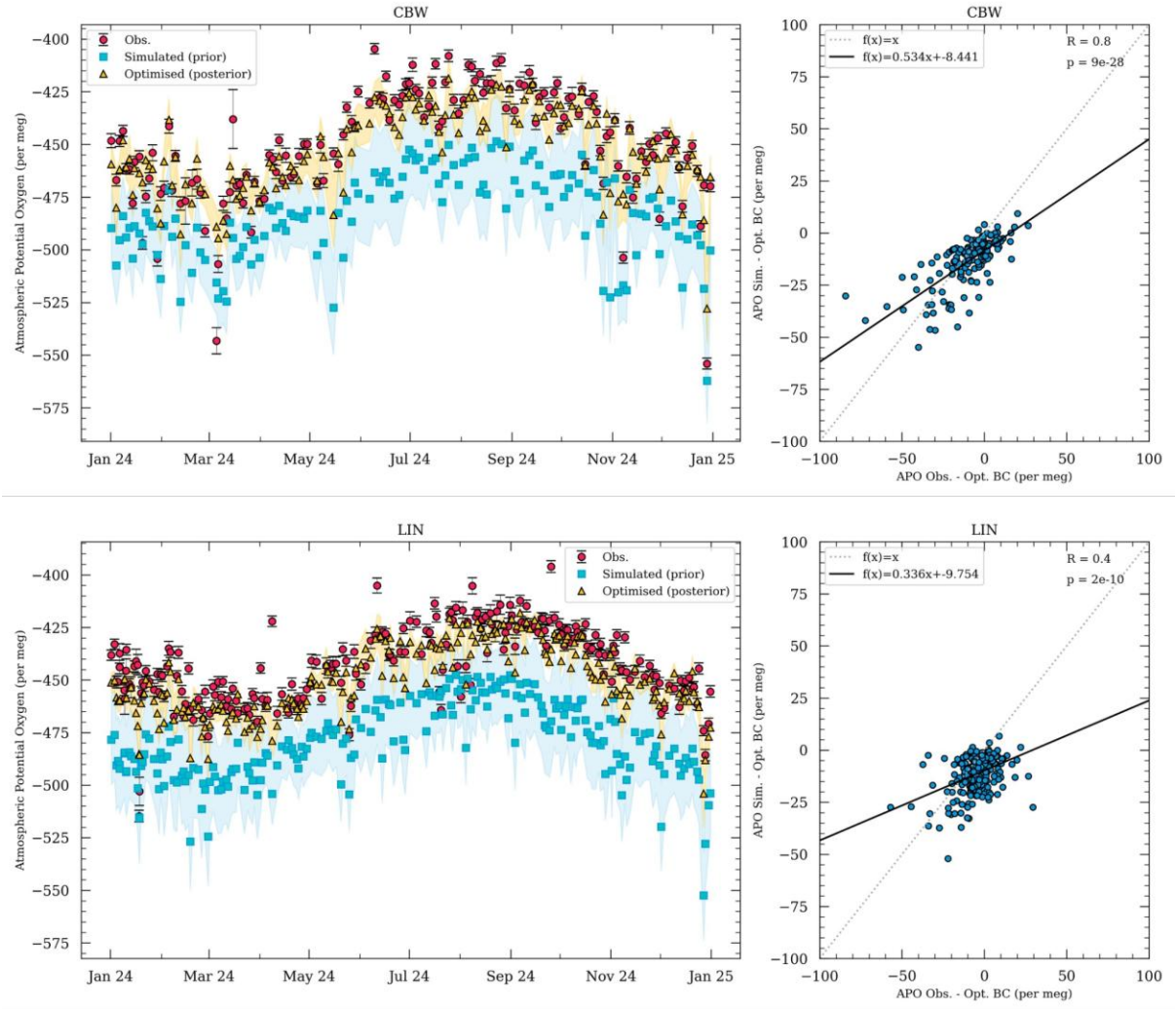

Figure 31: Observed (red), simulated (blue) and RHIME-optimised (yellow) APO values for the year 2024 at CBW (top row) and LIN (bottom row). Error bars and shaded regions denote the 65% confidence interval regions in the prior model simulations. Scatter plots show the detrended (background removed) optimised-observation comparisons.

NAME-RHIME: Model-data comparison

Figure 31 shows the 2024 APO derived from atmospheric CO_2 and O_2 observations at CBW and LIN measurement stations, along with the forward simulations produced using EDGAR-GridFED fossil fuel APO emissions estimates and NEMO-ERSEM ocean APO flux estimates in RHIME.

The bias of ~30 per meg between observations and a priori forward simulations is seen, mainly due to the extrapolated APO boundary conditions used in this simulation. The variation of the APO values in the simulations is similar to the observations for this period, but many of the very negative APO excursions seen in the observations have not been captured in the simulations. These very large negative excursions (around May-August) are likely due to fossil fuel emission events. However, the timing of these events aligns with when the terrestrial biosphere is most active. Furthermore, such events are not observed during the winter months when higher fossil fuel emissions would be expected. This is the general picture for forward simulations across the network.

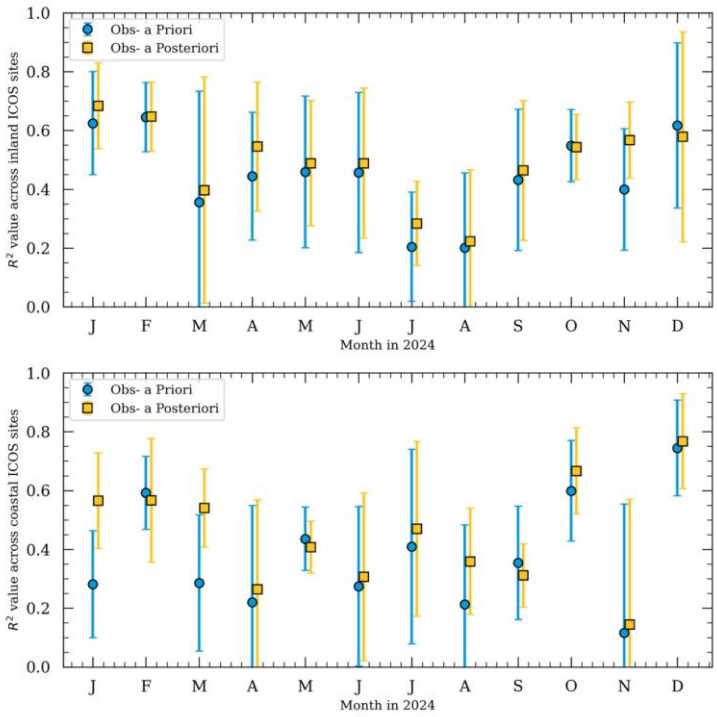

Figure 32: Monthly average Pearson correlation coefficients between the APO observations and a priori simulations (blue) and observations and optimised simulations (yellow) split between sites further inland (HPB, JFJ, KIT, KRE, OXK) shown on the top panel and sites closer to the coast (CBW, GAT, HTM, NOR, STE) shown on the lower panel. Error bars represent the 1σ standard deviation of the correlation coefficients calculated across the subset of sites.

The optimised APO values shown in Fig. 31 have an improved agreement with the observations at CBW and LIN. Looking at the monthly-averaged Pearson's correlation coefficients between the observations and optimised simulations (and a priori simulations) across the network (Fig. 32) we see that the optimised APO values agree better with the observations across all months.

We also see a clear seasonal trend in the Pearson's correlation coefficients, with higher values during the winter and lower values during the summer. We find that sites further inland (HPB, JFJ, KIT, KRE, OXK) have higher Pearson's correlation coefficient values (better correspondence with observations) than sites closer to the coast (CBW, GAT, HTM, NOR, STE). It is likely that oceanic APO is influencing sites closer to the coast and that these differences arise because oceanic APO is poorly captured in the NEMO-ERSEM ocean model.

The lower Pearson's correlation coefficients in the summer could suggest the influence of APO fluxes from the terrestrial biosphere, which should theoretically be masked out. Rodenbeck et al. (2024) found in their APO pseudo-simulations and inversions possible influences of APO from the terrestrial biosphere which could be influencing land-based APO fluxes.

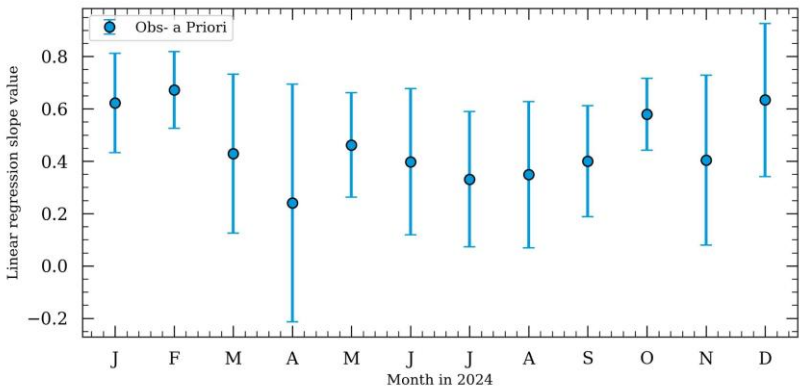

Figure 33: Slope of linear regressions applied to APO observations and a priori simulations at each site in each month of 2024. Markers denote the mean slope value and error bars the 68% variation.

As indicated in Figure 31, a substantial under-estimate in the least-squares regression slope is observed for the APO prior simulations. This slope compares the above or below-baseline variation in APO in the model versus the observations. If this signal is dominated by fossil fuel fluxes, and if model transport was accurate, a slope close to 1 would be expected. Smaller slopes indicate an under-estimate in model $ffCO_2$. Across the network, mean slopes between the model and the observations on the order of 0.5 are seen (Figure 33). If the observed above-baseline observations are dominated by fossil fuel emissions, this would imply that fossil fuel CO_2 emissions would need to be increased by approximately a factor of 2, which would be inconsistent with the difference between prior estimates, and with the results for $\Delta^{14}CO_2$ at the European scale. Some seasonality in the slope is seen, which could indicate changes in $ffCO_2$, or of seasonal changes in ocean influences or biosphere exchange ratios.

NAME-RHIME: Emissions estimates for Germany

Figure 34 shows the APO-inferred RHIME fossil fuel CO_2 emissions estimates for Germany in 2024. Given the very large uncertainty assumed on the model simulations (Figure 31), the inversion was found to primarily adjust boundary conditions, with little adjustment to the prior fluxes. Further work should examine and revise prior model uncertainties to determine the results that would be obtained in a data-driven scenario. As shown in Figure 31, substantial model-data residuals were seen in the posterior solution supporting the hypothesis of under-fitting in the inversion.

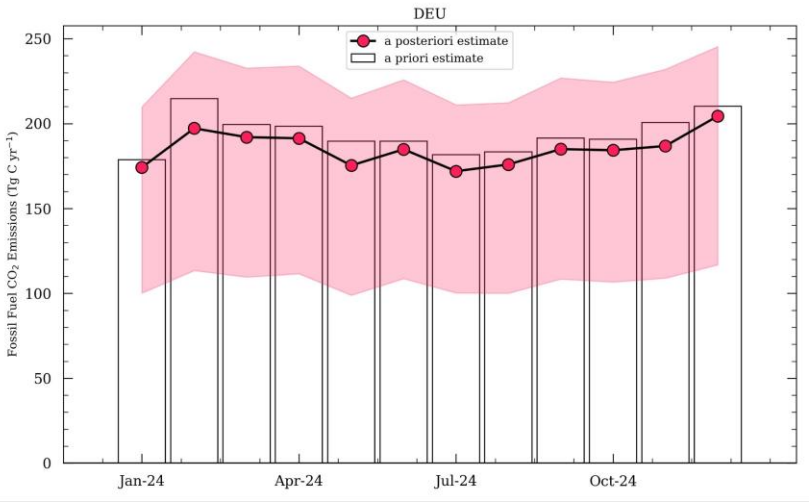

Figure 34: Preliminary APO-inferred RHIME fossil fuel CO_2 emissions estimates for Germany in 2024. The red markers show the a posterior emissions estimate (with the shaded region denoting the 68% confidence interval) and the black bars the a priori emissions estimate from EDGAR. Note that this inversion used a very large uncertainty for the simulated APO (see Figure 31), leading to a highly prior-constrained solution. As shown in Figure 31, substantial residuals remained in the posterior model-measurement comparison. Further work is needed to determine appropriate model uncertainties in this system, and determine fluxes that would be derived in a more data-driven inversion.

4.3 Conclusions

Major model development was conducted in tasks 3.3 and 3.4, with the implementation of multi-tracer and fossil fuel inversion systems in four inverse modelling frameworks, exploiting atmospheric $\Delta^{14}CO_2$ and, for two of them, O_2 and APO. The parallel analyses of these systems are documented above and converge to general conclusions at both regional and global scales.

At regional scale, the systems assimilating $^{14}CO_2$ data tend to adjust the fossil fuel emissions in a limited part of north-western Europe around the core of the $\Delta^{14}CO_2$ sampling network, and in particular in Germany. The robustness of the corresponding fossil fuel emission estimates should be carefully assessed. However, the annual budgets derived for Germany when assimilating $\Delta^{14}CO_2$ observations are broadly consistent. Furthermore, the inversions tend to maintain or increase the seasonal variations compared to the inventories used as prior estimates in a consistent way, leading to similar seasonality across the systems, especially in Germany. The control of the fossil fuel emissions is stronger in 2024 (the posterior estimate being more strongly constrained by the observations, and less impacted by the choice of the prior estimate) than during previous years, exploiting the enhanced $\Delta^{14}CO_2$ sampling during this year.

The results obtained over Europe when assimilating O_2 or APO data appear to be more preliminary than those obtained with atmospheric $\Delta^{14}CO_2$ observations, with major differences between the results obtained with the RHIME and CTE inversions. The individual results show that O_2 provides additional information on fossil fuel emissions, but further work is needed to reconcile the model results. Specific focus of follow up work should be on the added value of continuous O_2 measurements.

At a global and multi-decennial scale, the current global background network of atmospheric $\Delta^{14}CO_2$ and O_2 observations brings useful constraints for the estimate of the natural sinks, but does not lead to a strong and robust control of the fossil fuel CO_2 emissions. The assimilation of O_2 observations in addition to CO_2 observations in the CTE system strengthens the partitioning between land and biosphere fluxes. In the CIF-LMDZ inversions, over the past two decades, the joint $^{14}CO_2$-CO_2 assimilation is focused on the control of the NEE and of the ^{14}C

isotopic signature of the heterotrophic respiration, which are highly uncertain, but does not lead to significant corrections to the fossil fuel emissions outside of Europe. The potential to control the fossil fuel emissions in Europe depends on the spatial resolution of the transport simulations and on the density of the $\Delta^{14}CO_2$ network in the continent. However, it is important to maintain a background $\Delta^{14}CO_2$ and O_2 network and large scale analysis with global systems to constrain the baseline for the regional inversions.

5 Recommendations for the CO2MVS

Based on the above conclusions, and lessons learned during Tasks 3.3 and 3.4 the following recommendations regarding the use of $\Delta^{14}CO_2$ and O_2 data for CO2MVS in the CAMS/IFS system are suggested:

1. The ongoing development of $^{14}CO_2$ and O_2 in the IFS should be continued and further evaluated as a prerequisite to inverse simulations. Forward simulations have been shown to provide useful diagnostics of model fluxes, even without inverse modelling studies being performed.
2. Given the relative consistency of inverse estimates of fossil fuel CO_2 fluxes in parts of north-western Europe, particularly Germany, during 2024, the findings of this report support the added value of atmospheric $\Delta^{14}CO_2$ as a tracer of fossil fuel emissions, compared to atmospheric CO_2 mole fraction observations alone. Therefore, the relatively high-frequency sampling established during CORSO should be continued. Furthermore, to provide $ffCO_2$ constraints on countries outside of Germany, the network should be expanded across Europe.
3. The current global background monitoring system did not provide a strong constraint on global fossil fuel CO_2 emissions. However, global inversions will be important to constrain boundary conditions for future regional modelling studies. Therefore, maintenance of the background network should be encouraged. Enhanced global monitoring may allow for improved understanding of global fossil fluxes in the future.
4. Inversions of $\Delta^{14}CO_2$ are influenced by uncertainties in heterotrophic respiration fluxes and their ^{14}C isotopic signatures, particularly at the global scale. Further work is needed to constrain these fluxes using observations and models.
5. Further work is needed to establish the use of simultaneous atmospheric measurements of CO_2 and O_2 as a tracer for fossil fuel CO_2 emissions. In particular, the role of oceanic fluxes should be investigated, and potential errors or variations in assumed biosphere/atmosphere exchange ratios. Furthermore, the added value of high-frequency O_2 observations has not yet been established beyond forward model comparisons. Further research on this subject is expected through the Horizon Europe PARIS project in 2026.

6 References

Basu, S., Miller, J. B., & Lehman, S. (2016). Separation of biospheric and fossil fuel fluxes of CO_2 by atmospheric inversion of CO_2 and $^{14}CO_2$ measurements: Observation System Simulations. Atmos. Chem. Phys., 16(9), 5665–5683. https://doi.org/10.5194/acp-16-5665-2016

Berchet, A., E. Solemn, R. L. Thompson, I. Pison, J. Thanwerdas, G. Broquet, F. Chevallier, T. Aalto, A. Berchet, P. Bergamaschi, D. Brunner, R. Engelen, A. Fortems-Cheiney, C. Gerbig, C. D. Groot Zwaaftink, J.-M. Haussaire, S. Henne, S. Houwling, U. Karstens, W. L. Kutsch, I. T. Luijkx, G. Monteil, P. I. Palmer, J. C. A. van Peet, W. Peters, P. Peylin, E. Potier, C. Rodenbeck, M. Saunois, M. Scholze, A. Tsuruta, and Y. Zhao (2020). "The Community Inversion Framework v1.0: a unified system for atmospheric inversion studies". Geosci. Model Dev, 14, pg 5331-5354, doi:10.5194/gmd-14-5331-2021.

Bergamaschi, P., Colomb, A., De Mazière, M., Emmenegger, L., Kubistin, D., Lehner, I., Lehtinen, K., Lund Myhre, C., Marek, M., Platt, S.M., Plaß-Dülmer, C., Schmidt, M., Apadula, F., Arnold, S., Blanc, P.-E., Brunner, D., Chen, H., Chmura, L., Conil, S., Couret, C., Cristofanelli, P., Delmotte, M., Forster, G., Frumau, A., Gheusi, F., Hammer, S., Haszpra, L., Heliasz, M., Henne, S., Hoheisel, A., Kneuer, T., Laurila, T., Leskinen, A., Leuenberger, M., Levin, I., Lindauer, M., Lopez, M., Lunder, C., Mammarella, I., Manca, G., Manning, A., Marklund, P., Martin, D., Meinhardt, F., Müller-Williams, J., Necki, J., O'Doherty, S., Ottosson-Löfvenius, M., Philippon, C., Piacentino, S., Pitt, J., Ramonet, M., Rivas-Soriano, P., Scheeren, B., Schumacher, M., Sha, M.K., Spain, G., Steinbacher, M., Sørensen, L.L., Vermeulen, A., Vítková, G., Xueref-Remy, I., di Sarra, A., Conen, F., Kazan, V., Roulet, Y.-A., Biermann, T., Heltai, D., Hensen, A., Hermansen, O., Komínková, K., Laurent, O., Levula, J., Pichon, J.-M., Smith, P., Stanley, K., Trisolino, P., ICOS Carbon Portal, ICOS Atmosphere Thematic Centre, ICOS Flask And Calibration Laboratory, ICOS Central Radiocarbon Laboratory, 2023. European Obspack compilation of atmospheric carbon dioxide data from ICOS and non-ICOS European stations for the period 1972-2022; obspack_co2_466_GLOBALVIEWplus_v8.0_2023-03-30. https://doi.org/10.18160/CEC4-CAGK

Butenschön, M., Clark, J., Aldridge, J. N., Icarus Allen, J., Artioli, Y., Blackford, J., Bruggeman, J., Cazenave, P., Ciavatta, S., Kay, S., Lessin, G., van Leeuwen, S., van der Molen, J., de Mora, L., Polimene, L., Sailley, S., Stephens, N., & Torres, R. (2016). ERSEM 15.06: A generic model for marine biogeochemistry and the ecosystem dynamics of the lower trophic levels. *Geoscientific Model Development*, *9*(4). https://doi.org/10.5194/gmd-9-1293-2016

Chawner, H., Saboya, E., Adcock, K. E., Arnold, T., Artioli, Y., Dylag, C., Forster, G. L., Ganesan, A., Graven, H., Lessin, G., Levy, P., Luijkx, I. T., Manning, A., Pickers, P. A., Rennick, C., Rödenbeck, C., & Rigby, M. (2024). Atmospheric oxygen as a tracer for fossil fuel carbon dioxide: a sensitivity study in the UK. *Atmospheric Chemistry and Physics*, *24*(7), 4231–4252. https://doi.org/10.5194/acp-24-4231-2024

Chau, T. T. T., M. Gehlen, and F. Chevallier (2022). "A seamless ensemble-based reconstruction of surface ocean pCO2 and air-sea CO2, fluxes over the global coastal and open oceans". Biogeosciences, 19(4), pg 1087-1109, doi:10.5194/bg-19-1087-2022.

Chau, T.-T.-T., F. Chevallier, and M. Gehlen (2024a). "Global analysis of surface ocean CO2 fugacity and air-sea fluxes with low latency". Geophysical Research Letters, 51, e2023GL106670. doi:10.1029/2023GL106670

Chau, T.-T.-T., M. Gehlen, N. Metzl, and F. Chevallier, F. (2024b). “CMEMS-LSCE: a global, 0.25°, monthly reconstruction of the surface ocean carbonate system”. Earth Syst. Sci. Data, 16, 121–160, doi:10.5194/essd-16-121-2024.

Chevallier, F., M. Fischer, P. Peylin, S. Serrar, P. Bousquet, F.-M. Breton, A. Chedin, P. Ciais (2005). “Inferring CO2 sources and sinks from satellites observations: Method and applications to TOVS data”. J. Geopys. Res. Atmos., 110(D24), doi:10.1029/2005JD006390.

Chevallier, F., Z. Lloret, A. Cozic (2023). “Evaluation and Quality control document for the satellite-driven CO2 inversion FT22r1”. Copernicus Atmosphere Monitoring Service, Report, REF: CAMS255_2021SC1_D1.4.1-2023-1_202302_v1v1_Validation FT inversion

Copernicus Atmosphere Monitoring Service (2020). CAMS global inversion-optimised greenhouse gas fluxes and concentrations. Copernicus Atmosphere Monitoring Service (CAMS) Atmosphere Data Store, DOI: 10.24381/ed2851d.

Crippa, M., Guizzardi, D., Solazzo, E., Muntean, M., Schaaf, E., Monforti-Ferrario, F., Banja, M., Olivier, J. G. J., Grassi, G., Rossi, S., & Vignati, E. (2021). GHG emissions of all world countries - 2021 Report. In *Publications Office of the European Union* (Issue October).

Friedlingstein, P. M. O'Sullivan, M. W. Jones, R. M. Andrew, D. C. E. Bakker, J. Hauck, P. Landschützer, C. Le Quéré, I. T. Luijkx, G. P. Peters, W. Peters, J. Pongratz, C. Schwingshackl, S. Sitch, J. G. Canadell, P. Ciais, R. B. Jackson, S. R. Alin, P. Anthoni, L. Barbero, N. R. Bates, M. Becker, N. Bellouin, B. Decharme, L. Bopp, I. B. M. Brasika, P. Cadule, M. A. Chamberlain, N. Chandra, T.-T.-T. Chau, F. Chevallier, L. P. Chini, M. Cronin, X. Dou, K. Enyo, W. Evans, S. Falk, R. A. Feely, L. Feng, D. J. Ford, T. Gasser, J. Ghattas, T. Gkritzalis, G. Grassi, L. Gregor, N. Gruber, Ö. Gürses, I. Harris, M. Hefner, J. Heinke, R. A. Houghton, G. C. Hurtt, Y. Iida, T. Ilyina, A. R. Jacobson, A. Jain, T. Jarníková, A. Jersild, F. Jiang, Z. Jin, F. Joos, E. Kato, R. F. Keeling, D. Kennedy, K. K. Goldewijk, J. Knauer, J. I. Korsbakken, A. Körtzinger, X. Lan, N. Lefèvre, H. Li, J. Liu, Z. Liu, L. Ma, G. Marland, N. Mayot, P. C. McGuire, G. A. McKinley, G. Meyer, E. J. Morgan, D. R. Munro, S.-I. Nakaoka, Y. Niwa, K. M. O'Brien, A. Olsen, A. M. Omar, T. Ono, M. Paulsen, D. Pierrot, K. Pocock, B. Poulter, C. M. Powis, G. Rehder, L. Resplandy, E. Robertson, C. Rödenbeck, T. M. Rosan, J. Schwinger, R. Séférian, T. L. Smallman, S. M. Smith, R. Sospedra-Alfonso, Q. Sun, A. J. Sutton, C. Sweeney, S. Takao, P. P. Tans, H. Tian, B. Tilbrook, H. Tsujino, F. Tubiello, G. R. van der Werf, E. van Ooijen, R. Wanninkhof, M. Watanabe, C. Wimart-Rousseau, D. Yang, X. Yang, W. Yuan, X. Yue, S. Zaehle, J. Zeng, and B. Zheng (2023). “Global Carbon Budget 2023”. Earth System Science Data, 15(2), pg 5301-5369, doi:10.5194/essd-15-5301-2023.

Ganesan, A. L., Rigby, M., Zammit-Mangion, A., Manning, A. J., Prinn, R. G., Fraser, P. J., Harth, C. M., Kim, K. R., Krummel, P. B., Li, S., Mühle, J., O’Doherty, S. J., Park, S., Salameh, P. K., Steele, L. P., & Weiss, R. F. (2014). Characterization of uncertainties in atmospheric trace gas inversions using hierarchical Bayesian methods. *Atmospheric Chemistry and Physics*, *14*(8). https://doi.org/10.5194/acp-14-3855-2014

Gómez-Ortiz, C., Monteil, G., Basu, S., and Scholze, M. (2025a). A CO_2–$\mathbf{\Delta}^{14}CO_2$ inversion setup for estimating European fossil CO_2 emissions, Atmospheric Chemistry and Physics, 25, 397–424, https://doi.org/10.5194/ACP-25-397-2025
Gómez-Ortiz, C., Monteil, G., Karstens, U., and Scholze, M. (2025b). Preparing for an extensive $^{14}CO_2$ flask sample monitoring campaign over Europe to constrain fossil CO_2 emissions, EGUsphere, 2025, 1–35, https://doi.org/10.5194/egusphere-2024-3013
Graven, H., Keeling, R. F., & Rogelj, J. (2020). Changes to Carbon Isotopes in Atmospheric CO_2 Over the Industrial Era and Into the Future. Global Biogeochemical Cycles, 34(11), e2019GB006170. https://doi.org/https://doi.org/10.1029/2019GB006170

Graven, H. D. and Gruber, N. (2011). “Continental-scale enrichment of atmospheric 14CO2 from the nuclear power industry: potential impact on the estimation of fossil fuel-derived CO2”. Atmospheric Chemistry and Physics, 11(23), 12339–12349, doi:10.5194/acp-11-12339-2011.

Hersbach H, Bell B, Berrisford P, et al.: The ERA5 global reanalysis, Q J R Meteorol Soc., 146, 1999–2049, https://doi.org/10.1002/qj.3803, 2020.

Holtslag, A. A. M., and B. A. Boville: Local Versus Nonlocal Boundary-Layer Diffusion in a Global Climate Model, J. Climate, 6, 1825–1842, https://doi.org/10.1175/1520-0442(1993)006<1825:LVNBLD>2.0.CO;2, 1993.

Hooghiem et al.: A multi-tracer data assimilation system combining a long- and short-window approach: CarbonTracker Europe-LW-SW v1.0, in prep. 2025.

Hoffman, M. D., & Gelman, A. (2014). The no-U-turn sampler: Adaptively setting path lengths in Hamiltonian Monte Carlo. *Journal of Machine Learning Research*, *15*.

ICOS RI, Apadula, F., Arnold, S., Bergamaschi, P., Biermann, T., Chen, H., Colomb, A., Conil, S., Couret, C., Cristofanelli, P., De Mazière, M., Delmotte, M., Di Iorio, T., Emmenegger, L., Forster, G., Frumau, A., Harris, E., Haszpra, L., Hatakka, J., Heliasz, M., Heltai, D., Hensen, A., Hermansen, O., Hoheisel, A., Kneuer, T., Komínková, K., Kubistin, D., Larmanou, E., Laurent, O., Laurila, T., Lehner, I., Lehtinen, K., Leskinen, A., Leuenberger, M., Levula, J., Lindauer, M., Lopez, M., Lund Myhre, C., Lunder, C., Mammarella, I., Manca, G., Manning, A., Marek, M.V., Marklund, P., Meinhardt, F., Miettinen, P., Molnár, M., Montaguti, S., Mölder, M., Müller-Williams, J., O'Doherty, S., Ottosson-Löfvenius, M., Piacentino, S., Pichon, J.-M., Pitt, J., Platt, S.M., Plaß-Dülmer, C., Ramonet, M., Rivas-Soriano, P., Roulet, Y.-A., Scheeren, B., Schmidt, M., Schumacher, M., Sferlazzo, D., Sha, M.K., Smith, P., Stanley, K., Steinbacher, M., Sørensen, L.L., Trisolino, P., Vítková, G., Ylisirniö, A., Yver-Kwok, C., Zazzeri, G., Zwerschke, E., di Sarra, A., ICOS ATC-Laboratoires des Sciences du Climat et de L'Environnement (LSCE), France, ICOS Central Radiocarbon Laboratory (CRL), Germany, ICOS Flask And Calibration Laboratory (FCL), Germany (2025). ICOS Atmosphere Release 2025-1 of Level 2 Greenhouse Gas Mole Fractions of CO_2, CH_4, N_2O, CO, meteorology and $^{14}CO_2$, and flask samples analysed for CO_2, CH_4, N_2O, CO, H_2, SF_6, $\delta^{13}C\text{-}CO_2$, $\delta^{18}O\text{-}CO_2$, $\delta O_2/N_2$ and $^{14}CO_2$. https://doi.org/10.18160/PP29-9CNZ

Janssens-Maenhour, G., M. Crippa, D. Guizzardi, M. Muntean, E. Schaaf, F. Dentener, P. Bergamaschi, V. Pagliari, J. G. J. Olivier, J. A. H. W. Peters, J. A. van Aardenne, S. Monni, U. Doering, A. M. R. Petrescu, E. Solazzo, and G. D. Oreggioni (2019). “EDGAR v4.3.2 Global Atlas of the three major greenhouse gas emissions for the period 1970-2012”. Earth System Science Data, 11, pg 959-1002, doi:10.5194/essd-11-959-2019.

Jones, A., Thomson, D., Hort, M., & Devenish, B. (2007). The U.K. Met Office’s Next-Generation Atmospheric Dispersion Model, NAME III. In *Air Pollution Modeling and Its Application XVII* (pp. 580–589). Springer US. https://doi.org/10.1007/978-0-387-68854-1_62

Jones, M. W., Andrew, R. M., Peters, G. P., Janssens-Maenhout, G., De-Gol, A. J., Ciais, P., Patra, P. K., Chevallier, F., & Le Quéré, C. (2021). Gridded fossil CO2 emissions and related O2 combustion consistent with national inventories 1959–2018. *Scientific Data*, *8*(1). https://doi.org/10.1038/s41597-020-00779-6

Kanu, A. M., L. L. Comfort, T. P. Guilderson, P. J. Cameron-Smith, D. J. Bergmann, E. L. Atlas, S. Schauffler, and K. A. Boering (2016). “Measurements and modeling of contemporary radiocarbon in the stratosphere”. Geophysical Research Letters, 43(3), pg 1399-1406, doi:10.1002/2015GL066921.

Keeling, R. F., & Manning, A. C. (2014). Studies of Recent Changes in Atmospheric O2 Content. In *Treatise on Geochemistry: Second Edition* (Vol. 5). https://doi.org/10.1016/B978-0-08-095975-7.00420-4

Krinner, G., N. Viovy, N. de Noblet-Ducoudré, J. Ogée, J. Polcher, P. Friedlingstein, P. Ciais, S. Sitch, and I. C. Prentice (2005). "A dynamic global vegetation model for studies of the coupled atmosphere-biosphere system". Global Biogeochemistry Cycles, 19(1), doi:10.1029/2003GB002199.

Koch, F.-T., Gerbig, C. (2025). European anthropogenic CO_2 emissions based on EDGARv4.3 and the Statistical Review of World Energy 2025 for 2005-2024. https://doi.org/10.18160/3GP1-JZKA

Krol, M., Houweling, S., Bregman, B., van den Broek, M., Segers, A., van Velthoven, P., Peters, W., Dentener, F., and Bergamaschi, P.: The two-way nested global chemistry-transport zoom model TM5: algorithm and applications, Atmos. Chem. Phys., 5, 417–432, https://doi.org/10.5194/acp-5-417-2005, 2005.

Lehman, S. J., Miller, J. B., Wolak, C., Southon, J., Tans, P. P., Montzka, S. A., Sweeney, C., Andrews, A., LaFranchi, B., Guilderson, T. P., & Turnbull, J. C. (2013). Allocation of Terrestrial Carbon Sources Using $^{14}CO_2$: Methods, Measurement, and Modeling. Radiocarbon, 55(3), 1484–1495. https://doi.org/DOI: 10.1017/S0033822200048414

Levin, I., Kromer, B., Schmidt, M., & Sartorius, H. (2003). A novel approach for independent budgeting of fossil fuel CO_2 over Europe by $^{14}CO_2$ observations. Geophysical Research Letters, 30(23), 2194. https://doi.org/10.1029/2003GL018477

Lemarié, F., Samson, G., Redelsperger, J. L., Giordani, H., Brivoal, T., & Madec, G. (2021). A simplified atmospheric boundary layer model for an improved representation of air-sea interactions in eddying oceanic models: Implementation and first evaluation in NEMO (4.0). *Geoscientific Model Development*, *14*(1). https://doi.org/10.5194/gmd-14-543-2021

Lindsay, C. M. (2016). "Carbon dynamics of the deglacial and contemporary ocean inferred from radiocarbon measurements in foraminifera, seawater and atmospheric carbon dioxide". Ph.D. thesis. Geological Sciences, University of Colorado Boulder.

Louis, JF.: A parametric model of vertical eddy fluxes in the atmosphere, Boundary-Layer Meteorol 17, 187–202, https://doi.org/10.1007/BF00117978, 1979.

Machta, L., & Hughes, E. (1970). Atmospheric oxygen in 1967 to 1970. *Science*, *168*(3939). https://doi.org/10.1126/science.168.3939.1582

Maier, F., Levin, I., Gachkivskyi, M., Rödenbeck, C., & Hammer, S. (2023). Estimating regional fossil fuel CO_2 concentrations from $^{14}CO_2$ observations: challenges and uncertainties. Philosophical Transactions of the Royal Society A, 381(2261). https://doi.org/10.1098/RSTA.2022.0203

Masarik, J. and J. Beer (2009). "An updated simulation of particle fluxes and cosmogenic nuclide production in the Earth's atmosphere". J. Geophys. Res., 114(D11103), doi:10.1029/2008JD010557

Miller, J. B., Lehman, S. J., Montzka, S. A., Sweeney, C., Miller, B. R., Karion, A., Wolak, C., Dlugokencky, E. J., Southon, J., Turnbull, J. C., & Tans, P. P. (2012). Linking emissions of fossil fuel CO_2 and other anthropogenic trace gases using atmospheric $^{14}CO_2$. Journal of Geophysical Research: Atmospheres, 117(D8). https://doi.org/https://doi.org/10.1029/2011JD017048

Monteil, G., & Scholze, M. (2021). Regional CO_2 inversions with LUMIA, the Lund University Modular Inversion Algorithm, v1.0. Geosci. Model Dev., 14(6), 3383–3406. https://doi.org/10.5194/gmd-14-3383-2021

Naegler, T., & Levin, I. (2009). Biosphere-atmosphere gross carbon exchange flux and the $\delta^{13}CO_2$ and $\Delta^{14}CO_2$ disequilibria constrained by the biospheric excess radiocarbon inventory. Journal of Geophysical Research: Atmospheres, 114(D17). https://doi.org/10.1029/2008JD011116

Nakada, A., Miyauchi, T., Akiyama, K., Momose, T., Kozawa, T., Yokota, T. and Ohtomo, H. (2008). “Radioactive airborne effluent discharged from Tokai reprocessing plant. 1998-2007”, Japan Atomic Energy Agency, Tokai, Ibaraki (Japan). [online] Available from: https://inis.iaea.org/search/search.aspx?orig_q=RN:40102398 (Accessed 3 December 2024).

Oda, T., & Maksyutov, S. (2023). ODIAC Fossil Fuel CO_2 Emissions Dataset (Version name: ODIAC2023a). https://doi.org/10.17595/20170411.001
Peters, W., et al.: An Atmospheric Perspective on North American Carbon Dioxide Exchange: CarbonTracker, Proceedings of the National Academy of Sciences 104 (48), 18925–30, https://doi.org/10.1073/pnas.0708986104, 2007.

Pickers, P. A., Manning, A. C., Quéré, C. le, Forster, G. L., Luijkx, I. T., Gerbig, C., Fleming, L. S., & Sturges, W. T. (2022). Novel quantification of regional fossil fuel CO2 reductions during COVID-19 lockdowns using atmospheric oxygen measurements. *Science Advances*, *8*(16). https://doi.org/10.1126/sciadv.abl9250

Potier, E., G. Broquet, Y. Wang, D. Santaren, A. Berchet, I. Pison, J. Marshall, P. Ciais, F.-M. Bréon, and F. Chevallier (2022). “Complementing XCO2 imagery with ground-based CO2 and 14CO2 measurements to monitor CO2 emissions from fossil fuels on a regional to local scale”. Atmospheric Measurement Techniques, 15(18), pg 5261–5288, doi:10.5194/amt-15-5261-2022.

Randerson, J. T., Enting, I. G., Schuur, E. A. G., Caldeira, K. and Fung, I. Y.: Seasonal and latitudinal variability of troposphere Δ14CO2: Post bomb contributions from fossil fuels, oceans, the stratosphere, and the terrestrial biosphere, Global Biogeochem. Cycles, 16(4), 59-1-59–19, doi:10.1029/2002gb001876, 2002.

Rödenbeck, C., Adcock, K. E., Eritt, M., Gachkivskyi, M., Gerbig, C., Hammer, S., Jordan, A., Keeling, R. F., Levin, I., Maier, F., Manning, A. C., Moossen, H., Munassar, S., Pickers, P. A., Rothe, M., Tohjima, Y., & Zaehle, S. (2023). The suitability of atmospheric oxygen measurements to constrain western European fossil-fuel CO2 emissions and their trends. *Atmospheric Chemistry and Physics*, *23*(24). https://doi.org/10.5194/acp-23-15767-2023

Russell, G. L., & Lerner, J. A.: A New Finite-Differencing Scheme for the Tracer Transport Equation, Journal of Applied Meteorology (1962-1982), 20(12), 1483–1498, http://www.jstor.org/stable/26180374, 1981.

Saboya, E., Manning, A. J., Levy, P., Stanley, K. M., Pitt, J., Young, D., Say, D., Grant, A., Arnold, T., Rennick, C., Tomlinson, S. J., Carnell, E. J., Artioli, Y., Stavart, A., Spain, T. G., O’Doherty, S., Rigby, M., & Ganesan, A. L. (2024). Combining Top-Down and Bottom-Up Approaches to Evaluate Recent Trends and Seasonal Patterns in UK N_2O Emissions. *Journal of Geophysical Research: Atmospheres*, *129*(14). https://doi.org/10.1029/2024JD040785

Say, D., Manning, A. J., Western, L. M., Young, D., Wisher, A., Rigby, M., Reimann, S., Vollmer, M. K., Maione, M., Arduini, J., Krummel, P. B., Mühle, J., Harth, C. M., Evans, B.,

Weiss, R. F., Prinn, R. G., & O'Doherty, S. (2021). Global trends and European emissions of tetrafluoromethane (CF4), hexafluoroethane (C2F6) and octafluoropropane (C3F8). *Atmospheric Chemistry and Physics*, *21*(3). https://doi.org/10.5194/acp-21-2149-2021

Scholze, M., Kaplan, J. O., Knorr, W., and Heimann, M. (2003), "Climate and interannual variability of the atmosphere-biosphere 13CO2 flux", Geophys. Res. Lett., 30, 1097, doi:10.1029/2002GL015631.

Sitch, S., Smith, B., Prentice, I.C., Arneth, A., Bondeau, A., Cramer, W., Kaplan, J.O., Levis, S., Lucht, W., Sykes, M.T., Thonicke, K. and Venevsky, S. (2003), "Evaluation of ecosystem dynamics, plant geography and terrestrial carbon cycling in the LPJ dynamic global vegetation model". Global Change Biology, 9: 161-185. doi:10.1046/j.1365-2486.2003.00569.x

Stephens, B. B., Keeling, R. F., Heimann, M., Six, K. D., Murnane, R., & Caldeira, K. (1998). Testing global ocean carbon cycle models using measurements of atmospheric O2 and CO2 concentration. *Global Biogeochemical Cycles*, *12*(2). https://doi.org/10.1029/97GB03500

Storm, I., Maier, F., Levin, I., Preunkert, S., Karstens, U. ICOS RI, 2024. Annual emission totals of 14CO2 from nuclear facilities, https://hdl.handle.net/11676/v5l2UcS8RBVFORjUzKnZCX31

Stuiver, M., & Polach, H. A. (1977). Discussion Reporting of ^{14}C Data. Radiocarbon, 19(3), 355–363. https://doi.org/DOI: 10.1017/S0033822200003672

Tans, P. P., Berry, J. A., & Keeling, R. F. (1993). Oceanic $^{13}C/^{12}C$ observations: A new window on ocean CO_2 uptake. Global Biogeochemical Cycles, 7(2), 353–368. https://doi.org/10.1029/93GB00053

Tans, P. P., J. A. Berry, R. F. and Keeling (1993). "Oceanic 13C/12C observations: a new window on ocean CO2 uptake". Global Biogeochemical Cycles, 7(2), pg 353–368.

Thanwerdas, J., M. Saunois, A. Berchet, I. Pison, B. H. Vaughn, S. E. Michel, and P. Bousquet (2022). "Variational inverse modeling within the Community Inversion Framework v1.1 to assimilate δ13C(CH4) and CH4: a case study with model LMDz-SACS", Geosci. Model Dev., 15, pg 4831–4851, doi:10.5194/gmd-15-4831-2022.

Tiedtke, M., (1989). "A Comprehensive Mass Flux Scheme for Cumulus Parameterization in Large-Scale Models", Mon. Wea. Rev., 117(8), 1779–1800, doi:10.1175/1520-0493(1989)117<1779:ACMFSF>2.0.CO;2.

Turnbull, J., Rayner, P., Miller, J., Naegler, T., Ciais, P., & Cozic, A. (2009). On the use of $^{14}CO_2$ as a tracer for fossil fuel CO_2: Quantifying uncertainties using an atmospheric transport model. Journal of Geophysical Research: Atmospheres, 114(D22). https://doi.org/10.1029/2009JD012308

van der Laan-Luijkx, Ingrid T., et al.:The CarbonTracker Data Assimilation Shell (CTDAS) v1.0: Implementation and Global Carbon Balance 2001-2015, Geoscientific Model Development, 10, 2785–2800, https://doi.org/10.5194/gmd-10-2785-2017, 2017.
van der Woude, A. (2022). Near real time fluxes. https://doi.org/10.18160/20Z1-AYJ2
Vogelezang, D.H.P., Holtslag, A.A.M.: Evaluation and model impacts of alternative boundary-layer height formulations, Boundary-Layer Meteorol 81, 245–269, https://doi.org/10.1007/BF02430331, 1996.

Van der Werf, G. R., J. T. Randerson, L. Giglio, T. T. van Leeuwen, Y. Chen, B. M. Rogers, M. Mu, M. J. E. van Marle, D. C. Morton, G. J. Collatz, R. J. Yokelson, and P. S. Kasibhatia

(2017). “Global fire emissions estimates during 1997-2016”. Earth System Science Data, 9(2), pg 697-720, doi:10.5194/essd-9-697-2017.

Wang, Y.(2016). “The potential of observations of radiocarbon in atmospheric CO_2 for the atmospheric inversion of fossil fuel CO_2 emission at regional scale”. Ph.D. Thesis. Earth Sciences, Université Paris Saclay (CO-mUE).

Western, L. M., Redington, A. L., Manning, A. J., Trudinger, C. M., Hu, L., Henne, S., Fang, X., Kuijpers, L. J. M., Theodoridi, C., Godwin, D. S., Arduini, J., Dunse, B., Engel, A., Fraser, P. J., Harth, C. M., Krummel, P. B., Maione, M., Mühle, J., O’Doherty, S., … Rigby, M. (2022). A renewed rise in global HCFC-141b emissions between 2017-2021. *Atmospheric Chemistry and Physics*, *22*(14), 9601–9616. https://doi.org/10.5194/acp-22-9601-2022

White, E. D., Rigby, M., Lunt, M. F., Luke Smallman, T., Comyn-Platt, E., Manning, A. J., Ganesan, A. L., O’Doherty, S., Stavert, A. R., Stanley, K., Williams, M., Levy, P., Ramonet, M., Forster, G. L., Manning, A. C., & Palmer, P. I. (2019). Quantifying the UK’s carbon dioxide flux: An atmospheric inverse modelling approach using a regional measurement network. *Atmospheric Chemistry and Physics*, *19*(7). https://doi.org/10.5194/acp-19-4345-2019

Zazzeri, G., E. Acuna Yeomans, and H. D. Graven (2018). “Global and regional emissions of radiocarbon from nuclear power plants from 1972 to 2016”. Radiocarbon, 60(4), pg 1067-1081, doi:10.1017/RDC.2018.42

Document History

Version	Author(s)	Date	Changes
1.0	H. Allen, J. Hooghiem, C. Gómez-Ortiz, E. Saboya, M. Rigby, I. Luijkx, G. Broquet, M. Scholze, A. Visser	5 December, 2025	
1.1	H. Allen, J. Hooghiem, C. Gómez-Ortiz, E. Saboya, M. Rigby, I. Luijkx, G. Broquet, M. Scholze, A. Visser	17 December, 2025	Implemented reviewers feedback

Internal Review History

Internal Reviewers	Date	Comments
Jaroslaw Necki (AGH)	10 December, 2025	Slight changes proposed - some comments added regarding the coherence and figures
Marc Guevara Vilardell (BSC)	15 December, 2025	High level review only